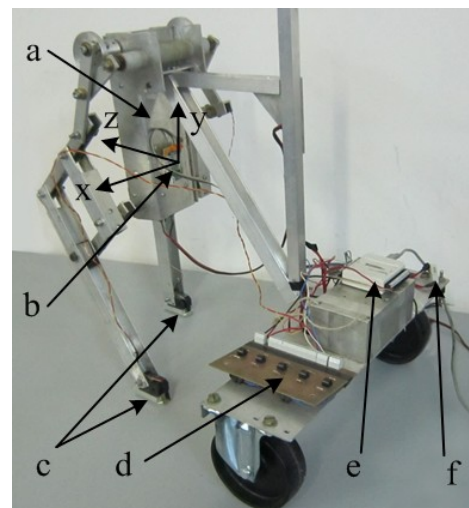
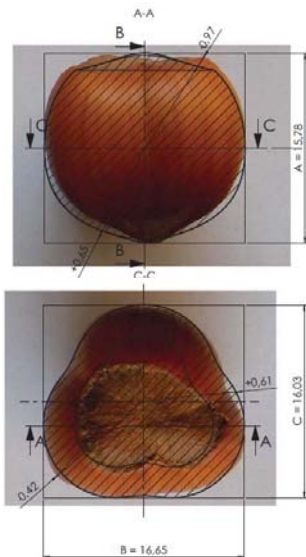
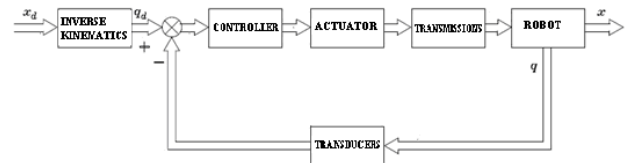
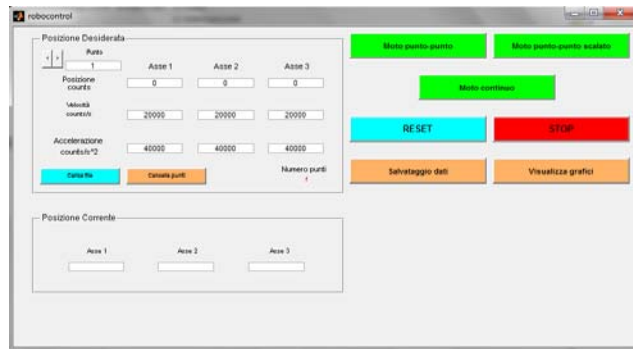
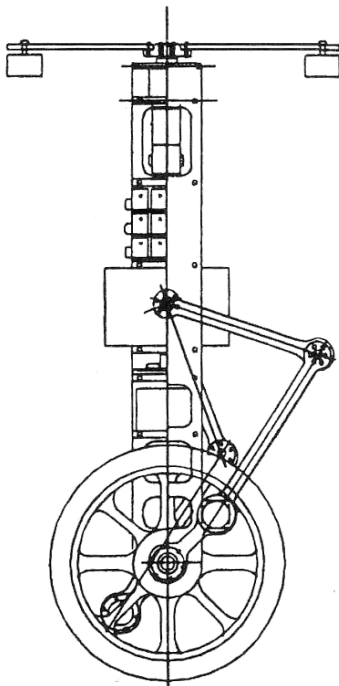


International Journal of Mechanics and Control

Editor: Andrea Manuello Bertetto



Editorial Board of the
International Journal of Mechanics and Control

Published by Levrotto&Bella – Torino – Italy E.C.

Honorary editors

Guido Belforte

Kazy Yamafuji

Editor: Andrea Manuello Bertetto

General Secretariat: Elvio Bonisoli

Atlas Akhmetzyanov
*V.A.Trapeznikov Institute of Control Sciences
of Russian Academy of Sciences
Moscow – Russia*

Domenico Appendino
*Prima Industrie
Torino – Italy*

Kenji Araki
*Saitama University
Shimo Okubo, Urawa
Saitama – Japan*

Guido Belforte
*Technical University – Politecnico di Torino
Torino – Italy*

Bruno A. Boley
*Columbia University,
New York – USA*

Marco Ceccarelli
*LARM at DIMSAT
University of Cassino
Cassino – Italy*

Amalia Ercoli Finzi
*Technical University – Politecnico di Milano
Milano – Italy*

Carlo Ferraresi
*Technical University – Politecnico di Torino
Torino – Italy*

Anindya Ghoshal
*Arizona State University
Tempe – Arizona – USA*

Nunziatino Gualtieri
*Space System Group
Alenia Spazio
Torino – Italy*

Alexandre Ivanov
*Technical University – Politecnico di Torino
Torino – Italy*

Giovanni Jacazio
*Technical University – Politecnico di Torino
Torino – Italy*

Takashi Kawamura
*Shinshu University
Nagano – Japan*

Kin Huat Low
*School of Mechanical and Aerospace Engineering
Nanyang Technological University
Singapore*

Andrea Manuello Bertetto
*University of Cagliari
Cagliari – Italy*

Stamos Papastergiou
*Jet Joint Undertaking
Abingdon – United Kingdom*

Mihailo Ristic
*Imperial College
London – United Kingdom*

János Somló
*Technical University of Budapest
Budapest – Hungary*

Jozef Suchy
*Faculty of Natural Science
Banska Bystrica – Slovakia*

Federico Thomas
*Instituto de Robótica e Informática Industrial
(CSIC-UPC)
Barcelona – Espana*

Lubomir Uher
*Institute of Control Theory and Robotics
Bratislava – Slovakia*

Furio Vatta
*Technical University – Politecnico di Torino
Torino – Italy*

Vladimir Viktorov
*Technical University – Politecnico di Torino
Torino – Italy*

Kazy Yamafuji
*University of Electro-Communications
Tokyo – Japan*

*Official Torino Italy Court Registration
n.5390, 5th May 2000*

*Deposito presso il Tribunale di Torino
numero 5390 del 5 maggio 2000*

Direttore responsabile:

Andrea Manuello Bertetto

International Journal of Mechanics and Control

Editor: Andrea Manuello Bertetto

***Honorary editors: Guido Belforte
Kazy Yamafuji***

General Secretariat: Elvio Bonisoli

The Journal is addressed to scientists and engineers who work in the fields of mechanics (mechanics, machines, systems, control, structures). It is edited in Turin (Northern Italy) by Levrotto&Bella Co., with an international board of editors. It will have not advertising.

Turin has a great and long tradition in mechanics and automation of mechanical systems. The journal would will to satisfy the needs of young research workers of having their work published on a qualified paper in a short time, and of the public need to read the results of researches as fast as possible.

Interested parties will be University Departments, Private or Public Research Centres, Innovative Industries.

Aims and scope

The *International Journal of Mechanics and Control* publishes as rapidly as possible manuscripts of high standards. It aims at providing a fast means of exchange of ideas among workers in Mechanics, at offering an effective method of bringing new results quickly to the public and at establishing an informal vehicle for the discussion of ideas that may still in the formative stages.

Language: English

International Journal of Mechanics and Control will publish both scientific and applied contributions. The scope of the journal includes theoretical and computational methods, their applications and experimental procedures used to validate the theoretical foundations. The research reported in the journal will address the issues of new formulations, solution, algorithms, computational efficiency, analytical and computational kinematics synthesis, system dynamics, structures, flexibility effects, control, optimisation, real-time simulation, reliability and durability. Fields such as vehicle dynamics, aerospace technology, robotics and mechatronics, machine dynamics, crashworthiness, biomechanics, computer graphics, or system identification are also covered by the journal.

Please address contributions to

Prof. Guido Belforte
Prof. Andrea Manuello Bertetto
PhD Eng. Elvio Bonisoli

*Dept. of Mechanics
Technical University - Politecnico di Torino
C.so Duca degli Abruzzi, 24.
10129 - Torino - Italy - E.C.*

www.jomac.it
e_mail: jomac@polito.it

Subscription information

Subscription order must be sent to the publisher:

*Libreria Editrice Universitaria
Levrotto&Bella
2/E via Pigafetta – 10129 Torino – Italy*

www.levrotto-bella.net
e_mail: info@levrotto-bella.net
tel. +39.011.5097367
+39.011.5083690
fax +39.011.504025

MOTION PRINCIPLES AND CONTROL OF A HUMAN RIDING TYPE ROBOTIC UNICYCLE (PART 1, MECHANISMS, STABILITY PRINCIPLES AND SIMULATION)

Hisanobu Suzuki*

Shunji Moromugi**

Kazuo Yamafuji***

* Olympus Inc., 1-18-1 Kuboyama-cho, Hachioji, Tokyo, 192-0023 Japan, lassih@ybb.ne.jp.

** Dept. of Mechanical Systems Engineering, Nagasaki University,
1-14 Bunkyo-machi, Nagasaki-shi, 852-8521 Japan, smoromug@nagasaki-u.ac.jp.

*** University of Electro-Communications, 3-10-14 Matsubara, Setagaya, Tokyo, 156-0043 Japan,
kazyama@r2.dion.ne.jp.

ABSTRACT

Driving a unicycle by automatic control has long been an interest of many researchers. This paper presents the successful development and motion control of a robotic unicycle emulating human riding a unicycle. The unicycle is consisted of a body supported on a single wheel, a closed linkage on each side of the body to drive a wheel, and a rotor on the top of the body. Part 1 of the study focuses on the unicycle design, stability principles and control algorithms. The effects of the closed link mechanism, the gyro-effect, the centrifugal force and the reaction torque of the rotor on the unicycle stability are also investigated. Computer simulation demonstrates stable driving of the robotic unicycle. The experimental evaluation, velocity and direction control of the robot will be presented in Part 2 of this study.

Keywords: Unicycle, Mechanisms, Stability principle, Control, Simulation

1 INTRODUCTION

A unicycle is an inherently-unstable system in three dimensions. As shown by a human riding a unicycle, the rider needs to perform complicated motions in order to maintain postural stability of the unicycle and drive it following a desired route. Motions of a unicycle can be grouped into four types, i.e., rotation of the wheel, forward and backward motion in the pitch (longitudinal) direction, motion toward right and left in the roll (lateral) direction, and motion around the plumb line in the yaw direction.

Ozaka et al [1] analyzed the postural stability of an inverted pendulum type unicycle and succeeded its stable control.

They considered that the rotation of the wheel and the lateral displacement of a mass act independently of each other. Honma et al [2] developed a gyro-unicycle that was equipped with a gyro-rotor on the top of the body to achieve the postural stability. Although its stability was maintained by controlling the gyro-moment of the rotor, it is a quite different system from that of inherently-unstable unicycle.

Feng and Yamafuji [3] modeled a unicycle as a wheeled inverted pendulum, developed control algorithms and investigated the stability under external disturbances. Yamafuji and Inoue [4] developed a unicycle with double control arms on the both side of an inverted pendulum type body. It succeeded in maintaining its upright position about 12~13 s. but failed in driving. Kawaji et al [5] attempted to stabilize a unicycle using spin effect by jerking a weight on the body.

Inspired by the gyro-unicycle by Honma et al [2], Schoonwinkel [6] developed a unicycle composed of a wheel, a body and an overhead turn-table and reported the its structure, the theoretical analysis of stability through the

Contact author: Shunji Moromugi

1-14 Bunkyo-machi, Nagasaki-shi, 852-8521 Japan,
E-mail: smoromug@nagasaki-u.ac.jp.

linearized equations of motion, and successful driving of the robot. Vos and Flotow [7] followed Schoonwinkel's model and applied an adaptive control rule to the model to deal with the nonlinear problem based on the linearized dynamic equations.

Learning the lessons from the previous studies, Sheng and Yamafuji [8], [9], [10], [11] concluded that the accurate modeling of the dynamics of a human riding unicycle is essential for successful development of a human riding type unicycle robot. Based on the observation of human riding a unicycle, they developed a new type of a unicycle. It employs double closed four-link mechanisms to emulate a human body, thighs, shanks and pedals to drive a wheel. In addition, an overhead rotor is installed on the top of the body. The function of the rotor, however, is completely different from the gyro-rotors used in the previous studies. The reaction torque of the rotor emulates the twist of the rider's torso, shoulders and arms for stability control.

Sheng and Yamafuji succeeded in maintaining postural stability and driving of this robotic unicycle in experiments. However, the stability and drive principles of the unicycle were not quantitatively evaluated. Control of the direction and driving speed was not achieved. Functions of the link mechanisms, the overhead rotor and the wheel were not made clear. The cable linking the unicycle to its power supply and a PC controller interfered the movement of the robot.

The objectives of this study including Part 1 and 2 are (1) to develop an upgraded autonomous unicycle robot without extension cables, (2) to investigate the stability and drive principles and control algorithms, (3) to realize direction control of the robot and driving with specified velocity, and (4) to clarify the role of each element.

2 ROBOTIC UNICYCLE DEVELOPED IN THIS STUDY

2.1 MECHANISM AND DRIVING SYSTEM

Figure 1 shows the autonomous robotic unicycle developed in this study. Similar to the previous one developed by the same research group [8], [9], [10], [11], this unicycle is equipped with a closed four-link mechanism (crank) on each side of the body and an overhead rotor. However, this prototype represents major improvements over the previous one. First, a battery and a computer are installed inside the body, and as a result no cable interferes the movement of the unicycle. Second, the unicycle wheel is driven only by the two DC servomotors on the double links, while the previous prototype required an extra motor. Each prototype of the robot equips the same overhead rotor driven by a DC servomotor. Each motor is 60W with a rotary encoder (resolution, $500p/rev$). Three reduction gears are utilized, two for the crank (ratio, $1/18$) and one for the rotor (ratio, $1/10$).

2.2 COMPUTER AND CONTROL SYSTEM

As a controller, *CARD-486D4* (with a clock frequency; $75MHz$) is used and the software is written in "*TurboC++language*". All the motors, including two for the wheel rotation through closed link mechanism actuation and one for the rotor rotation, are driven by torque commands. Battery is composed of 12 pieces of high-capacity cadmium-nickel batteries connected in series. Mass, nominal-voltage and electric capacity of the battery are about $1.9kg$, $14.4V$ and $5,000mAh$, respectively. The robot can be driven for approximately 15min continuously without battery recharging. Three rate gyro-sensors

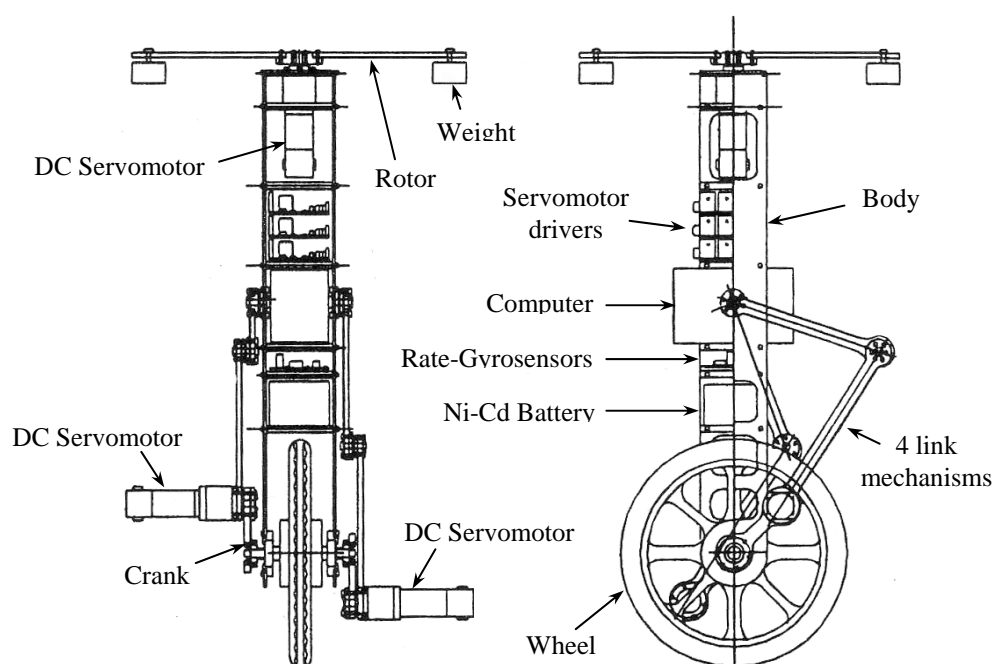


Figure 1 The developed unicycle robot

(produced by MURATA Inc.) are installed to detect robot posture angles including pitch-, roll- and yaw-angles. Commands for starting or stopping the unicycle are given by an external remote controller (one chip RISC – microcomputer) using an infrared ray.

3 STABILITY PRINCIPLE IN THE PITCH DIRECTION

The postural stability of the unicycle in the pitch (forward/backward) direction is achieved by pedaling the wheel, while the stability in the roll (left/right) direction by rotating the rotor and wheel. Therefore, we can analyze the motions in the pitch and roll directions independently. A 2D model of the unicycle composed of a body, a wheel and a closed linkage is shown in Fig. 2.

3.1 EQUATIONS OF MOTION

Equations of motion are derived based on the following steps.

1. Choosing the closed linkage A1-B-C-D in Fig. 2, we cut the joint B that is not powered by the motor, and as a result A1-B and B-C-D become open links.
2. Equations of motion for the open link mechanisms (cutting off the link 1, 2 and 3, 4 by the joints B and E in Fig. 2) are derived by Lagrange's differential equations as follows.

$$\frac{d}{dt} \left(\frac{\partial L}{\partial \dot{q}_i} \right) - \frac{\partial L}{\partial q_i} = \sum_{j=1}^k \mu_j \delta_{ij} + Q_i \quad (1)$$

(for $i=1,2,\dots,6$ and $k=1,2,\dots,6$)

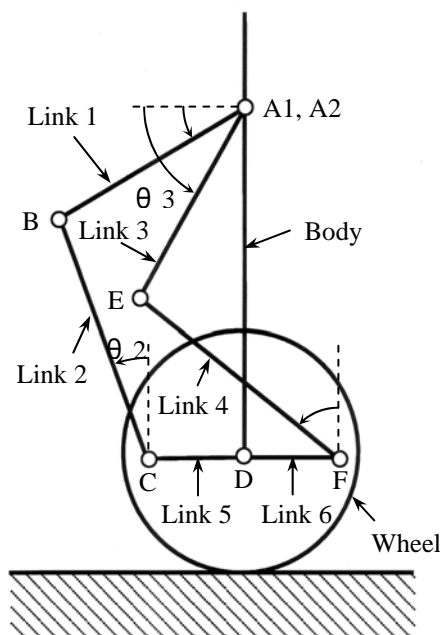


Figure 2 2D Model in the pitch direction

where, q_i are generalized coordinate, Q_i are generalized forces, δ_{ji} are terms given by Eq. (2).

$$\delta_{ji} = \frac{\partial \xi_j}{\partial q_i} \quad (2)$$

where, ξ_j are the constraints of the system.

Translation velocity V of the wheel is given by

$$V = r_w \dot{\psi} = \dot{x}_0 \quad (3)$$

where, r_w is radius of the wheel, $\dot{\psi}$ is angular velocity of the wheel, and x_0 is moving coordinate of the wheel.

Assuming that the wheel rolls without slippery, the constraint between the wheel and the ground is given by

$$x_0 = r_w \psi \quad (4)$$

Using Eq. (3) and its derivatives, the equations of motion for the open links are given by Eq. (5).

$$M(q)\ddot{q} + B(q)[\dot{q}\dot{q}] + C(q)[\dot{q}^2] + D(q)[\dot{q}] + G(q) = \tau \quad (5)$$

where, $\tau = (\tau_\psi, \tau_\beta, \tau_{\theta_1}, \tau_{\theta_2}, \tau_{\theta_3}, \tau_{\theta_4})^T$ are torques for the open links, $M(q)$ is 6×6 mass matrix, $B(q)$ is Coriolis's terms, $[\dot{q}\dot{q}]$ are product of the velocity vector terms, $D(q)$ is 6×6 friction force matrix, $[\dot{q}] = (\dot{\psi}, \dot{\beta}, \dot{\theta}_1, \dot{\theta}_2, \dot{\theta}_3, \dot{\theta}_4)^T$, $G(q)$ is the 6×1 gravity vector, and $q = (\psi, \beta, \theta_1, \theta_2, \theta_3, \theta_4)^T$. $\theta_1, \theta_2, \theta_3$ and θ_4 are given in Fig.2.

3. The actual robot employs two closed, rather than open linkages whose equations of motion can be considered as four constraints added to the open links, shown as follows.

$$\tau + \left(\frac{\partial c}{\partial q} \right) \lambda = M(q)\ddot{q} + B(q)[\dot{q}\dot{q}] + C(q)[\dot{q}^2] + D(q)[\dot{q}] + G(q) \quad (6)$$

where, $\frac{\partial c}{\partial q}$ is 4×4 matrix determined by the four constraints, and λ is Lagrange's multipliers.

4. Using constraints for the acceleration of the closed linkages, equations of motion for the robotic unicycle are obtained [12].

3.2 2D COMPUTER SIMULATION OF UNICYCLE DRIVING

Simulation on driving of the 2D robot model with the closed links is carried out using MATLAB. The motor driving the wheel is controlled by a torque command to maintain the upright posture of the robot body. The control

torque input U_{wheel} is computed on the PD control rule shown as follows:

$$U_{wheel} = k_{p1}\delta\beta + k_{d1}\delta\dot{\beta} \quad (7)$$

where, k_{p1} is proportional feedback gain (FBG), k_{d1} is differential FBG, $\delta\beta$ is deviation of the pitch angle from a target angle, and $\delta\dot{\beta}$ is differential of $\delta\beta$.

Inputting the above torques (in practice, electric current derived from dividing the torque by torque-coefficient of the motor) respectively into the two motors installed on the joints connecting links 1 and 2, and links 3 and 4, the wheel starts to rotate and the robot advances in the pitch direction.

Simulation results are given in Fig. 3, with time histories of the wheel's rotation distance in Fig. 3 (a), the pitch angle in Fig. 3 (b) and the torque input for the wheel in Fig. 3 (c). Figure 3 demonstrates successful driving of the 2D unicycle while maintaining its postural stability, although the pitch angle oscillates in the advancing direction.

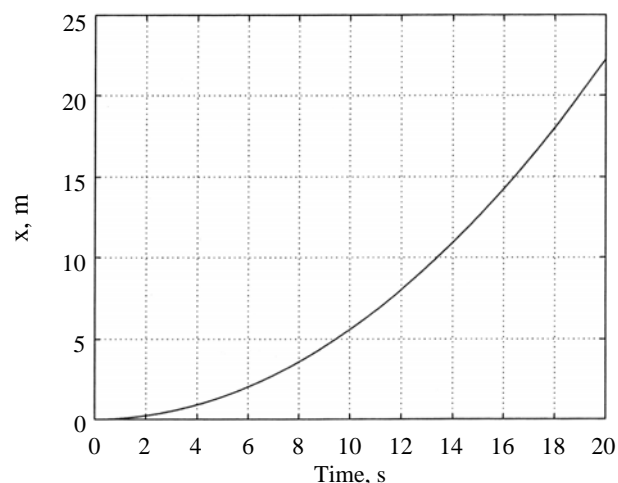
This suggests that the stability of the unicycle can be achieved by controlling the wheel. The drive principles of the 2D robot can be summarized as follows based on the observations in Fig. 4.

1. We set the target pitch angle slightly larger than zero in the advancing direction. As a result, the body tends to fall forward due to the gravity moment.
2. The wheel is accelerated forward to decrease the body inclination.
3. When the robot reaches the target pitch angle, the wheel would stop accelerating, but the body tends to fall again due to the gravity moment.
4. Again the robot wheel is accelerated to restore the stable body posture.
5. The robot advances forward by repeating above sequence.

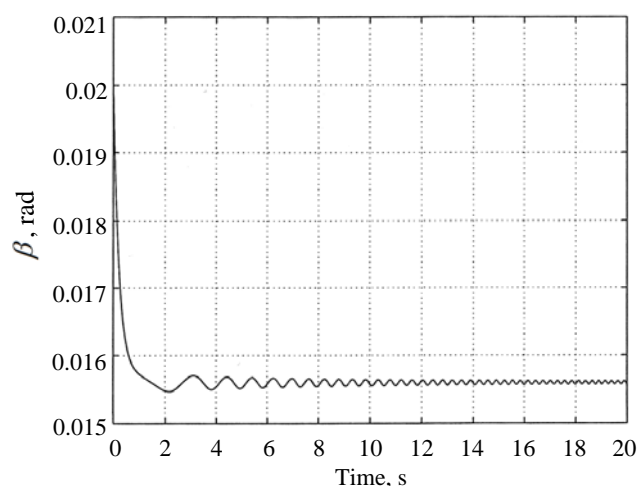
Therefore, the wheel is always accelerated to move forward and the acceleration can be computed as illustrated in Fig. 5. The gravity moment $mg\sin\beta$ letting the robot fall must be balanced by the inertial moment $mal\cos\beta$, from which the wheel's acceleration is derived as $a = g \tan\beta$. Namely, the more the pitch angle increases, the more acceleration of the robot is required.

3.3 EFFECT OF THE CLOSED LINK MECHANISMS ON THE UNICYCLE

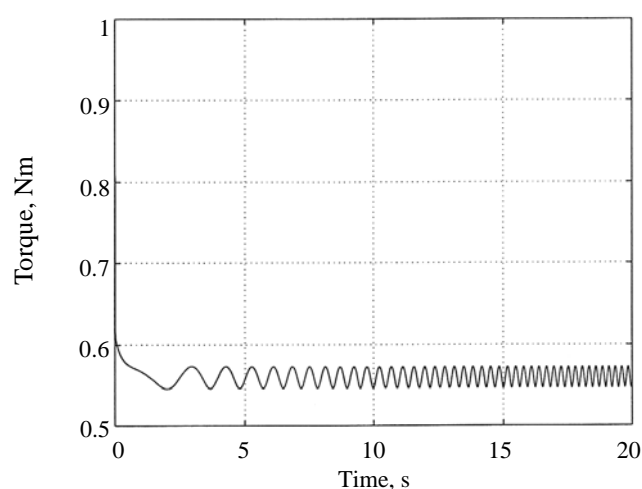
The unicycle's wheel is driven by the two motors mounted on the cranks of the closed linkages. In order to investigate the effect of the closed linkages on the body, a computer model is developed, in which the wheel is fixed on the ground without moving the wheel and the body can rotate around the wheel axis. By this model, the torque provided by the motors via linkages is fully utilized to rotate the body.



(a) Wheel rotation distance



(b) Pitch angle



(c) Input torque for the wheel

Figure 3 Time histories of the simulation results of 2D model

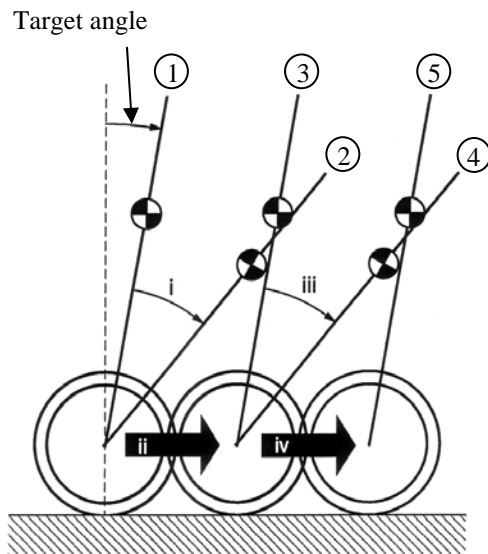


Figure 4 Stability and drive principle in the pitch direction

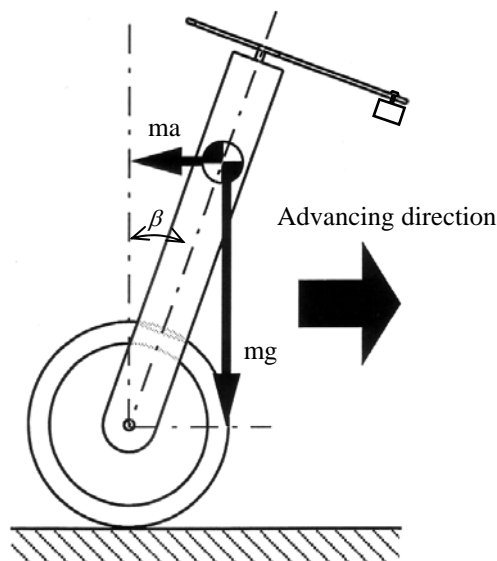


Figure 5 Force and moment balance in the pitch direction

Motion simulation is conducted by applying the torque to each of the two joints between link 1 and 2, and link 3 and 4. The same PD control rule is applied to maintain approximately the zero pitch angle. Simulation results in Fig. 6 shows that the torque was insufficient to maintain the upright posture of the body and it fall down. Therefore larger motor torque beyond the torque capacity of $4Nm$ is needed to maintain the pitch angle within $0.02rad$. On the other hand, motor torque needed to rotate the wheel is at most $0.6 Nm$ as seen in Fig. 3 (c).

This implies that the body's stability cannot be achieved with the same torque that successfully drove the 2D robot in the preceding section. From the simulation results, we can guess that effect of the motor torque on the body is

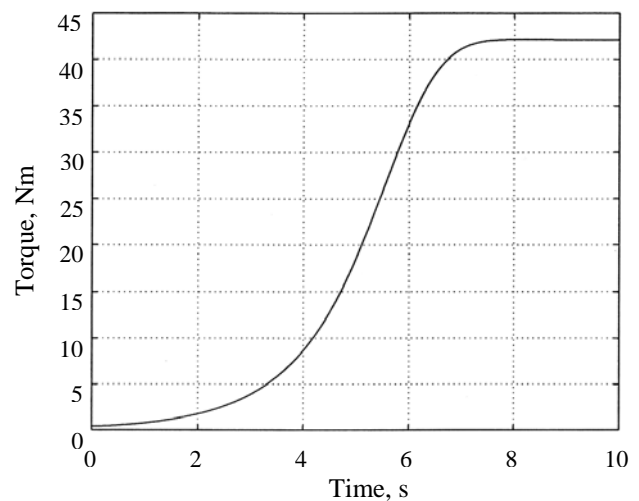
small and almost all the motor torque is used for rotation of the wheel. Therefore, the effect of the closed linkages on the body stability is not so large.

4 STABILITY PRINCIPLE IN THE ROLL DIRECTION

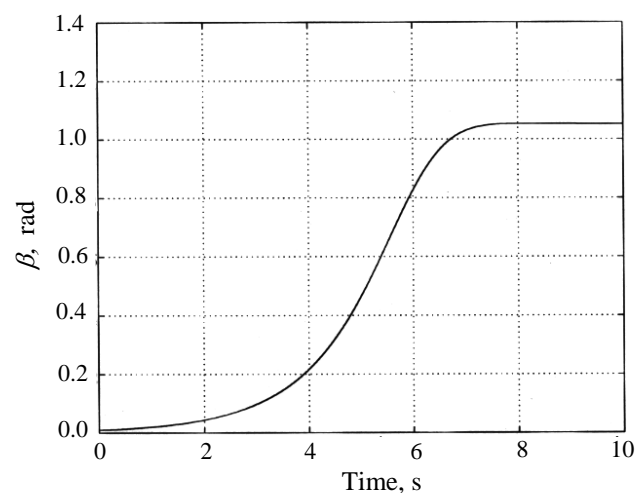
Sheng and Yamafuji [10], [11] reported that the stability of the robotic unicycle in the roll direction could be attained by rotating the overhead rotor in the opposite direction of the inclination of the body. However, they did not give the evidence. In this study, we analytically investigated the stability of the unicycle in the roll direction, particularly, (1) the gyro-effect of the rotor rotation, (2) the gyro-effect of the wheel rotation and (3) the effect of turning the advancing direction of the body.

4.1 GYRO-EFFECT OF THE ROTOR ROTATION WHEN THE WHEEL IS FIXED

In order to investigate the effect of the rotor rotation on the unicycle stability in the roll direction, a 2D model is



(a) Torque



(b) Pitch angle

Figure 6 Time history of input torque and pitch angle

developed to deal with the inclination of the robot body in the roll direction. This model consists of an inverted pendulum (robot body) with its wheel fixed and a rotor mounted on the pendulum. The pendulum can incline in the roll direction as shown in Fig. 7.

Considering the reality that the compound center of gravity (hereafter, CCG) [13] is unlikely located exactly in the geometrical center of the unicycle robot, two additional models are also developed for simulation, in which CCG is slightly shifted either in the pitch or in the roll direction. Setting the target roll angle of the body as $\gamma = 0$, the control input to the rotor U_{rotor} is computed as

$$U_{rotor} = k_{p2}\delta\gamma + k_{d2}\delta\dot{\gamma} \quad (8)$$

where, k_p is proportional feedback gain (FBG), k_d is differential FBG, $\delta\gamma$ is deviation from the target roll angle, and $\delta\dot{\gamma}$ is differential of $\delta\gamma$.

As shown in the simulation results in Fig. 8 (a), the pendulum fell down in spite of rotation of the rotor. Parametric study is performed to test a large range of control gains, but none of them can achieve the postural stability of the unicycle in the roll direction, even when the rotor angular velocity reaches as high as 20rad/sec as seen in Fig. 8 (c). The gyro-effect is not sufficient to restore the body inclination. Thus the rotation of the rotor itself does not contribute to the stabilization of the body. Apart from the gyro-effect, the rotor does play an important role in the robot stability in the roll direction when the wheel is not fixed, as described in the following Section 4.4.

4.2 EFFECT OF THE CENTRIFUGAL FORCE

The rotation of the rotor causes the robot body to meander, producing a centrifugal force on the robot. To examine the effect of the centrifugal force, a 3D model of the robot is contrived and the robot motion in the pitch-, roll- and yaw-directions is considered. Investigations in Section 3.3 made it clear that the effect of the closed linkages of the body was insignificant in comparison with the torque rotating the wheel. So, we consider a 3D model composed of the wheel, body and rotor without the linkages. Simulation on the posture stability and drive was conducted using the controllers in Eqs. (7) and (8).

Simulation results in Fig. 9 show stable driving of the unicycle. The roll-, pitch- and yaw-angles are stabilized within 3sec after starting as observed in Fig. 9 (a), (b) and (c). The driving trajectory in Fig. 9 (d) shows meandering until the robot attained the stability. Figure 10 shows the trajectories of CCG and the contact point (hereafter, CP) of the robot with the ground at a time interval of 0.1sec. Symbol (o) in the figure indicates location of CCG and CP at every 1sec. From the enlarged Fig. 10 (a), CCG is always ahead of CP in the advancing pitch direction, which implies that the robot inclines forward. Although the trajectory of CP meanders at the starting period in Fig. 10 (a), that of CCG is almost linear. This implies that no centrifugal force is produced.

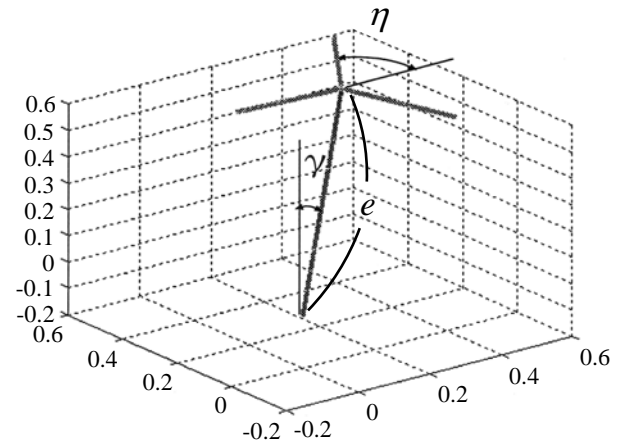


Figure 7 Inverted pendulum model inclined to the roll direction only

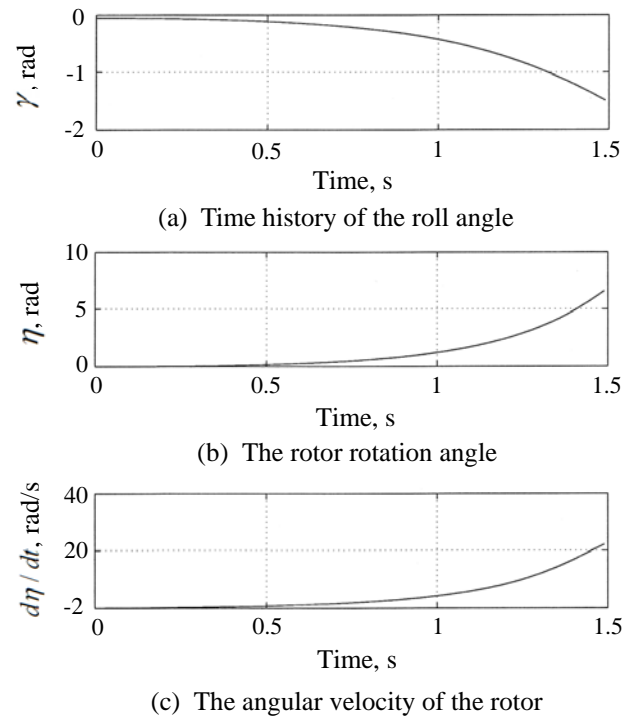


Figure 8 Influence of the rotor rotation, simulation results of 2D model

4.3 COMBINED GYRO-EFFECT BY THE WHEEL AND ROTOR ROTATION

The wheel and rotor rotation may produce the combined effect on posture and drive of the unicycle. There exists a relationship given by Eq. (9) between the gyro-moment M_g , wheel's angular velocity ω_w , rotor's angular velocity ω_r and inertial moment I of unicycle around the gravity center of the body in the roll direction.

$$M_g = I\omega_w\omega_r \quad (9)$$

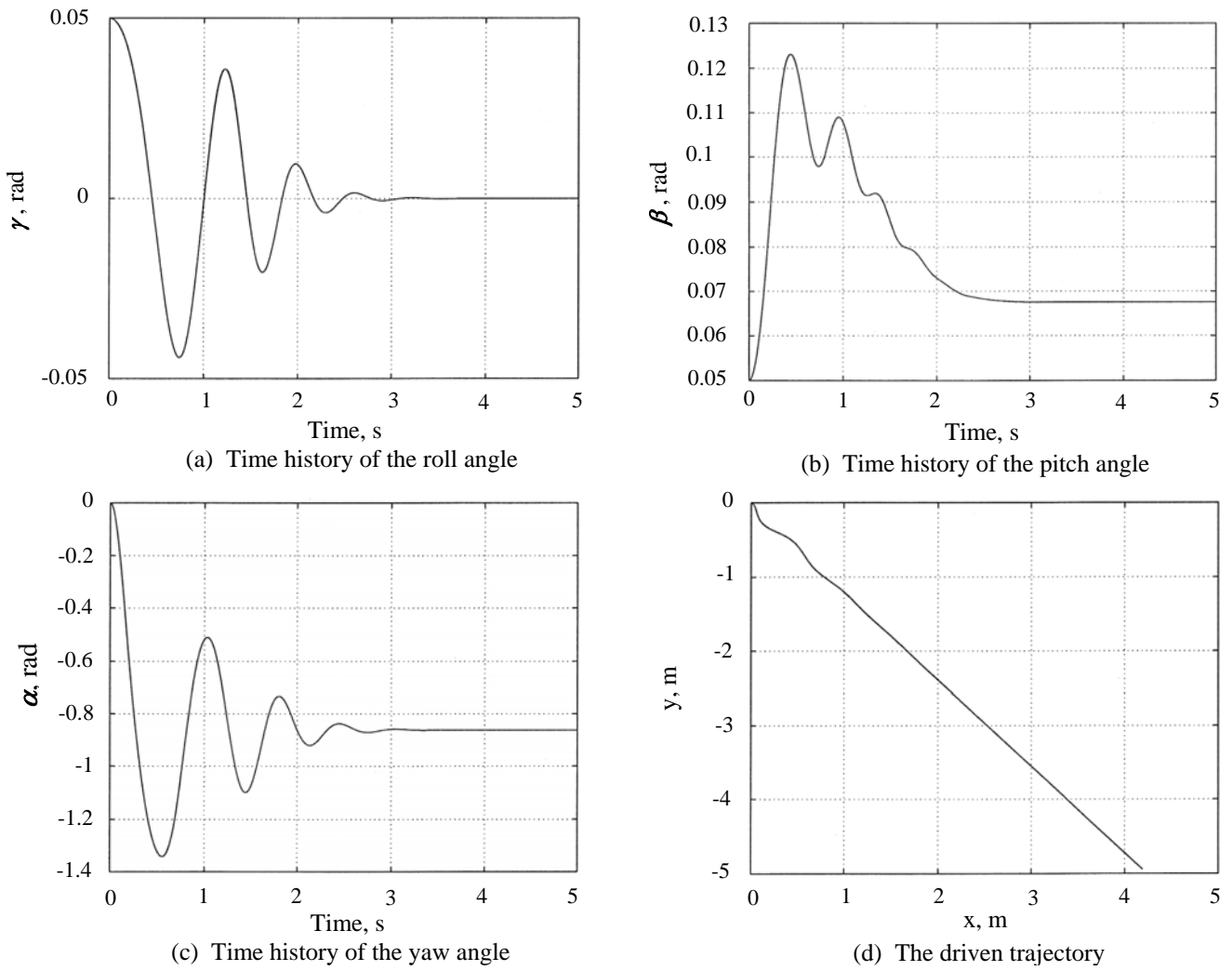


Figure 9 Simulation results on 3D model

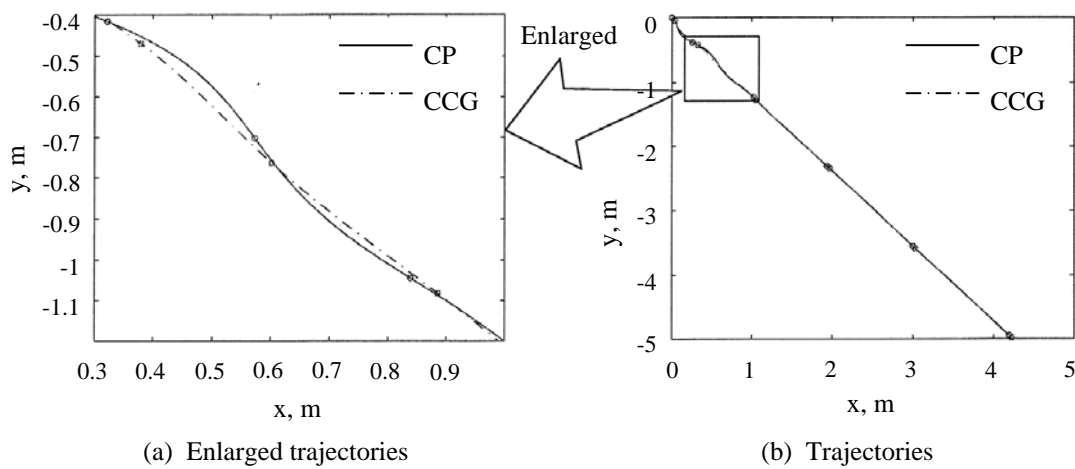


Figure 10 Trajectories of CP and CCG, influence of the centrifugal force

When the unicycle that is advancing straight inclines to the right, the wheel and the body turn to the right by the gyro-effect. However considering Eq. (9), the gyro-effect is so small just after the unicycle starts moving since the rotation of the wheel is not large during that period. The combined gyro-effect is enhanced as the wheel's angular speed increases. Thus we can neglect the combined gyro-effect in this study.

4.4 EFFECT OF VARYING ADVANCING DIRECTION

Quick rotation of the overhead rotor lets the unicycle rotate in the yaw direction. As a result, the advancing direction of the unicycle is varied. The effect of change in advancing direction on the postural stability was investigated by 3D computer simulation. The control rules and parameters were the same as those used in Section 4.2. Trajectories of CP and CCG obtained by the simulation are shown in Fig. 11. The enlarged graph in Fig. 11 (a) indicates that the unicycle is advancing to the right. The time history of the motion in the advancing (pitch)- and posture inclination (roll)- directions can be expressed by the vectors on the plane as shown in Fig. 12. The unicycle stabilizes the posture by changing the advancing direction toward the inclined direction, such a motion is observed often in human riding a bicycle. The stability of the unicycle in the roll direction is achieved by both rotations of the wheel (as explained in Section 4.3) and the rotor as shown in Fig. 13. In order to examine whether the wheel rotation is needed to stabilize the posture in the roll direction, a new model is tested in which a motor torque is applied to the rotor but not to the wheel. By this model we can examine if the wheel's rotation is necessary or not for stability of the unicycle in the roll direction. Simulation was carried out under the following initial conditions, $\beta_0 = 0 \text{ rad}$ for the pitch angle (because the 3D model has no closed linkages), and $\gamma_0 = 0.05 \text{ rad}$ for the roll angle.

From the simulation results shown in Fig. 14, the following explanations of motion stability in the roll direction can be made.

- Just after the start, the rotor begins to rotate, changing the yaw angle of the robot body.
- The pitch angle β that is zero at the start begins to incline largely in accordance with the body rotation in the yaw direction. On the contrary, the roll angle γ converges to zero. This indicates that the inclination of the body in the roll direction is compensated (replaced) by the inclination in the pitch direction because of the rotation of the body in the yaw direction. Thus, in order to stabilize the posture in the roll direction, the body turns to the roll direction. Then the inclination of the body in the roll direction decreases and is replaced by the inclination in the pitch direction.
- The wheel rotates to restore the postural stability in the pitch direction. Thus the robot advances in the pitch direction to which the body is inclining.

4.5 BODY ROTATION ANGLE NECESSARY FOR STABILIZATION

From the preceding analyses, it is confirmed that rotation of the body in the yaw direction is necessary for the robot posture stabilization in the roll direction. Here, the magnitude of the necessary rotation angle θ_{rel} is derived from the relationship between the pitch-, roll- and yaw-angles. First, the plain view of the unicycle's coordinates with the origin O is shown in Fig. 15. The position (x_b, y_b) of the body top is computed as follows.

$$\left. \begin{aligned} x_b &= e \cos \alpha \sin \beta + e \sin \alpha \cos \beta \sin \gamma \\ y_b &= e \sin \alpha \sin \beta - e \cos \alpha \cos \beta \cos \gamma \end{aligned} \right\} \quad (10)$$

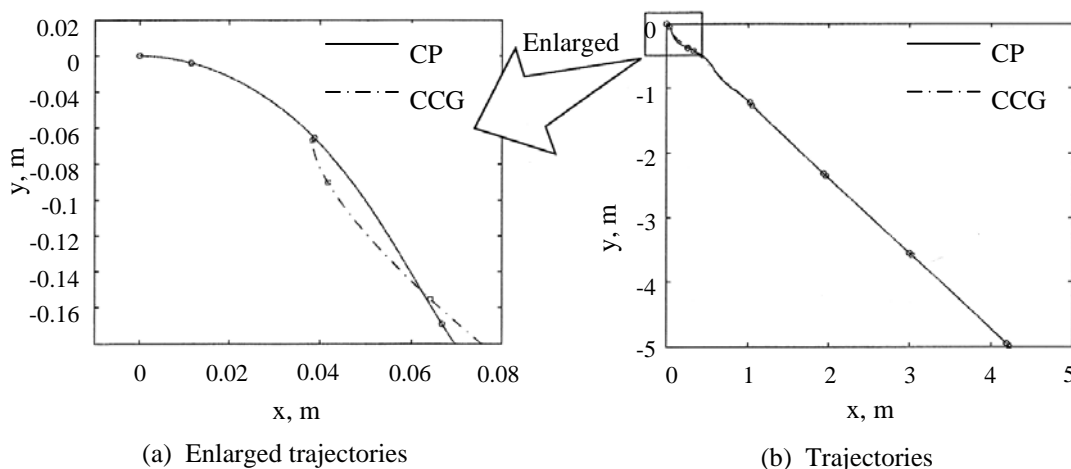


Figure 11 Trajectories of CP and CCG, influence of the advancing direction

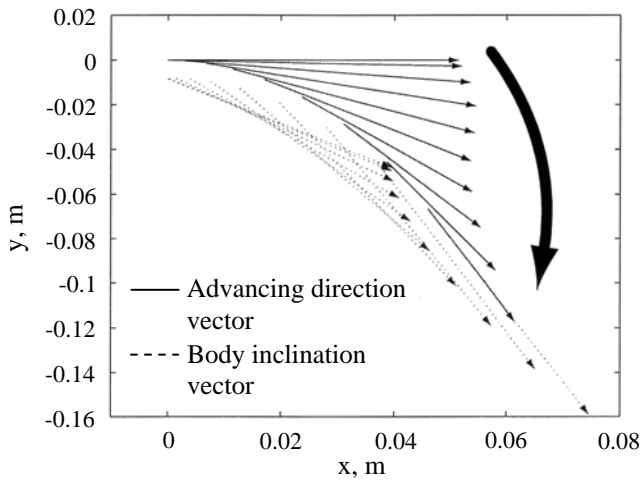


Figure 12 Vectors expression for the advancing direction and body inclination

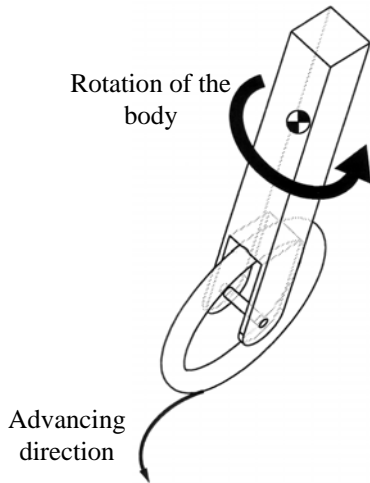


Figure 13 Stability principle in the roll direction

where, α , β and γ are yaw-, pitch- and roll-angle, respectively. e is the body length. The angle θ_b between the x axis and the body inclination vector projected on the ground shown in Fig. 15 is

$$\theta_b = \tan^{-1}(y_b / x_b) \tag{11}$$

The relative angle between θ_b and α is

$$\theta_{rel} = \theta_b - \alpha = \tan^{-1} \frac{\sin \alpha \sin \beta - \cos \alpha \cos \beta \cos \gamma}{\cos \alpha \sin \beta + \sin \alpha \cos \beta \sin \gamma} - \alpha \tag{12}$$

The unicycle's rotation by θ_{rel} (in Fig. 15) and its driving in the pitch direction are closely related to the stability in the roll direction. The fundamental motion characteristics of the unicycle are summarized as follows,

a. The reaction torque caused by rotation of the rotor makes the body rotate around the yaw axis, altering the

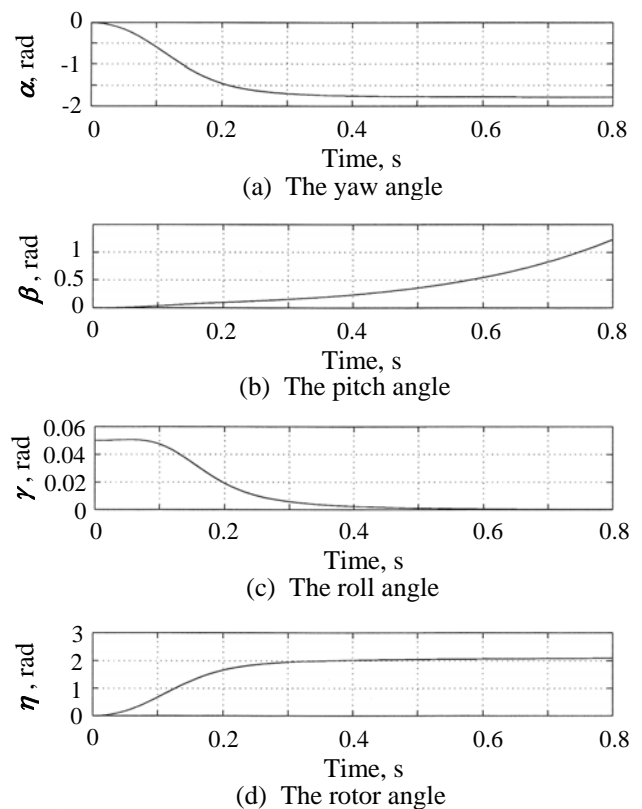


Figure 14 Time history of the robot's angles, simulation result in 3D

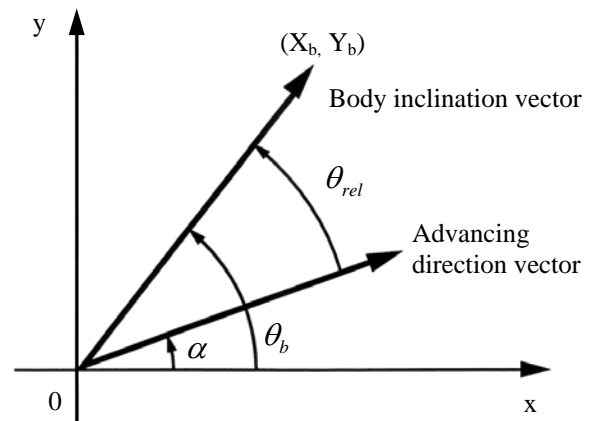


Figure 15 Relation between the body inclination and the advancing direction

unicycle's advancing direction. Rotation of the body by the amount θ_{rel} around the Z axis compensates the inclination and restores the posture in the roll direction.

b. On the contrary, as the body rotates around the yaw axis to stabilize the posture in the roll direction, the inclination in the pitch direction is also induced by the body rotation around the yaw axis. The inclination in the pitch direction is then compensated by rotating the wheel. As a result, the postural stability of the robotic unicycle in both the pitch and roll directions is attained.

5 CONCLUSIONS

A robot is developed emulating human riding a unicycle. The stability and drive principles of the robotic unicycle in the pitch- and roll-directions are investigated using 2D-, 3D-models and computer simulation. The conclusions are summarized as follows;

- a. The stability of the robot in the pitch direction is achieved by controlling the wheel. When the body inclines forward, the wheel is accelerated forward to restore the pitch angle back to a target value that is slightly larger than zero. As the robot reaches the target pitch angle, the body tends to fall due to the gravity force, and the robot is accelerated again to restore the stable posture. The robot advances forward by repeating above sequence.
- b. The stability of the robot in the roll direction is achieved by the rotation of the robot around the yaw axis, which is caused by rotation of the wheel and the overhead rotor. Just after the robot starts moving, the rotor starts to rotate, causing the robot to rotate around the yaw axis. As a result, inclination of the body in the pitch direction is induced, which compensates the inclination in the roll direction and attains the postural stability in the roll direction.
- c. The inclination in the pitch direction is then compensated by rotating the wheel. In this way, the postural stability of the robot in the pitch- and roll-directions is achieved. In other words, both the wheel and the overhead rotor play an important role in the stabilization of the robot.
- d. The closed double link mechanisms do not contribute to the stabilization of the unicycle more than rotating the wheel. The centrifugal force and gyro-moment of the rotor are insignificant. The function of the overhead rotor is to emulate the body turning of a human rider for stabilization in the roll direction.

Experimental results on postural stability, velocity and direction control of the robotic unicycle will be presented at Part 2 of this study. They verify the conclusions made in this paper.

REFERENCES

- [1] Ozaka C., Kano H. and Masubuchi M., "Stability of a Monocycle-Type Inverted Pendulum"(in Japanese), *3rd Vehicle Automation Symposium of Japan Automatic Control Society*, pp. 63-66, 1980.
- [2] Honma D., Iguchi N., Kondo Y., Michimori A. and Okubo H., "One Wheel-Locomotive Robot and Its Control"(in Japanese), *Journal of Robotic Society of Japan*, 2-4, pp. 366-372, 1983.
- [3] Feng Q. and Yamafuji K., "Design and Simulation of Control System of an Inverted Pendulum", *Robotica*, Cambridge Univ. Press, 6-2, pp. 235-241, 1988.
- [4] Yamafuji K. and Inoue K., "Study on the Posture Stability of a Unicycle"(in Japanese), *Preprint of the Yamanashi Meeting, Japan Society of Mechanical Engineering (JSME)*, pp. 4-6, 1986.
- [5] Kawaji S., Shiotsuki T., Matsunaga N. and Kisanuki M., "Stabilization of a Unicycle Using Spinning Motion"(in Japanese), *Transactions of Institute of Electrical Engineers of Japan*, 107-D-1, pp. 21-30, 1987.
- [6] Schoonwinkel A., "Design and Test of a Computer Stabilized Unicycle", Dissertation, Stanford University, 1987.
- [7] Vos D.W. and Von Flotow A.H., "Dynamic and Nonlinear Adaptive Control of an Autonomous Unicycle, Theory and Experiment", *Proc. 29th Conf. Decision Control*, pp. 182-187, 1990.
- [8] Sheng Z.Q. and Yamafuji K., "Study on the Stability and Motion Control of a Unicycle (Part 1, Dynamics of human riding unicycle and its modeling by link mechanisms)", *JSME Intern. Journal*, Series 3, 38-2, pp. 249-259, 1995.
- [9] Sheng Z.Q. and Yamafuji K., "Study on the Stability and Motion Control of a Unicycle (Part 2, Design and experimental results of a unicycle robot)"(in Japanese), *Trans. JSME*, 61-583C, pp. 1042-1049, 1995.
- [10] Sheng Z.Q. and Yamafuji K., "Study on the Stability and Motion Control of a Unicycle (Part 3: Characteristics of a unicycle)", *JSME Intern. Journal*, Series 3, 39-3, pp. 560-568, 1996.
- [11] Sheng Z.Q. and Yamafuji K., "Postural Stability of a Human Riding a Unicycle and Its Emulation by a Robot", *IEEE Trans. on Robotics and Automation*, 13-5, pp. 709-720, 1997.
- [12] Suzuki H., "Study on the Drive Principles and Control of the Unicycle" (in Japanese), Master Theses, University of Electro-Communications, 2001.
- [13] Hirabayashi T. and Yamafuji K., "Posture and Driving Control of a Variable Structure Type Parallel Bicycle (1st Report, Posture stabilization and drive control of the arm-wheel model)"(in Japanese), *Trans. JSME*, 56-523C, pp. 721-730, 1990.

MOTION PRINCIPLES AND CONTROL OF A HUMAN RIDING TYPE ROBOTIC UNICYCLE (PART 2, MOTION PRINCIPLES, DIRECTION CONTROL, EXPERIMENTS AND SIMULATION)

Hisanobu Suzuki*

Shunji Moromugi**

Kazuo Yamafuji***

* Olympus Inc., 1-18-1 Kuboyama-cho, Hachioji, Tokyo, 192-0023 Japan, lassih@ybb.ne.jp.

** Dept. of Mechanical Systems Engineering, Nagasaki University,
1-14 Bunkyo-machi, Nagasaki-shi, 852-8521 Japan, smoromug@nagasaki-u.ac.jp.

*** University of Electro-Communications, 3-10-14 Matsubara, Setagaya, Tokyo, 156-0043 Japan,
kazyama@r2.dion.ne.jp.

ABSTRACT

The stability and drive principles of the robotic unicycle proposed in our previous paper were verified by experiments in this paper. The robot is accelerated or decelerated depending on location of the compound center of gravity of the body. Inclination in the roll direction is compensated with that in the pitch direction by rotating the robot due to reaction torque of the overhead rotor. Based on the proposed acceleration control rule, the robot can run with a specified velocity. Combining the acceleration control rule and a specified yaw angular velocity, the direction control rule is proposed. Using that rule, drive simulation of tracing a circle and “8” character was carried out. Role of the overhead rotor rotation is very important. The robot can perform motions dynamically similar to those in human riding a unicycle.

Keywords: Unicycle, robot, motion principles, control, experiment, simulation

1 INTRODUCTION

In our previous paper [1], the stability and drive principles of the robotic unicycle in the pitch- and roll- directions were reported based on the simulation results. The stability of the robot in the pitch direction is achieved by controlling the wheel.

The stability in the roll direction is attained by rotating the robot around the yaw axis, which is caused by rotation of the wheel and overhead rotor. Quick rotation of the overhead rotor lets the robot rotate around the yaw axis. As a result, the advancing direction of the robot is varied. In this way, the postural stability of the robot in the pitch- and roll-directions is achieved. Both the wheel and overhead rotor play important roles in the stabilization of the robot.

Verification of the stability and drive principles reported in [Part 1] was done by the experiments in this paper. The control rules based on the stability and drive principles are proposed in order to drive the robot with a specified velocity and realize direction control. Then driving of the robot along an assigned route was conducted by computer simulation.

2 VERIFICATION OF THE STABILITY AND DRIVE PRINCIPLES BY EXPERIMENTS

2.1 EXPERIMENTAL METHOD AND RESULTS

Concerning to the stability and drive principles described in [Part 1], their validity is verified experimentally in this section. Using the fuzzy scheduling controllers by Sheng and Yamafuji [2], [3], experiments on driving the robotic unicycle were conducted. Experiments were carried out using the robot shown in Fig. 1 of [1]. To improve reproduction of the results, an apparatus for starting the

Contact author: Shunji Moromugi

1-14 Bunkyo-machi, Nagasaki-shi, 852-8521 Japan,
E-mail: smoromug@nagasaki-u.ac.jp.

robot (robot launcher) was made. By use of the robot launcher, the posture at starting is kept upright or maintained at a desired posture.

The experimental results on time histories of the roll-, pitch-, yaw-angle, and rotor rotation angle are given respectively in Figs. 1 (a), (b), (c) and (d). Variations of the pitch- and roll-angle are limited within 0.03 rad and ± 0.05 rad, respectively. Figure 1 (b) shows that the stable drive of the robot was realized. In comparing time history of the yaw angle with that of the rotor rotation angle, the yaw angle increases in the opposite direction of the rotor rotation as seen in Fig. 1 (c) and (d). The most important fact is that the inclination in the roll direction was incessantly corrected by increasing the yaw angle, i.e., by rotation of the robot around the yaw axis due to rotation of the overhead rotor.

Figure 2 shows time histories of the roll- and yaw-angular velocity. Fluctuations of Figs. 2 (a) and (b) show that they are closely related because the roll angle inclination and rotation of the robot around the yaw axis are linked as stated in [Part 1] and Section 2.2 of this paper. Time delay between them implies that the posture restoration by the rotor takes a time. Time history of torque output of the rotor is shown in Fig. 3. Comparing Fig. 1 (a) and Fig. 3, the fluctuating patterns of the roll angle and rotor torque resemble each other. The negligible time delay between them indicates that response of the torque command to the roll angle control is very quick. The wheel angle change shown in Fig. 4 means that rotation of the wheel is not constant but accelerated or decelerated.

2.2 VERIFICATION OF STABILITY AND DRIVE PRINCIPLES

Figure 5 shows trajectories of the compound center of gravity (hereafter, CCG) [4] and the contact point (hereafter, CP) of the robot with the ground. Figure 5 (a) illustrates an enlargement of the starting period in Fig. 5 (b). By investigating changes of the advancing direction vector and body inclination vector of the robot in the Fig. 5 (a), the former goes on to merge with the direction of the body inclination. Then the body restores the upright posture. It implies the very important fact that the robot restores the stable posture by rotation of the body around the yaw axis. Next, we notice the trajectories in the vicinity of a point ($x = 1.5\text{m}$ and $y = 0.8\text{m}$) on Fig. 5(b).

Relations between CP and CCG are demonstrated in Fig. 6. Examining the enlarged Fig. 6 (b), the trajectories of CP and CCG curve to the opposite direction each other. This indicates that the robot's postural stability is not attained by the centrifugal force. The reason why is that the force toward the right-lower direction in Fig. 6 (b), i.e., toward the trajectory of CP must act on CCG in order to restore the upright posture of the robot. If a centrifugal force acts on CCG in the trajectory shown in Fig. 6 (b), such a force does not act in the direction to restore the robot posture but in the opposite direction to put it down. This implies that the robot posture is not restored by the centrifugal force as it is suggested by the computer simulation in [1].

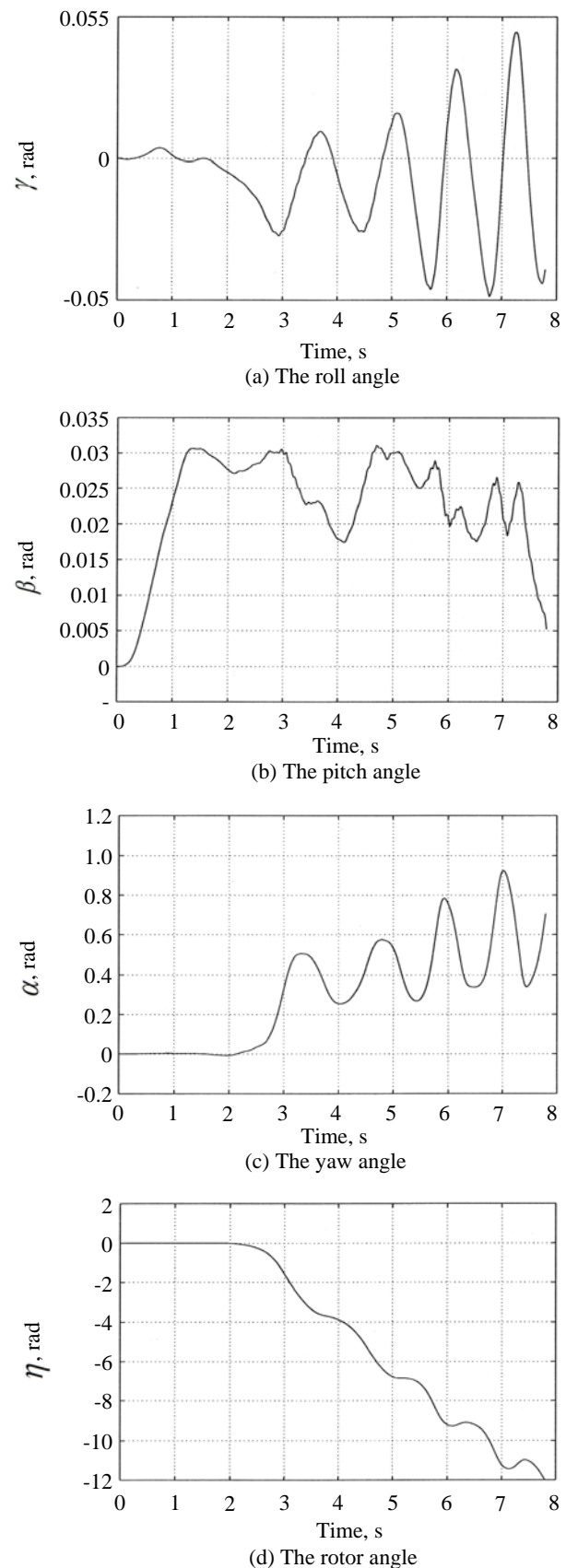
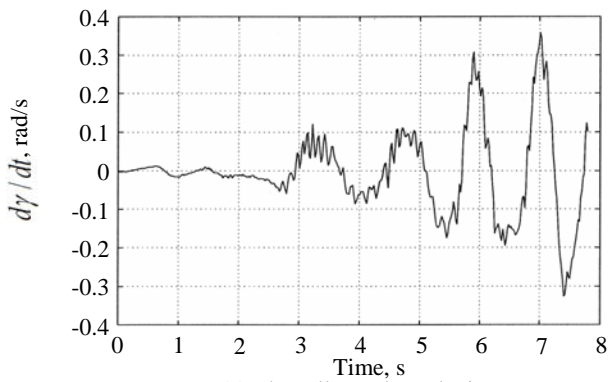
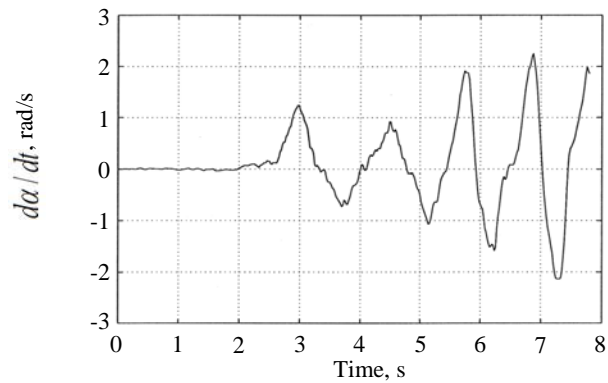


Figure 1 Time history of the robot's angles, experimental results.



(a) The roll angular velocity



(b) The yaw angular velocity

Figure 2 Time history of the roll- and yaw-angular velocity, experimental results.

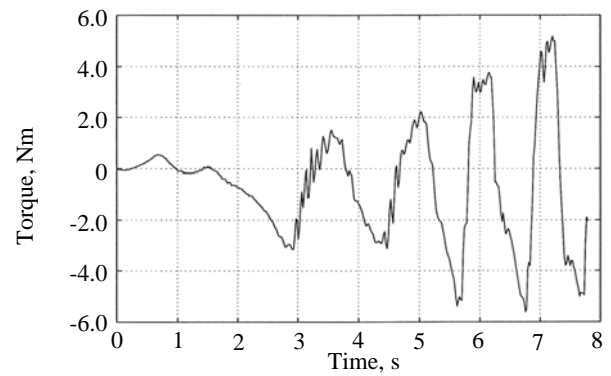


Figure 3 Time history of the torque output of the rotor.

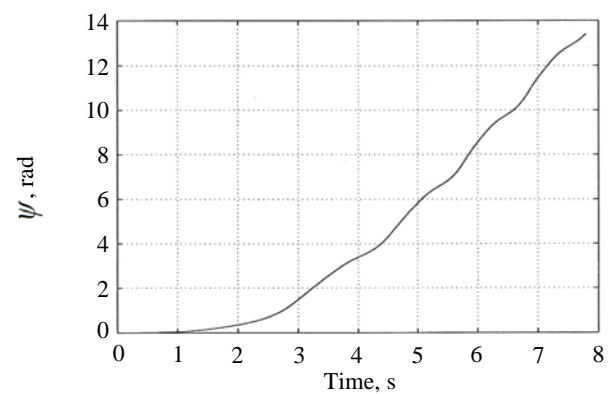
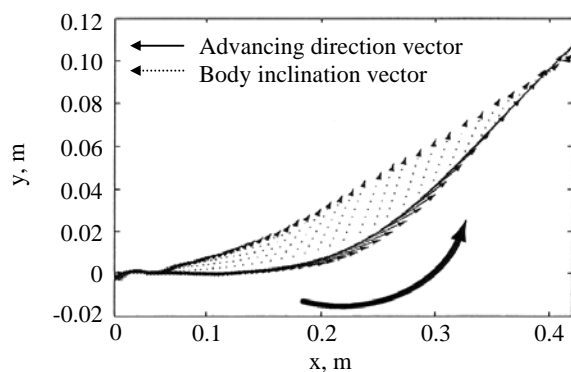
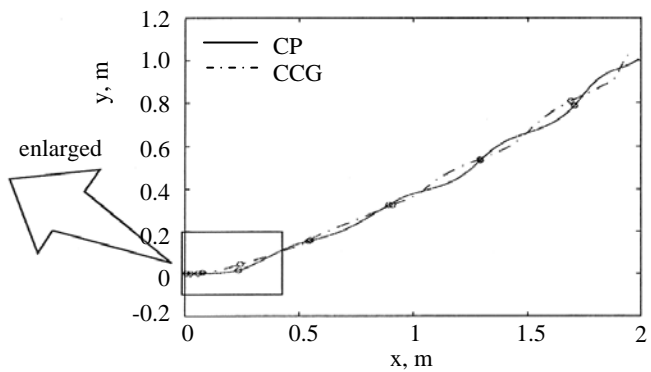


Figure 4 Time history of the wheel angle, experiment.

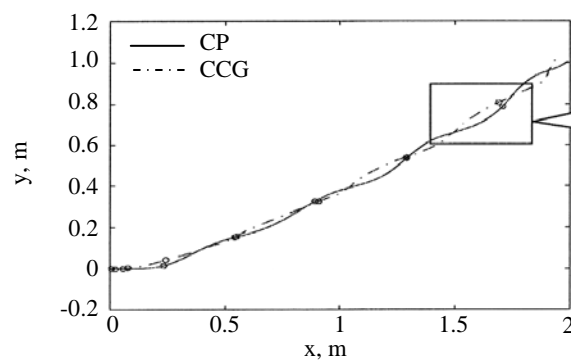


(a) Change of direction vectors

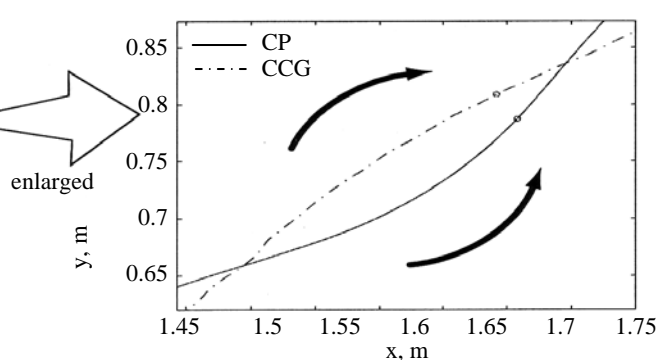


(b) Trajectories of CP and CCG

Figure 5 Change of direction vectors and trajectories.



(a) Trajectories of CP and CCG



(b) Enlargement of (a) in the vicinity of x=1.5

Figure 6 Relations between CP and CCG projected on the ground.

We verify the reason why CP and CCG curve to the opposite direction each other but the robot's posture can be restored. The wheel's advancing direction and the body's inclined direction in Fig. 6 (b) are expressed by vectors, and their time histories are shown in Fig. 7. It is confirmed that the advancing direction vector followed the body's inclined direction by simulation in [Section 4.4]. The advancing direction vector follows the body's inclined direction vector. However, it seems to the contrary that the body's inclined direction vector approaches more and more close to the advancing direction vector. The reasons can be expressed using Figs. 7 and 8. The following symbols (i), (ii), (iii), (iv), (v) and (vi) correspond to the same ones in both figures.

- (i) After the robot begins to start moving and runs over 1.5 s, CCG gets velocity vector V_{body} as shown in the Fig. 7.
- (ii) We define the wheel-coordinates in which the wheel's advancing direction and its vertical axis are x - and y -axis, respectively. Velocity vector V_{body} is decomposed in x - and y - direction. Since the robot has a velocity V_y on the y axis, we know that the robot tends to fall in this direction.
- (iii) If the advancing direction is varied by reaction torque of the rotor, the velocity vector V_{body} and advancing velocity vector V_{wheel} become parallel each other.
- (iv) At this time, the velocity component in the y axis becomes zero, and the body does not incline further.
- (v) The advancing direction is further varied. And both directions of the velocity vector V_{body} and the advancing velocity vector V_{wheel} intersect as shown in Fig. 8.
- (vi) Then the velocity component on the y axis turns to the wheel direction, i.e., the robot restores the posture upright.

Investigating the sequential motion changes (ii) \rightarrow (iv) \rightarrow (vi) in Fig. 8, the velocity vector of the body seen in the wheel-coordinates is merging with that of the wheel. The force causing above changes is the inertial force generated on the body by varying the advancing direction of the robot. According to such a motion sequence, the velocity vector of the robot approaches onto the wheel vector as shown in Fig. 7. In this way, the trajectories of both vectors curve to the opposite directions.

Based on the above experimental results, the stability principle in the roll direction can be explained as follows.

1. While the wheel velocity is small just after start moving, the robot restores the inclination in the roll direction by turning the advancing direction to the body's inclination using reaction torque of the rotor. Thus inclination of the robot to the roll direction is compensated by inclination in the pitch direction.
2. When the wheel velocity is increased, the robot can use the body's inertial force as well as varying the advancing direction in order to stabilize the posture in the roll direction.

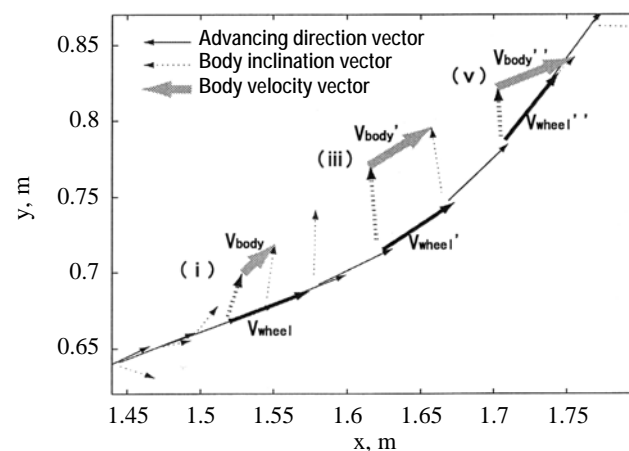


Figure 7 Vectors of advancing- and body inclination-direction on the ground.

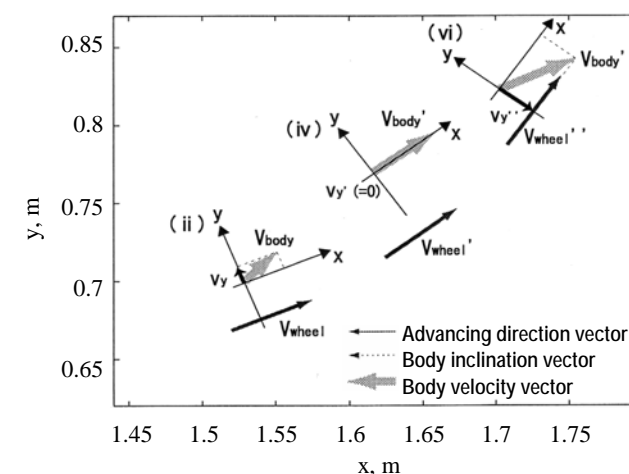


Figure 8 Velocity vectors on the ground.

3 CONTROL RULES BASED ON THE STABILITY

3.1 ACCELERATION CONTROL RULE

Sheng and Yamafuji [2], [3] stabilized the robot posture in the pitch direction by rotating the wheel. However, it is supposed by the results of [Section 3.2] that the advancing velocity of the robot might increase incessantly because the vehicle had to be accelerated to continue drive. In the real robotic unicycle, it cannot run long distance due to the torque limit of the motor. However their robot had no serious problem because the extension cables were only 8m long.

Here, we propose a control rule with which the robot is not continuously accelerated but driven with a constant velocity. According to the drive principle obtained in [Part 1], it is confirmed that the robot is accelerated or decelerated depending on whether the projection of CCG on the ground is located forward or backward of CP. Using this fact, we propose a control rule that the target pitch angle is adjusted depending on the wheel velocity.

Namely, the target pitch angle had to be diminished to decrease velocity, and augmented to increase it. And the specified target pitch angle must satisfy the following two conditions.

1. For the larger driving velocity, the smaller target pitch angle must be provided.
2. In order to realize smoother starting of the robot, the larger target pitch angle is given for a while after the starting.

Equation (1) is a function satisfying the above conditions.

$$\beta_{target} = -a\dot{\psi}^3 + b \quad (1)$$

where, β_{target} : target pitch angle, $\dot{\psi}$: angular velocity of the wheel, and a, b are constant coefficients, respectively.

As an example, a solid-line in Fig. 9 illustrates a curve given by Eq. (1) in which coefficients are chosen as $a = 1.0 \times 10^{-4}$ and $b = 0.05$. According to the graph, a larger target pitch angle can be taken while the wheel angular velocity is small just after the starting. Then a smaller target angle is provided when the wheel angular velocity is increased. In the real robotic unicycle, the larger target pitch angle is desirable since it must be accelerated until the posture is stabilized after the starting. Therefore, the control based on this function will be advantageous for the robot. If the target pitch angle is given by a dotted line in Fig. 9 as an example, it varies quickly just after the starting and inconvenient for a precise drive control of the robot.

3.2 2D SIMULATION RESULTS AND DISCUSSIONS

The proposed control rule is given by Equations (1) and (2).

$$U_{wheel} = k_{p1}(\beta_{target} - \beta) - k_{d1}\dot{\beta} \quad (2)$$

where, U_{wheel} : torque command to the wheel, β : pitch angle, β_{target} : target pitch angle, $\dot{\beta}$: pitch angular velocity, k_{p1} : proportional feedback gain (FBG), and: k_{d1} differential FBG.

Using the equations of motion and system parameters in [Section 3.1] together with the control rule proposed above, 2D simulation was carried out. Simulation results are shown in Figs. 10 and 11. Figure 10 (a) and (b) show time histories of the pitch angle and the pitch angular velocity. After the starting, the pitch angle varies largely

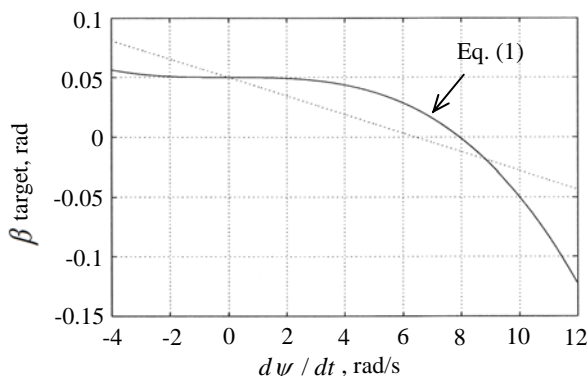
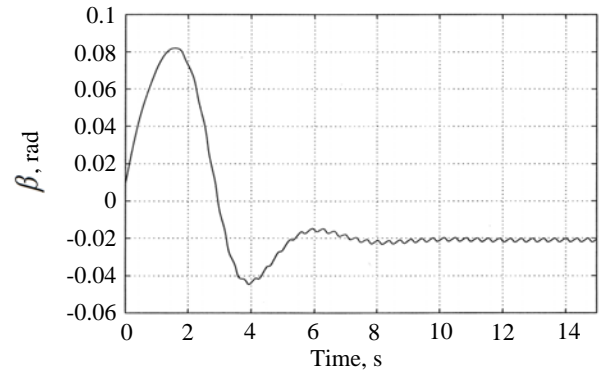
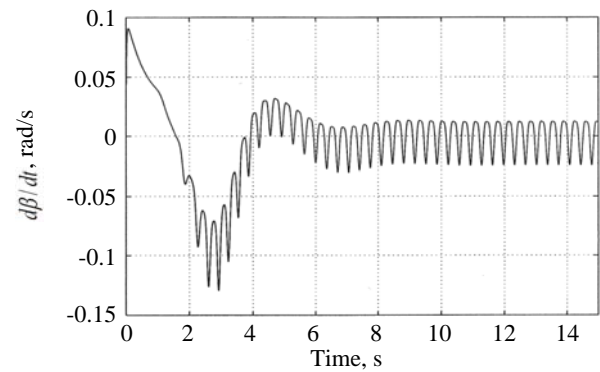


Figure 9 Relation between the target pitch angle and the wheel angular velocity.

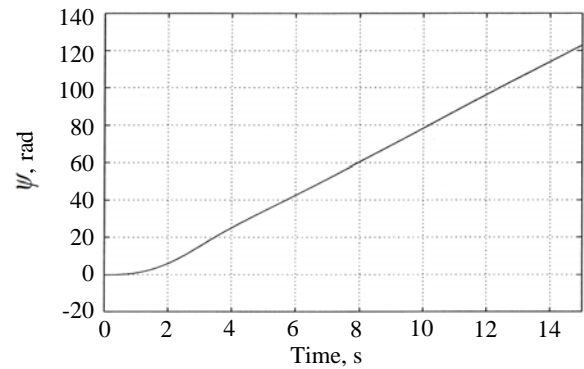


(a) The pitch angle

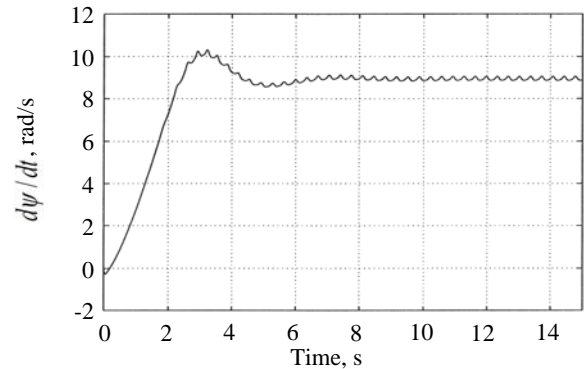


(b) The pitch angular velocity

Figure 10 Time history of the pitch angle and angular velocity, 2D simulation results.



(a) The wheel rotation angle



(b) The wheel angular velocity

Figure 11 Time history of the wheel angle and angular velocity, 2D simulation results.

during about 6 sec. Then, the robot is driven stably with roughly zero pitch angular velocity together with a constant pitch angle ($\beta = -0.02\text{rad}$). Time history of the wheel rotation angle in Fig. 11 (a) shows the smooth starting of the robot. Figure 11 (b) indicates that the driving with a constant angular velocity (ca. 9rad/sec) is attained about 7 sec after the starting. Summarizing the results, the robot succeeded in driven with the constant angular velocity (ca. 9rad/sec) at the constant pitch angle ($\beta = -0.02\text{rad}$). Since CCG of the robot overlaps with CP at $\beta = -0.02\text{rad}$ in this model, no acceleration is caused on the robot.

3.3 3D SIMULATION RESULTS AND DISCUSSIONS

The acceleration control rule applied to 3D simulation is constituted of Equations (1), (2) and (3).

$$U_{rotor} = k_{p2}(\dot{\gamma}_{target} - \dot{\gamma}) - k_{d2}\dot{\gamma} \quad (3)$$

where, U_{rotor} : torque command to the rotor, γ : roll angle, γ_{target} : target roll angle, $\dot{\gamma}$: roll angular velocity, k_{p2} : proportional FBG, and k_{d2} : differential FBG.

Utilizing the 3D model in [Part 1] and the acceleration control rule in Section 3.1 of this paper, 3D simulation was conducted. Simulation results are shown in Figs. 12 and 13. By time history of the wheel angular velocity given in Fig. 12, the stable driving with an almost constant angular velocity of 9rad/sec is attained. The stability in the roll direction is secured about 3sec after the starting as shown in Fig. 13.

4 DIRECTION CONTROL BASED ON THE DRIVE PRINCIPLES AND ITS APPLICATIONS

4.1 DETERMINATION OF THE DRIVE VELOCITY

As confirmed in Section 3.1, the robot is accelerated or decelerated depending on whether its CCG locates in front or rear of CP. Therefore, it is needed that CCG overlaps with CP in order to drive the robot with a constant velocity. In 2D simulation, the target pitch angle is given by Eq. (1) with $a = 1.0 \times 10^{-4}$ and $b = 0.05$. If the pitch angle of the robot driven at a constant velocity is known, we can determine the drive velocity by use of Eq. (1). For example, since CCG overlaps with CP in the 2D model when the target pitch angle is $\beta_{target} = -0.02\text{rad}$, the constant driving velocity $\dot{\psi}$ can be obtained by using Fig. 9. Namely, the abscissa of intersection with the horizontal line drawn from $\beta_{target} = -0.02$ on the ordinate and the curve given by Eq. (1) provides the constant wheel angular velocity $\dot{\psi}$. To increase the drive velocity, smaller a or larger b must be taken. On the other hand, larger a or smaller b is needed to decrease the velocity.

4.2 PROPOSAL OF THE DIRECTION CONTROL RULE

Without the direction control, the robot may advance to an unexpected direction. According to the stability principle

of the robot, the wheel rotation influences on the robot motion in the pitch direction, but few in the yaw direction. Since the rotor's rotation influences on the robot motion in the roll- and yaw-direction, its rotation is needed to control driving direction of the robot. Combining the acceleration control rules with a specified yaw angular velocity, a direction control rule is proposed, in which the target pitch angle β_{target} and yaw angular velocity $\dot{\alpha}_{target}$ must be specified.

Torque command to the wheel and rotor is given by Equations (1) and (2), and by Equations (4), (5) and (6), respectively.

$$U_{rotor} = U_{stabilize} + U_{direction} \quad (4)$$

$$U_{stabilize} = -k_{p3}\gamma - k_{d3}\dot{\gamma} \quad (5)$$

$$U_{direction} = k\dot{\psi}(\dot{\alpha}_{target} - \dot{\alpha}) \quad (6)$$

where, U_{rotor} : torque command to the rotor, $U_{stabilize}$: torque for stabilization, $U_{direction}$: torque for the direction control, $\dot{\alpha}$: yaw angular velocity, $\dot{\alpha}_{target}$: target yaw angular velocity, γ : roll angle, $\dot{\gamma}$: roll angular velocity, $\dot{\psi}$: wheel angular velocity, k_{p3} : proportional FBG, k_{d3} : differential FBG, and k : FBG.

Multiplier $\dot{\psi}$ in Eq. (6) is a kind of a feedback term which secures smooth and stable starting of the robot.

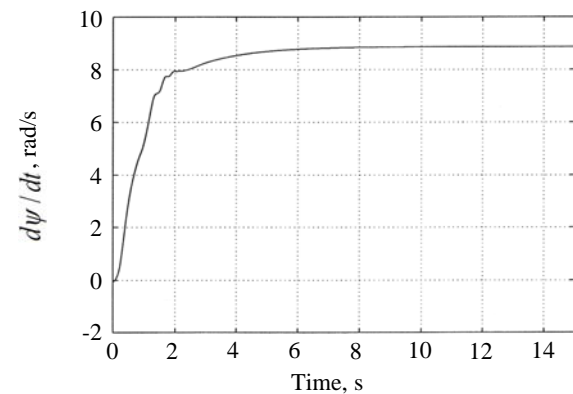


Figure 12 Time history of the wheel angular velocity, 3D simulation result.

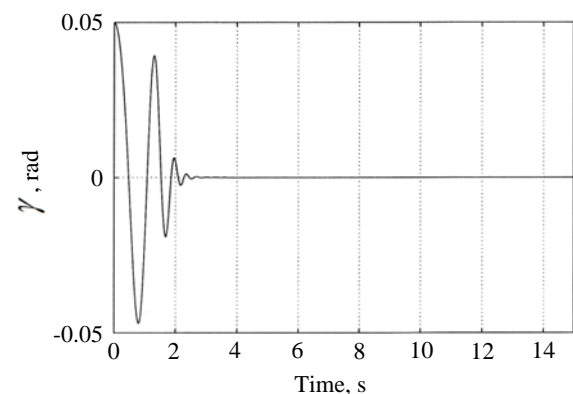


Figure 13 Time history of the roll angle, 3D simulation result.

4.3 EXAMPLE OF THE DIRECTION CONTROL A

A 3D simulation for tracing a circle was carried out using Equations (1), (2), (4), (5) and (6). The results are shown in Figs. 14 and 15. Figure 14 indicates the trajectory of a traced path. The yaw- and rotor-angular velocity shown in Figs. 15 (a) and (b) are kept roughly constant after ca. 4sec of the starting. The simulation results show that the satisfactory direction control is attained and a circle is traced. Although an experiment on tracing a circle by the real robot was attempted, it was not successful due to the motor encoder equipped on the pedal. The reason why is that the top of the encoder projected outward as seen in [Fig. 1] of [Part 1] touches and rubs the ground while the robot inclines toward the inside of the circle.

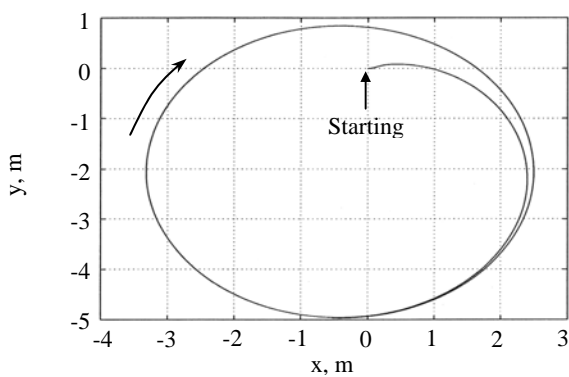
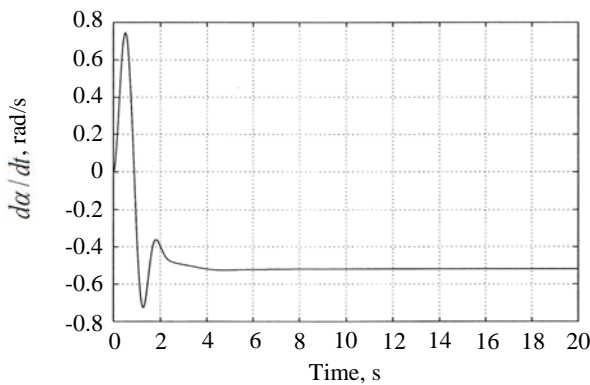
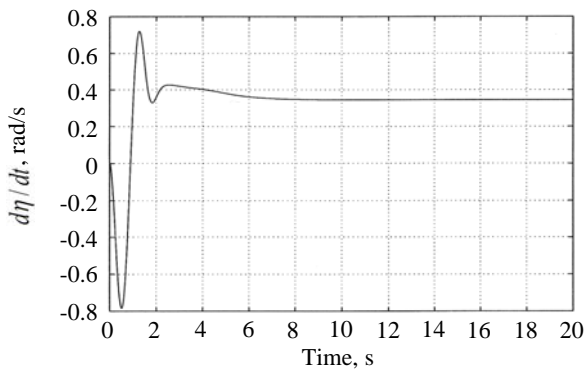


Figure 14 Trajectory of the traced circle.



(a) The yaw angular velocity



(b) The rotor angular velocity

Figure 15 Time history of the yaw- and rotor-angular velocity, tracing a circle.

4.4 EXAMPLE OF THE DIRECTION CONTROL B

In the preceding section, the direction control of the robot was attained by specifying a target yaw angular velocity. Next, driving control rules for tracing “8” character are proposed. In order to trace “8” character by the robot, the direction (yaw angular velocity) must be varied to switch one circle to another.

The proposed direction control rules are given below. Torque command to the wheel is provided by Equations (1) and (2). And torque command to the rotor is given by Equations (4), (5) and (7).

$$U_{direction} = k\dot{\psi} \left[\dot{\alpha}_1 - \frac{\dot{\alpha}_2}{2} \left\{ 1 - \cos \left(\pi \frac{t - t_{begin}}{t_{req}} \right) \right\} - \dot{\alpha} \right] \quad (7)$$

where, $\dot{\alpha}$: yaw angular velocity, $\dot{\alpha}_1$: target yaw angular velocity to trace the first circle, $\dot{\alpha}_2$: target yaw angular velocity to trace the second circle, $\dot{\psi}$: wheel angular velocity, k : FBG, t : drive time, t_{begin} : time to trace the second circle, and t_{req} : time required from initiation of yaw angular velocity change to end.

The term $\dot{\alpha}_1 - \frac{\dot{\alpha}_2}{2} \left\{ 1 - \cos \left(\pi \frac{t - t_{begin}}{t_{req}} \right) \right\}$ in Eq. (7) is the

target roll angular velocity $\dot{\alpha}_{target}$. By varying $\dot{\alpha}_{target}$ with time, the advancing direction of the robot can be arbitrarily varied.

The results of 3D simulation are shown in Figs. 16 and 17, which illustrate the traced “8” character and time history of the yaw angular velocity, respectively.

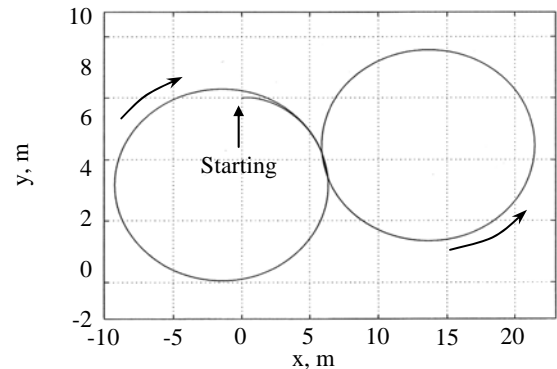


Figure 16 Trajectory of the traced “8” character.

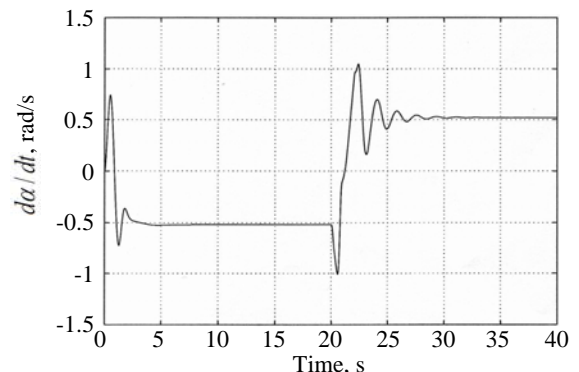


Figure 17 Time history of the yaw angular velocity.

5 CONCLUSIONS

Conclusions of this study including [Part 1] are summarized.

1. The stability principle of the robotic unicycle in the pitch direction can be explained as follows. When the robot body inclines forward or backward, the wheel rotates to go forth or back till restoring the balance. When it inclines forward more than a specified pitch angle, the wheel rotates to cancel the difference. Then the robot is accelerated until it restores the stable posture.
2. The drive principle can be explained as follows. The robot is accelerated or decelerated depending on whether projection of CCG on the ground is located in front or rear of CP. Thus, the robot runs with a constant velocity by specifying the pitch angle so as to let CCG overlap with CP.
3. When the robot inclines in the roll direction, the inclination in the roll direction is compensated by that in the pitch direction. Reaction torque of the overhead rotor rotates quickly the robot to the inclined direction.
4. The changes of the pitch-, roll- and yaw-angle are closely related each other. The necessary rotation angle of the robot to compensate the inclination in the roll direction is obtained by the relation between them in [Part 1].
5. Acceleration control rule that a target pitch angle is adjusted depending on the wheel velocity is proposed. Its effectiveness is verified by experiment as well as simulation.
6. Combining the acceleration control rule and specification of the yaw angular velocity, a direction control rule is proposed. Then computer simulation to trace a circle and "8" character by the robot was conducted. The results are satisfactory. In this way, the validity of the proposed direction control rule is verified. It can be applied to drive an inverted pendulum type robot along a given path with a constant arbitrary velocity.
7. The role of the overhead rotor is not simple but causes the change of the yaw-, roll- and pitch-angle through rotation of the robot body. It performs motions dynamically similar to human's twisting a torso, extending or closing hands and squeezing shoulders in human riding a unicycle.
8. The effect of gyro-moment and centrifugal force was examined. They are negligible in comparison with that of reaction torque exerted by the rotor's rotation and inertial force due to driving of the robot.
9. The closed link mechanisms have been supposed indispensable for the human riding type unicycle. However, the pedaling action is not necessary to the postural stability of the robot in the pitch direction.

REFERENCES

- [1] H. Suzuki, S. Moromugi and K. Yamafuji, "Motion Principles and Control of a Human Riding Type Robotic Unicycle (Part 1, Mechanisms, Stability Principles and Simulation)", *International Journal of Mechanics and Control*, Vol.12, No. 2, pp. 3-12, 2011.
- [2] Z. Q. Sheng and K. Yamafuji, "Study on the Stability and Motion Control of a Unicycle (Part 3: Characteristics of a unicycle)", *Japan Society of Mechanical Engineers (JSME) Intern. Journal*, Series 3, 39-3, pp. 560-568, 1996.
- [3] Z. Q. Sheng and K. Yamafuji, "Postural Stability of a Human Riding a Unicycle and Its Emulation by a Robot", *IEEE Transactions on Robotics and Automation*, 13-5, pp. 709-720, 1997.
- [4] T. Hirabayashi and K. Yamafuji, "Posture and Driving Control of a Variable Structure Type Parallel Bicycle (1st Report, Posture Stabilization and Drive Control of the Arm-Wheel Model)" (in Japanese), *Trans. on JSME*, 56-523C, pp. 721-730, 1990.
- [5] Z. Q. Sheng and K. Yamafuji, "Study on the Stability and Motion Control of a Unicycle (Part 2, Design and Experimental Results of a Unicycle Robot)" (in Japanese), *ibid.*, 61-583C, pp. 1042-1049, 1995.

3D MODELS FOR LANGHE HAZELNUTS

Stefano Tornincasa Elvio Bonisoli Marco Brino

Politecnico di Torino - Dipartimento di Sistemi di Produzione
Corso Duca degli Abruzzi, 24 - 10129 Torino – ITALY

ABSTRACT

The hazelnut production for food-farming field industry is made up of several processes and some of those could be suitable for performing virtual simulations. An aim for using simulations is to check the strong and weak features of the machineries and then apply suitable modifications. Both machineries and hazelnuts 3D models are then requested but, while machinery model is unique or the technical solution is represented through a deterministic sketch, hazelnut model must represent as good as possible its real statistical distribution of its characteristics. Then a parametric model of the hazelnut is useful for being a reference model whose parameters can be edited to generate a defined number of hazelnuts consistent with real distributions.

Keywords: hazelnut, 3D parametric model, stochastic simulation

1 INTRODUCTION

Virtual simulation of production processes is being widely used in the mechanical field, the implementation of these techniques in food-farming processes could be a useful step to improve machineries performance in that field, as well.

Taking into account typical food products of the south part of Piedmont in Italy, the Langhe region, an interesting object in the production steps, that could be virtually modelled, are the geometrical separation in different dimension families (*size*) and the removal of object different from the hazelnuts that were accidentally catch by the harvesting process. A sketch of separation and hulling processes is summarised in [1] for Turkish fruits.

Virtual 3D models of hazelnuts are needed to be imported into the model of the machinery, then to return reliable results from simulations, the geometrical and the inertial characteristics of hazelnuts fruits must be consistent with their real statistical distributions. This consideration causes the need of a parametric model of hazelnut, which allows having just one basic model whose parameters can be edited and updated, to generate then nuts with specific features. This kind of method was already used in wide-ranging applications, such as biomedical reverse engineering [2] or for the modelling of trees [3].

2 DEFINITION OF THE PARAMETERS

To choose which geometrical parameters can be taken as reference to define and reproduce a specific hazelnut, a representative sample of hazelnuts is considered to carry out this step.

2.1 NOMINAL SIZE

In the food-farming field, any type of food (such as hazelnuts, walnuts, eggs, ...) has a main feature that defines its dimensional range: this is called "size".

In hazelnuts manufacturing companies, the size is chosen by the result of the sieving process: a vibrating perforated deck processes both in-shell and in-kernel, where the square-holes have a certain size. In this way, for example, a hazelnut of size 16 mm is a hazelnut that passes through a sieve of size 17 mm, but does not pass through a sieve of size 16 mm.

For better representing the natural distribution of sizes in nature, a number of 134 hazelnuts have been taken as a sample (Figure 1), with the statistical distribution shown in Figure 2. This distribution was provided by an hazelnuts supplier based on its experience, and the amount of 134 samples is an extension of a previous group of 120 samples, already used by the authors in [4] which had uniform distribution.

In-shell hazelnut sizes have a minimum value of 15 mm, because smaller hazelnuts are more likely not fully grown, and a maximum size of 20 mm, where also hazelnuts of size over 20 mm are included.

Contact author: S. Tornincasa¹, E. Bonisoli², M. Brino³

¹stefano.tornincasa@polito.it

²elvio.bonisoli@polito.it

³marco.brino@polito.it



Figure 1 - Hazelnuts of different size

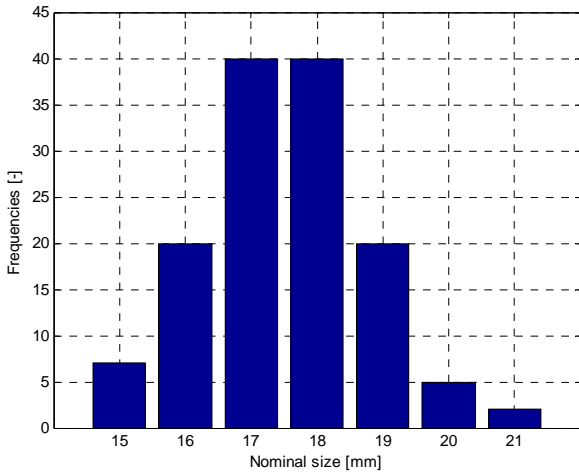


Figure 2 - Statistical distribution of the nominal size

The number of hazelnuts considered for each size are summarised in Table I.

Table I - Number of specimens for each size

Size [mm]	15	16	17	18	19	20	>20
Elements [#]	7	20	40	40	20	5	2

2.2 REFERENCE FRAME AND GEOMETRICAL MEASUREMENTS

A reference frame is defined to identify the dimensions in three spatial directions. The first value, called *A*, is the dimension of the hazelnut that starts from the base and ends to the head of the hazelnut. Then the other two dimensions belong to a plane normal with respect to the dimension *A*, and where the profile on that plane has its maximum extension. The bigger dimension in that plane is defined as *B*, and then the dimension orthogonal to dimension *B* is defined as *C*. The dimensions details are clarified in Figure 3.

Once this reference frame is defined, the *A*, *B* and *C* values of all the 134 hazelnuts of the sample can be measured and collected.

These measurements are used to characterize the sample and to perform statistical considerations on the values distribution.

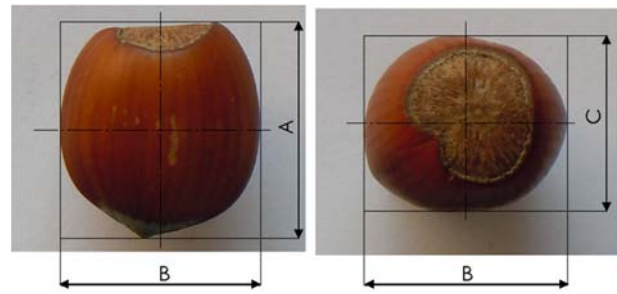


Figure 3 - Definition of dimensions *A*, *B* and *C*

2.3 “MEASURED” SIZE

A quick overview on the measured data reveals that some hazelnuts seem to be out of their nominal size range. This result occurs because sieving process is not ideal and some hazelnuts do not have enough possibility to fit its right hole. Then another feature must be considered to be consistent with the aim of having a value that identify the general “size” of the hazelnuts. By analysing the sieving process, in an ideal situation where the hazelnut finds its hole in an infinite amount of time, it would pass through the sieve on the second of the dimensions *A*, *B* and *C* placed in ascending order. An example of this behaviour is represented in Figure 4 and Figure 5 with 3D models. This intermediate value can be then referred to as “measured” size, where the value can be considered with the measured precision of 0.01 mm.

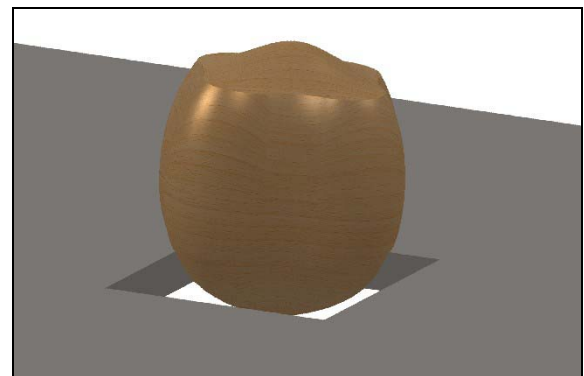


Figure 4 - Hazelnut passing through hole along direction *A*

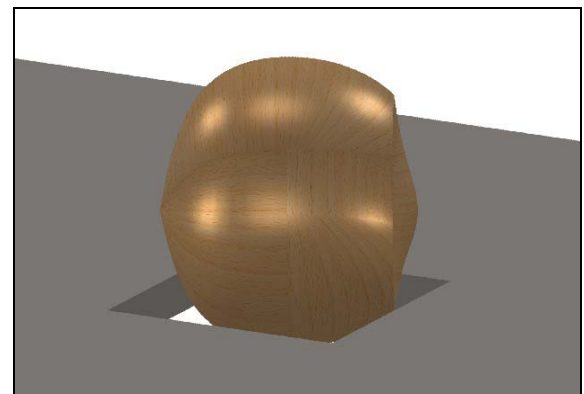


Figure 5 - Hazelnut passing through hole along direction *B*

2.4 A/B AND C/B RATIOS

A useful strategy to find relations among A , B and C could be the case of considering one of them as a reference, and the other two as their ratios with respect to the reference. In this case, B is considered as the reference and then the relevant ratios are A/B and C/B . By plotting these ratios with respect to the reference, a general look on the possible dependencies can be considered.

In particular, as shown in Figure 6, A/B with respect to B seems to have a certain inverse relation: the bigger is B , the less A/B is detected.

This relationship means that biggest hazelnuts have an almost spherical shape, while smallest ones have a stretched shape.

By plotting C/B with respect to B , no significant relationship looks to be present. This can be checked on Figure 7.

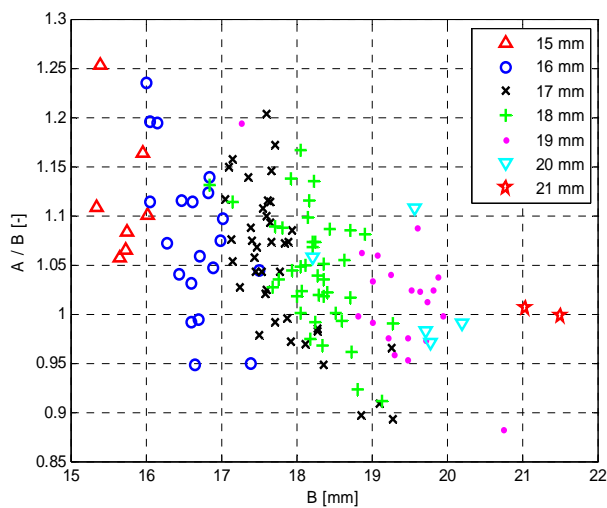


Figure 6 - Dependency of parameter A/B with respect to B

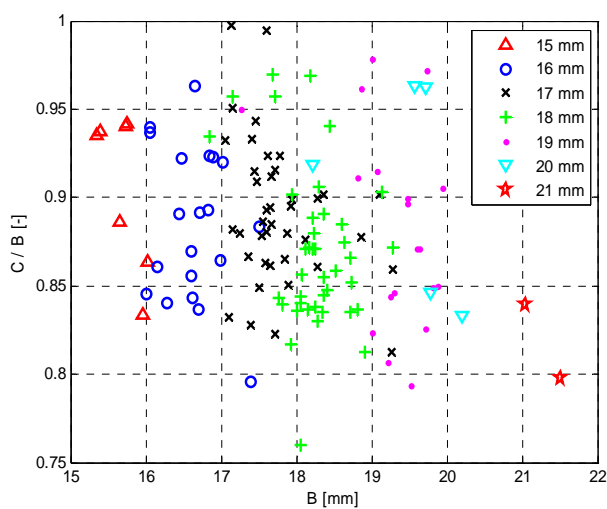


Figure 7 - Dependency of parameter C/B with respect to B

2.5 NUMBER OF LOBES

Not all the hazelnuts have the same shape in the BC plane, but the “number of lobes” can classify their shape.

The analysed samples have two, three and four lobes, describing the classification of *two-lobate*, *three-lobate* and *four-lobate* hazelnuts. These features are shown in Figure 8, Figure 9 and Figure 10 for the considered families.

There are some cases where this classification is not immediate, and some hazelnut, such as the ones represented in Figure 11, could be classified with just one lobe. As described further, these cases do not affect the previous classification for what is related to the three-dimensional modelling.



Figure 8 - Examples of hazelnuts with two lobes



Figure 9 - Examples of hazelnuts with three lobes

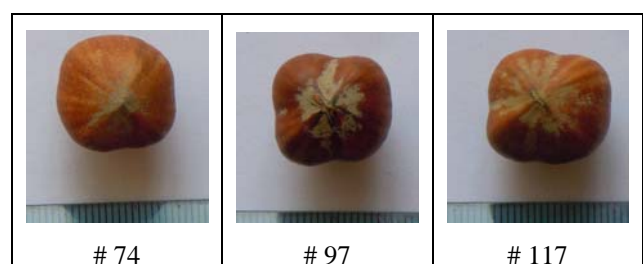


Figure 10 - Examples of hazelnuts with four lobes



Figure 11 - Examples of hazelnuts with unclear number of lobes

3. PARAMETRIC 3D MODELS OF HAZELNUTS

Once the relevant parameters are identified and defined, they can be used as the starting point for the development of the parametric 3D CAD model of the hazelnuts.

This modelling follows some logical steps that are platform independent, and this means that can be followed with any parametric CAD software, each one using their specific feature. In this paper, the software used is Solidworks, therefore the features mentioned are related to this software.

Three different files are necessary to model separately the hazelnuts with different number of lobes. The only difference is the first starting sketch from which the first feature is created, and then all the logical steps are repeated.

The logical steps are summarised below:

- **generation of the body:** the body is modelled with a number of spheres that represents the lobes, and in this step the parameters B and C define the dimensions;
- **stretching of the body:** the height of the body must be adapted with respect to the dimension A ;
- **generation of the top:** modification of the upper part of the body to model the top of the hazelnut;
- **generation of the bottom:** modification of the lower-half part of the body to reproduce the bottom part of the hazelnut.

All the dimensions in the sketch or related to the features are constant or dependant by the parameters B , A/B and C/B .

3.1 GENERATION OF THE BODY

A number of partially intersecting circles, equal to the number of lobes to represent, composes the first sketch necessary to generate the body. These circles are arranged in a circular pattern and in such a disposition that the total horizontal and vertical overall dimensions match the dimensions B and C respectively. The circles are the base entities to then generate the spheres.

The sketches are represented in Figure 12 for the three considered cases.

As mentioned above, the feature is identical for all the different number of lobes, the only difference is the number of circles in the relevant sketch.

The feature used is “Revolved Boss/Base”, performing a revolution of all the lobes one-by-one. In Figure 13 it is shown the result of the operation.

The shape of the interpenetration regions among the spheres must be smoothed in order to have a more natural representation. For this reason, rounds and fillets are added in the interpenetration regions; the final result of this operation is shown in Figure 14.

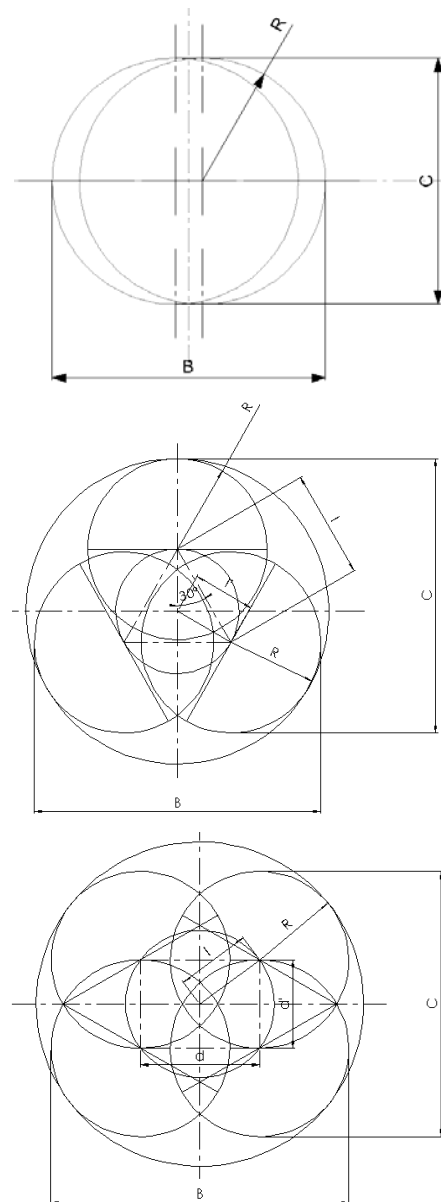


Figure 12 - Sketches for two, three and four-lobes hazelnuts



Figure 13 - Result of the body generation step

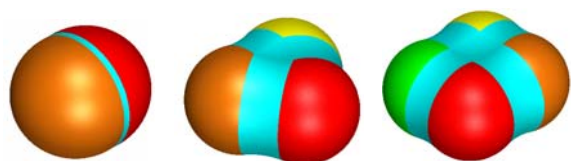


Figure 14 - Body with rounds and fillets

3.2 STRETCHING OF THE BODY

While the arrangement of the circles in the first sketch determines the overall dimensions B and C , without any modifications the dimension A would be the diameter of the spheres. For this reason, a stretching of the spheres in direction A is necessary for having an overall dimension that matches with A . The result of this step is represented in Figure 15.

In Solidworks this operation is collected in the “Flex” feature and it is called “Stretching”.

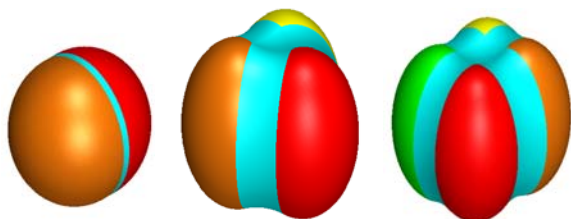


Figure 15 - Result of the body stretching operation

While the current model is dimensionally consistent with the parameters, the shape is not so aligned to a hazelnut shape, therefore little modifications must be taken into account to better match real shape and volume.

3.3 GENERATION OF THE TOP

To model the top of the hazelnut, the body must be cut at a certain height, which is a percentage of the total height. After this horizontal cut, another feature is used to fill the gap and match the dimension A , with a more representative shape. The result of this step is illustrated in Figure 16.

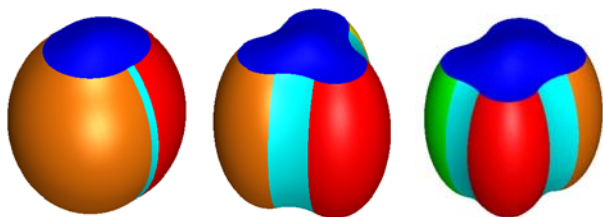


Figure 16 - Result of the top generation step

The Solidworks feature which best fits the shape is “Dome”.

3.4 GENERATION OF THE BOTTOM

For the same reason of the section above, also the bottom of the hazelnut must be modified to match the real shape. The shape at this step is quite good except for the fact that the geometry can be thought as a surface, which starts with a certain profile and converges to a point.

The operations are then to cut horizontally at a height that still matches the real shape and then to apply a feature which starting from the surface generate by the cutting

operation converges to a point at a total height of dimension A . The result of this operation, and then of the final step, is shown in Figure 17.

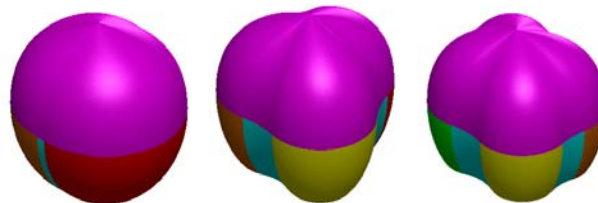


Figure 17 - Result of the bottom generation step (final result)

This operation was invented for modelling turbine blades: where many profiles are connected to each other by using tangent surfaces.

This feature in Solidworks is called “Lofted Boss/Base” and being so important for the application mentioned above, most CAD software have their equivalent feature.

4. MODEL VALIDATION

Once the 3D model with its relevant parameters is completed and is working correctly, a verification of the approximation of the parametric model with respect to real hazelnuts can be carried out.

For this purpose, a sub-sample of 32 hazelnuts is randomly selected from the starting sample of 134 hazelnuts and their measured values of B , A/B , C/B are used as input for the parametric model. By means of this approach a specific real hazelnut can be compared with its 3D representation.

4.1 COMPARISON VIA VIEWS AND SECTIONS

A quick and useful tool to check the differences between the real sample and the parametric model is to superimpose the projected views of the 3D model and the respective picture of the real hazelnut acquired with digital camera.

Then, by proportionally stretching the pictures to match dimensions A , B and C of the model, both a qualitative and quantitative comparison between the shapes can be performed and the model can be criticised. In Solidworks this operation of comparison can be performed by importing the pictures of the real hazelnut taken from top view, front view and right view on the respective reference planes of the model, as shown in Figure 18.

The analyses on the shape are performed on a Solidworks drawing with superimposition of a section of the model and its respective picture. The result allows to estimate shape differences by the visual identification of the maximum and the minimum distance for each view and to evaluate the difference in a direction which connects the location of the maximum or minimum distance with the centre (model origin) of the parametric model. In Figure 19 and Figure 20 the shape analysis on hazelnuts with two and three lobes are respectively represented.



Figure 18 - 3D representation of the parametric hazelnut with pictures of the respective real hazelnut on the reference planes

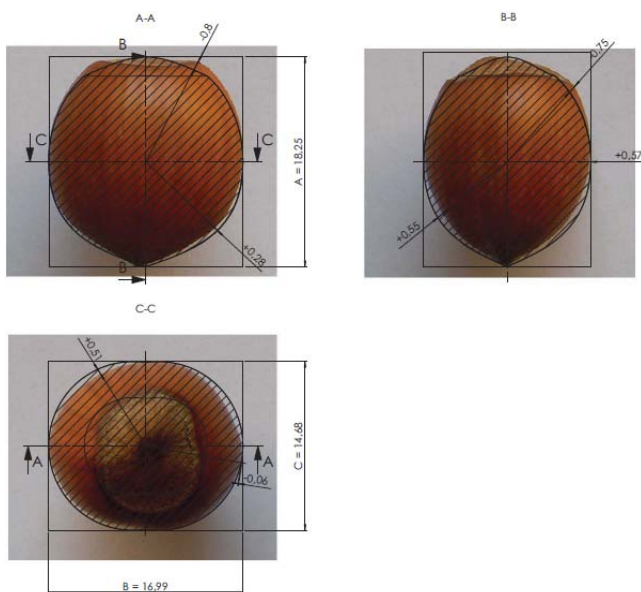


Figure 19 - Model validation of two-lobate hazelnut

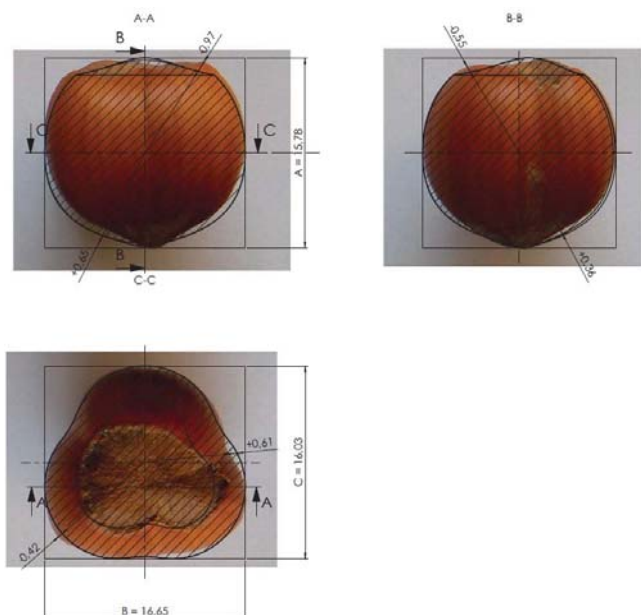


Figure 20 - Model validation of three-lobate hazelnut

All the analyses are performed separately by the number of lobes of the hazelnuts. In Table 2, Table 3 and Table 4 the difference in percentage of the parametric model are summarised. The terms m_{min} and m_{max} are the minimum and maximum average values of the positive and negative differences between real and parametric shapes, while max and min are the absolute maximum and minimum differences measured.

Table 2 - Error percentage of hazelnuts with two lobes

TWO LOBES					
SECTION A-A		SECTION B-B		SECTION C-C	
<i>min</i>	-7.17 %	<i>min</i>	-6.83 %	<i>min</i>	-3.35 %
<i>max</i>	+7.78 %	<i>max</i>	+6.25 %	<i>max</i>	+4.34 %
m_{min}	-4.70 %	m_{min}	-4.07 %	m_{min}	-1.30 %
m_{max}	+2.72 %	m_{max}	+3.72 %	m_{max}	+3.31 %

Table 3 - Error percentage of hazelnuts with three lobes

THREE LOBES					
SECTION A-A		SECTION B-B		SECTION C-C	
<i>min</i>	-8.46 %	<i>min</i>	-7.01 %	<i>min</i>	-8.96 %
<i>max</i>	+7.25 %	<i>max</i>	+5.53 %	<i>max</i>	+6.36 %
m_{min}	-4.57 %	m_{min}	-3.83 %	m_{min}	-4.78 %
m_{max}	+3.84 %	m_{max}	+2.78 %	m_{max}	+4.12 %

Table 4 - Error percentage of hazelnuts with four lobes

FOUR LOBES					
SECTION A-A		SECTION B-B		SECTION C-C	
<i>min</i>	-4.39 %	<i>min</i>	-3.85 %	<i>min</i>	-2.03 %
<i>max</i>	+6.43 %	<i>max</i>	+4.46 %	<i>max</i>	+5.96 %
m_{min}	-3.50 %	m_{min}	-3.56 %	m_{min}	-1.78 %
m_{max}	+4.15 %	m_{max}	+3.15 %	m_{max}	+5.40 %

These tables show that the absolute minimum is less than 9% while all the mean values remain under 5 % with only one exception (5.40 %).

These values are quite acceptable for a first attempt with the definition of four parameters.

4.2 COMPARISON VIA REVERSE ENGINEERING

A more accurate tool to quantify the differences between parametric model and real hazelnuts is the possibility to import in the Solidworks 3D environment the acquisition of the external surface of real samples. This procedure is known as Reverse Engineering (RE), and there are many methods for the acquisition of the surface of a 3D body.

The implemented method is a compromise between cost and acquisition accuracy, with the drawback of a very long acquisition time. This limit caused the possibility to choose only five samples for the acquisition.

In Figure 21 the 3D representation of the body obtained through RE is shown.

With this method, also a comparison between the volumes of the two respective models can be performed taking into account that, even if the volume values are very close, their shapes can be quite different.

A qualitative matching can be verified by following the same comparison with views and sections described in the previous section, with an example shown in Figure 22.

The volume and surface differences can be obtained directly from Solidworks with an appropriate command. Finally, the mean percentage errors can be calculated and summarised in Table 5.

Table 5 - Error percentages between parametric model and hazelnut RE on volume and surface

VOLUME ERRORS			SURFACE ERRORS		
<i>min</i>	<i>mean</i>	<i>max</i>	<i>min</i>	<i>mean</i>	<i>max</i>
0.67 %	4.46 %	9.12 %	1.94 %	3.77 %	5.38 %

Also in this case the error percentages are quite low and the means are below 5 %. The proposed model demonstrates to be acceptable regarding both dimensions and shape.



Figure 21 - 3D representation of the result of RE process

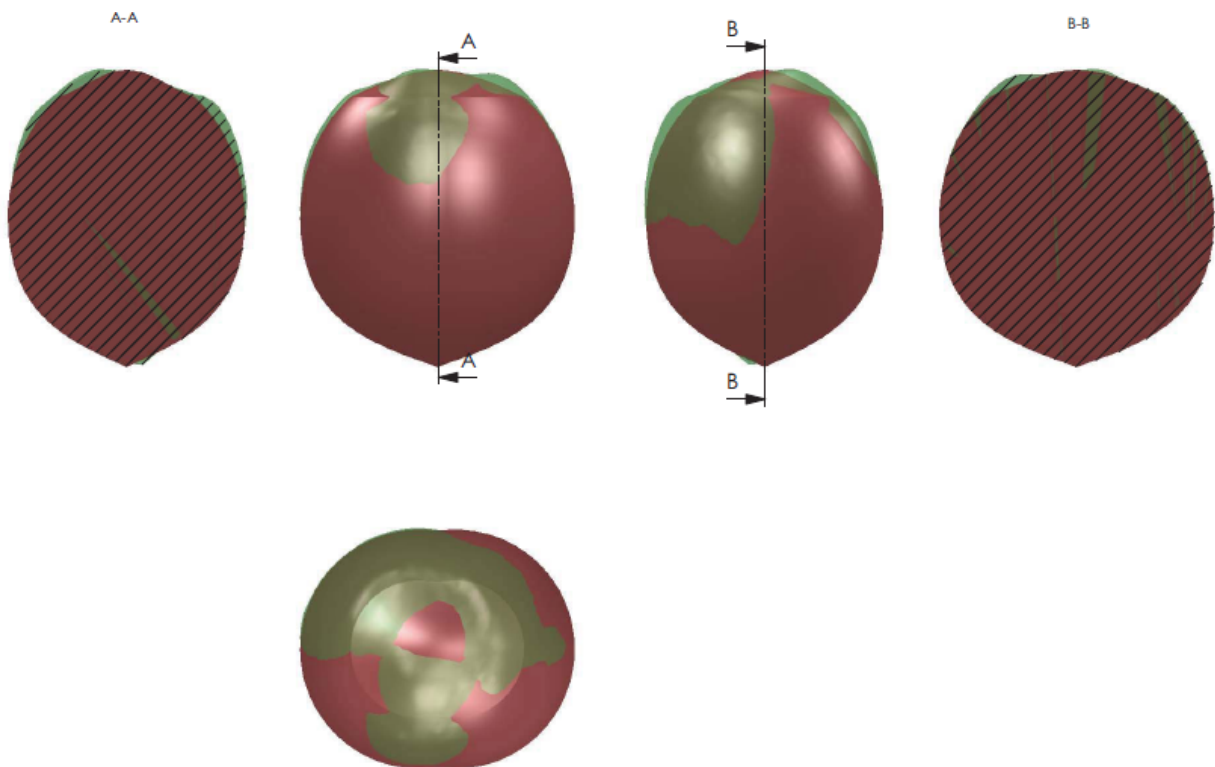


Figure 22 - Drawing representation of the superimposition between parametric model (in red) and hazelnut RE surface (in green)

5. CONCLUSIONS AND FUTURE DEVELOPMENTS

By means of the parametric model proposed and described in this paper, any hazelnut of the considered specimens can be reproduce with an average shape difference of about 5

%. It is also possible to generate an hazelnut with different values of the parameters such as considering other samples. This model can be used in the virtual simulation of the production processes by importing it into the model of the machinery to be evaluated.

Through the analyses on the statistical distributions of the parameters, an automated algorithm can be developed in order to generate a certain number of hazelnuts with the real distributions of their parameters and to have enough number of samples to be introduced in the virtual simulation model.

Further developments foresee the expansion of the parametric model regarding the hazelnut kernel, with the conversion of the model subject of this paper to represent the shell. An appropriate number of additional parameters should be introduced to represent the shell thickness. This following step requests the shelling of the 134 hazelnuts of the sample and then the statistical analysis on the distribution of the kernel parameters. The final aim for an optimal virtual and parameterised model of hazelnut is the estimation of density and elastic properties of shell and kernel.

REFERENCES

- [1] Özdemir M. and Özilgen M., Comparison of the quality of hazelnuts unshelled with different sizing and cracking systems. *Journal of Agricultural Engineering Research*, Vol. 67, No.3, pp. 219-227, 1997.
- [2] Zhang T., Guo L., Li G., Nie J. and Liu T., Parametric representation of cortical surface folding based on polynomials. *MICCAI 2009*, Part II, LNCS 5762, pp. 184-191, 2009.
- [3] Chen X., Neubert B., Xu Y., Deussen O. and Kang S., Sketch-based tree modeling using Markov random field. *ACM Transactions on Graphics*, Vol. 27, No. 5, pp. 109:1-109:9, 2008.
- [4] Bonisoli E. and Brino M., Modelli virtuali 3D per le nocciole delle Langhe. *Il Progettista Industriale*, XXXI(8), ISSN: 0392-4823, pp. 35-38, 2011.

AN EXPERIMENTAL CHARACTERIZATION OF A RICKSHAW PROTOTYPE

Tao Li*

Marco Ceccarelli*

*LARM Laboratory of Robotics and Mechatronics, DiMSAT – University of Cassino
Via Di Biasio, 43 – 03043 Cassino (Fr), Italy – E-mail: {taoli, ceccarelli}@unicas.it

ABSTRACT

In this paper, a rickshaw robot has been characterized from aspects of mechanical design and experimental tests. Experiments have been done to measure contact forces between feet and terrain, acceleration of the robot body and torque of the motor during a walking process. Experimental results of walking operation of a built prototype are reported to show characteristic features of a rickshaw efficient performance.

Keywords: Mobile robots, Legged robots, Experimental characterization, Robotics.

1 INTRODUCTION

Mobile robots can be classified by the device they use to move, mainly as legged robots (human-like legs or animal-like legs), wheeled robots, and track robots. Normally, wheeled robots have better stability and higher efficiency than legged robots, but they are not suitable in moving in an uneven environment. On the other hand, legged robots are more suitable in an unstructured environment than wheeled robots.

Hybrid systems have been developed as combination of wheeled and legged solutions with aim to exploit the advantages of both types of mobile systems.

A leg-wheel hybrid stair climbing wheelchair has been proposed in [1]. This robot consists of eight independent prismatic-joint legs and eight wheels. Rickshaw robot is another kind of leg-wheel hybrid robot, which has been studied by several researchers [2]. The word rickshaw came from China where they were mainly used as means of transportation for the social elite [2] as shown in Fig. 1. Rickshaw traditionally refers to a mode of human-powered transport: a person pulls a two-wheeled car with seats for one or two persons. Basically a rickshaw is a simple two-wheel chariot that is usually used for ground transportation by pulling and pushing it both for motion and for horizontal positioning.

A Chinese farmer inventor Wu Yulu has created several human-sized rickshaw robots which can transport him while speaking in a loudspeaker and playing music. The latest version of his rickshaw robot can move forward and backward, and change directions while walking under the control of a passenger through a steering wheel [3].



Figure 1 A Chinese rickshaw
(Photo is taken from web page).

At LARM: Laboratory of Robotics and Mechatronics in Cassino, design and research activities have been carried out to the design of legged walking machines [4]-[5], and even specifically for rickshaw robots. A rickshaw walking robot has been presented by Ceccarelli et al in [6], in which a study of feasibility had been carried out and preliminary results were presented on mechanical characteristics and operation programming. A hybrid walking robot has been proposed in [7] with two legs with one DOF (degree of freedom) and two passive wheels and it is capable of a straight walking. Then a low-cost easy-operation biped

Contact author: Tao Li¹, Marco Ceccarelli²

¹taoli@unicas.it

²ceccarelli@unicas.it.

mechanism has been proposed for a prototype of rickshaw robot [8]. Basic features of this system are compactness, light weight, and reduced number of DOFs. It is capable of carrying loads and straight walking with only one actuator. Furthermore, the additional passive wheeled system can increase the stability and adaptability of the robot over several types of terrains. A prototype has been built at LARM in Cassino (see LARM web page and Fig. 7).

In this paper, the LARM rickshaw solution has been analyzed in detail through the following aspects: mechanical design and kinematic modelling of the identical legs in section II; an experimental layout in section III; and in section IV experiment results are reported to characterize the contact forces between feet and terrain, the acceleration of the body, and also the torque of the motor during a walking operation. Experimental results show that the proposed LARM rickshaw solution has four main features during walking, namely, the operation of this rickshaw robot is very easy; contact forces between feet and terrain show that there is no wallop gait; acceleration shows that the rickshaw robot has a smooth movement; and measured actuation torque shows that it does not require high power in operation.

2 THE RICKSHAW SOLUTION

One basic consideration for a robotic leg design is that the leg should generate an approximately straight-line trajectory for the foot with respect to the body [9, 10]. A Chebyshev mechanism is used in LARM leg in the design of the biped mechanism with a pantograph mechanism. The pantograph is used to amplify the trajectory generated by the Chebyshev mechanism and to have a human-like operation. Besides the biped mechanism, the rickshaw robot has also been provided with a passive wheeled system to increase its load capability and stability of walking on different types of terrains.

Namely, the LARM rickshaw robot consists of a biped robot with one DOF and a chariot [4, 8]. It gives high maneuverability, simple use, reduced size, and it does not require high power in operation. A mechanical design of the rickshaw robot is shown in Fig. 2 with its outside dimensions. The biped mechanism is a low-cost one DOF mechanism and it is actuated by a DC motor, which is installed on board. A T shape gear box is used to transmit the motion to two legs simultaneously. The lengths of links have been determined by considering that the shape of the end leg point trajectory should be similar to the shape of human's foot trajectory [4].

A sketch for the rickshaw leg design is shown in Fig. 3. The solution considers a fully rotative actuation at point L that gives a suitable trajectory of point B, which can be suitably modified by changing the design parameters shown in Fig. 3. In particular, it has been shown that good features for leg operation can be obtained if the transmission angles γ_1 and γ_2 have suitable values. A parametric study had been carried out to study the influence of design parameters on

motion capabilities of the one-DOF leg mechanism in rickshaw solution [8].

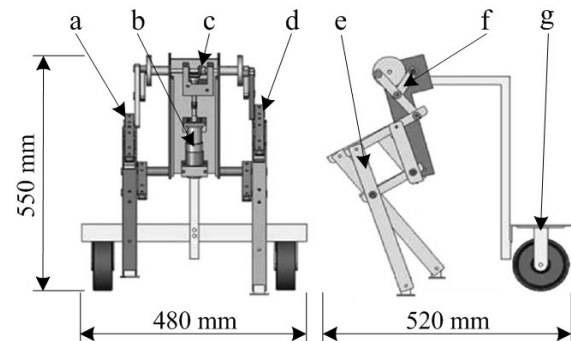


Figure 2 Mechanical design of LARM rickshaw robot with its main dimensions (a- right leg; b- motor; c- T gear box; d- left leg; e- pantograph mechanism; f- Chebyshev mechanism; g- passive two-wheeled chariot).

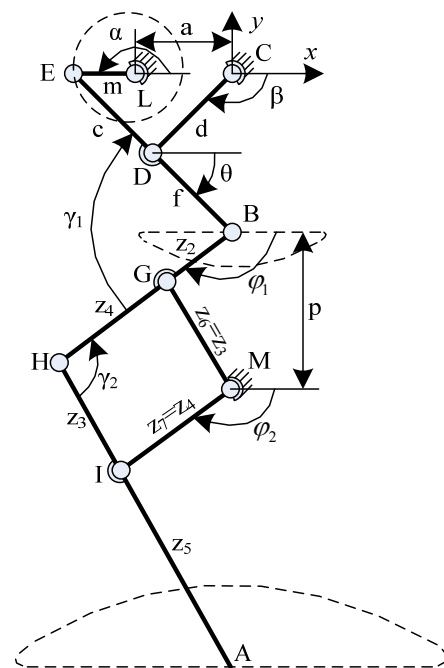


Figure 3 A scheme for the kinematic analysis of rickshaw leg.

When a reference system Cxy is attached at point C as shown in Fig. 3, the position of point B can be evaluated as a function of the input crank angle α and kinematic parameters of the Chebyshev mechanism LEBDC in the form

$$\begin{aligned} x_B &= -a + m \cos \alpha + (c + f) \cos \theta \\ y_B &= -m \sin \alpha - (c + f) \sin \theta \end{aligned} \quad (1)$$

in which

$$\theta = 2 \tan^{-1} [(-C_2 + \sqrt{C_2^2 - 4C_1C_3}) / 2C_1] \quad (2)$$

Coefficients C_1 , C_2 , and C_3 can be obtained by considering the closure equation of the four-bar linkage CLED in the form

$$\begin{aligned} C_1 &= a^2 - d^2 + m^2 + c^2 + 2ac - 2m \cos \alpha (c + a) \\ C_2 &= 4mc \sin \alpha \\ C_3 &= a^2 - d^2 + m^2 + c^2 - 2ac + 2m \cos \alpha (c - a) \end{aligned} \quad (3)$$

The position of foot point A with respect to the fixed frame can be obtained as

$$\begin{aligned} x_A &= x_B - (z_2 + z_4) \cos \varphi_1 + (z_3 + z_5) \cos \varphi_2 \\ y_A &= y_B - (z_2 + z_4) \sin \varphi_1 - (z_3 + z_5) \sin \varphi_2 \end{aligned} \quad (4)$$

in which

$$\begin{aligned} \varphi_1 &= 2 \tan^{-1} [(-K_2 + \sqrt{K_2^2 - 4K_1K_3}) / 2K_1] \\ \varphi_2 &= \cos^{-1} [(-x_B + z_2 \cos \varphi_1) / z_3] \end{aligned} \quad (5)$$

where

$$\begin{aligned} K_1 &= x_B^2 - z_3^2 + z_2^2 + y_B^2 + p^2 + 2x_B z_2 + 2y_B p \\ K_2 &= -4(y_B + p z_2) \\ K_3 &= x_B^2 - z_3^2 + z_2^2 + y_B^2 + p^2 - 2x_B z_2 + 2y_B p \end{aligned} \quad (6)$$

The velocity of point A can be computed as

$$\begin{aligned} \dot{x}_A &= \dot{x}_B + \dot{\varphi}_1 (z_2 + z_4) \sin \varphi_1 - \dot{\varphi}_2 (z_3 + z_5) \sin \varphi_2 \\ \dot{y}_A &= \dot{y}_B - \dot{\varphi}_1 (z_2 + z_4) \cos \varphi_1 - \dot{\varphi}_2 (z_3 + z_5) \cos \varphi_2 \end{aligned} \quad (7)$$

in which the velocity of point B can be obtained by differentiating eq. (1) with respect to time. The acceleration of point A can be calculated by differentiating eq. (7) with respect to time.

By using equations (1) to (6), while giving a clockwise rotation to the crank LE around point L, numerical simulations can be computed to check the curve that is generated by point A, and to check the motion properties.

In the mechanical design, a T gear box (as C in Fig. 1) is used to transmit the motion to the cranks of the two legs. As shown in Fig. 1 and Fig. 4, these two cranks LE and LE' are collinear assembled and actuated by one motor. In Fig. 4, the left leg and the right leg are presented in real line and dashed line, respectively. The rickshaw robot can be modelled as part 1 (the biped mechanism) and part 2 (the chariot), when ground is named as 3, so that forces can be identified as shown. F_{31L} and F_{32} represent the forces exerted from 3 to the left leg and to 2, respectively. F_{31Lh} indicates the force of sliding friction from 3 to the left leg,

which is the horizontal component of F_{31L} ; and F_{32h} is the force of rolling friction from 3 to 2, which is the horizontal component of F_{32} . F_{31Lv} and F_{32v} are the vertical components of F_{31L} and F_{32} , respectively. F_{31Lv} will be measured by force sensors during experiments. τ is the driving moment given by motor. During a walking process, the foot on the ground and the wheel always move in opposite directions, which means the directions of F_{31Lh} and F_{32h} are opposite. F_{31Lh} is larger than F_{32h} , so that the legs push the ground to make the wheels pulled forward step by step.

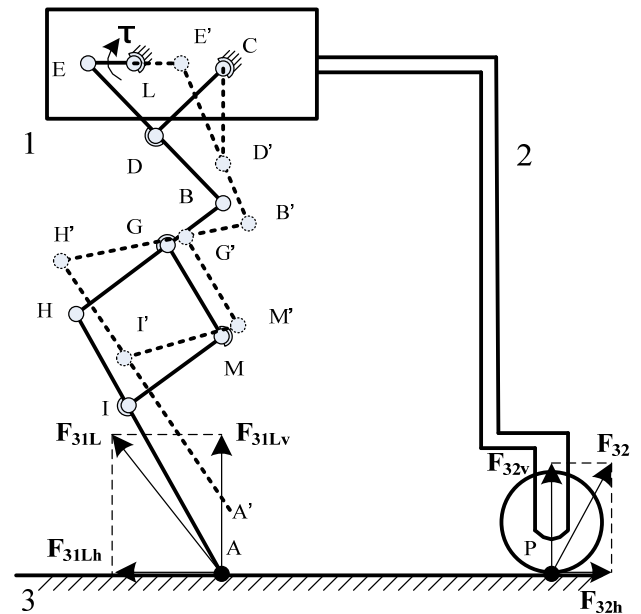


Figure 4 A scheme for force analysis of rickshaw operation.

3 AN EXPERIMENTAL LAYOUT

In order to evaluate the motion performance of the rickshaw robot, experiments have been designed and carried out to test main performance characteristics. The output results are contact forces between feet and terrain, the acceleration of the moving body, and the torque of the motor during a walking process.

Contact forces are measured by two force sensors that are installed on the bottom side of the feet. Each foot is equipped with one sensor. Piezoresistive force sensors have been used. This type of sensor has been chosen because of its small size (Fig. 5(a)) and low cost, as reported in [11]. Piezoresistive effect consists in a resistance variation of a suitable material when a contact force is applied on it. Therefore, it is necessary to use a proper conditioning board with the aim to obtain a tension output from a resistance variation. A conditioning board has been developed as base on the scheme of Fig. 5(b) [11], in which FSR represents the Force Sensing Resistor, and RM is a resistor chosen to maximize the desired force sensitivity range and to limit current. The current through the FSR should be limited to less than 1mA/cm² of applied force.

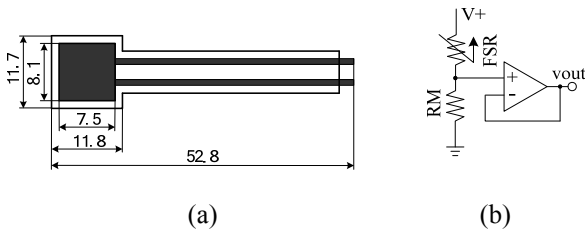


Figure 5 A piezoresistive sensor: (a) FSR150CP12 sensor with main dimensions in mm; (b) a basic scheme of a conditioning board.

A measured acceleration of the robot body can be calculated by

$$a = \sqrt{a_x^2 + a_y^2 + a_z^2} \quad (8)$$

in which a_x , a_y and a_z are the accelerations along x -axis, y -axis and z -axis, respectively. Components a_x , a_y and a_z can be measured by using a 3-axis accelerometer. Here a 3-axis low-g accelerometer MMA7260 [12] has been chosen and attached to the body of the biped mechanism as shown in Fig. 6.

As for measuring the torque of the motor, a resistance of 0.1Ω is used by measuring its input voltage. It forms a series circuit with the motor.

The data acquisition and elaboration are executed by a NI USB 6009 data acquisition board and a virtual instrument program in DAQ LabVIEW SignalExpress environment [13].

A scheme of the experimental system is shown in Fig. 7; and its experimental layout is shown in Fig. 6. The reference frame of the accelerometer is shown in Fig. 6.

Contact forces are measured to check if there is big impact during a walking. Accelerometer values are measured to check if the rickshaw robot has a smooth walking performance. The torque is measured to check if this rickshaw robot really does not require high power in operation.

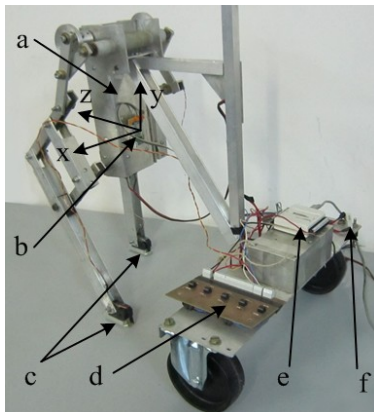


Figure 6 The experimental layout with a LARM rickshaw prototype (a-motor; b- accelerometer; c- force sensors; d- conditioning board; e- NI USB 6009; f- resistance).

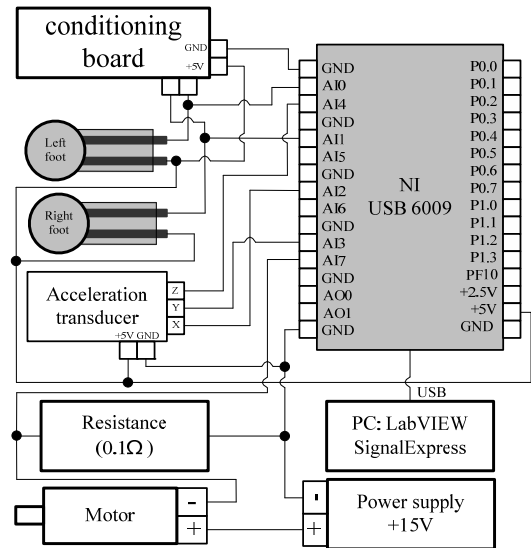


Figure 7 A scheme for the experimental system with LARM Rickshaw prototype.

4 EXPERIMENTS FOR CHARACTERIZATION

Three different types of experiments have been carried out for a characterization of the LARM rickshaw robot. The contact forces, the accelerations of the body, and the torque of the motor have been measured during each experiment. The first test has been carried out for a walking on a horizontal plane. Snapshots of this experiment are shown in Fig. 8. The whole process contains approximately three periods, when the biped leg mechanism walks six steps i.e. three steps for each leg.

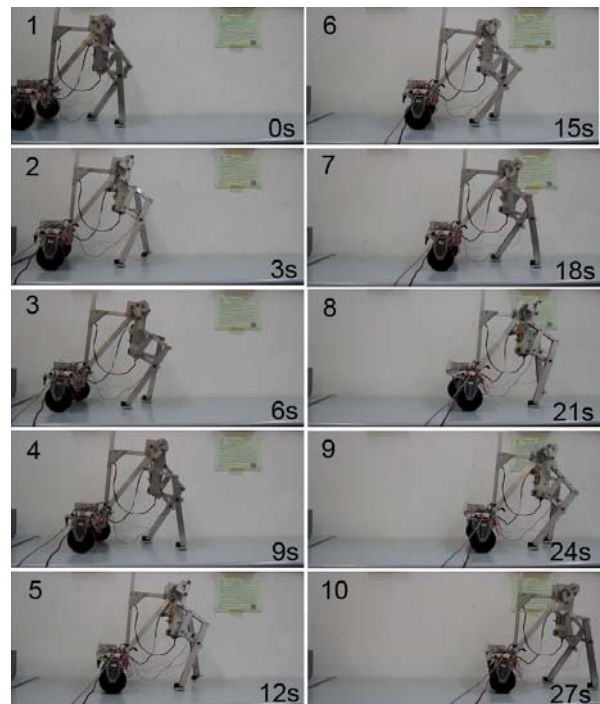


Figure 8 Snapshots of an experimental test of walking on a horizontal plane.

All experimental results are represented in forms of voltage output. They can be converted into force, acceleration and torque by using corresponding converting formulas, respectively.

Experimental results corresponding to forces on left and right foot are shown in Fig. 9 and Fig. 10, respectively.

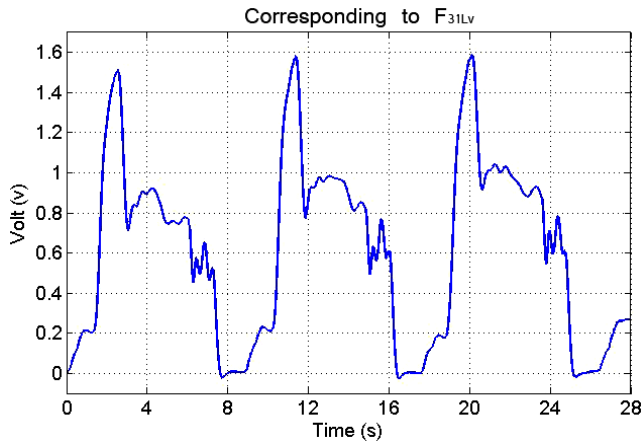


Figure 9 Voltage output for the contact force between the left foot and terrain (F_{31Lv}) with respect to time during the test in Fig. 8.

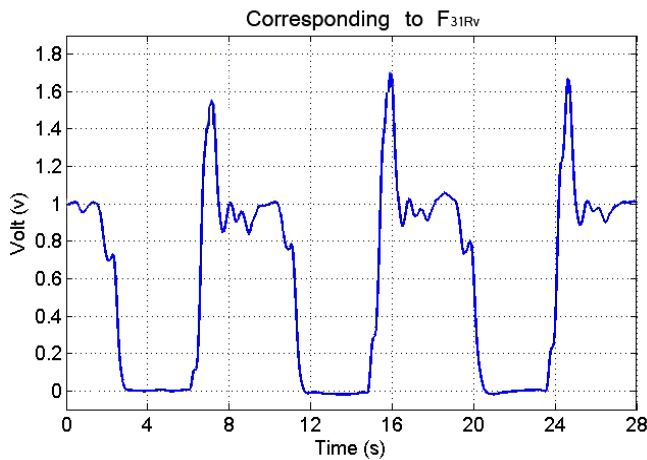


Figure 10 Voltage output for the contact force between the right foot and terrain (F_{31Rv}) with respect to time during the test in Fig. 8.

For a simple force-to-voltage conversion, the FSR device is tied to a measuring resistor in a voltage divider configuration. The output can be described by the expression

$$V_{OUT} = V / [1 + R_{FSR} / R_M] \quad (9)$$

In the configuration shown in Fig. 5(b), the output voltage increases with increasing force. If R_{FSR} and R_M are swapped, the output swing will decrease with all increasing force.

The measuring resistor, R_M , is chosen to maximize the desired force sensitivity range and to limit current. The current through the FSR should be limited to less than $1\text{mA}/\text{cm}^2$ of applied force. Suggested op-amps for single sided supply designs are LM358 and LM324. FET input devices such as LF355 and TL082 are also good. The low bias currents of these op-amps reduce the error due to the source impedance of the voltage divider. The conditioning board has been developed following this guidance.

A family of force vs. voltage curves is shown in Fig.11 for a standard FSR in a voltage divider configuration with various R_M resistors. A +5V power supply is used for these examples [14].

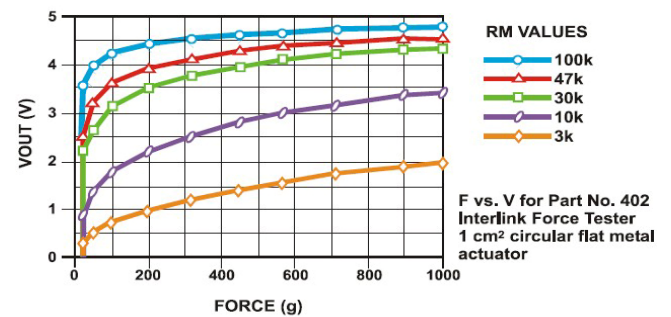


Figure 11 Force vs. voltage standard map, [14].

The R_M resistor used in these experiments has the value $3\text{k}\Omega$. Thus, the curve at the bottom of Fig. 11 is the needed one for converting voltage into contact force. From the outputted Volt curves shown in Fig. 9 and Fig. 10, both of the maximum voltages are less than 2V. Thus by using Fig.11, the contact force between feet and terrain can be computed as less than 10N. This means that there is no big impact existing during a walking process. Curves of left and right foot should have the same shape theoretically. However, in the prototype, there are some factors which make them differ from each other, like backlash, unsymmetry and friction.

As listed in Table 1, the used accelerometer is calibrated by logging its output voltage with positive and negative gravity. Therefore, converting coefficient K_{ai} ($i=x, y, z$) can be determined as

$$K_{ai} = 2g / (U_{ai}^g - U_{ai}^{-g}), (i = x, y, z) \quad (10)$$

where U_{ai}^g and U_{ai}^{-g} ($i=x, y, z$) are the original voltages under positive and negative gravity, respectively.

Thus, measured acceleration a_i ($i=x, y, z$) can be computed as

$$a_i = [U_{ai} - (U_{ai}^g + U_{ai}^{-g}) / 2] K_{ai}, (i = x, y, z) \quad (11)$$

where U_{ai} are the outputted voltages corresponding to the measured components a_x , a_y and a_z when i equals to x , y , and z , respectively.

Table I - A Calibration for Accelerometer

Gravity	-g (m/s ²)	g (m/s ²)
U _{ax} (V)	2.44	0.88
U _{ay} (V)	2.41	0.82
U _{az} (V)	2.43	0.84

If g is given with a value 9.8m/s^2 , from equations (10), (11), and table I, acceleration can be computed as

$$a_i = -12.25U_{ai} + 20.21, (i = x, y, z) \quad (12)$$

From eq. (12), values of a_x , a_y and a_z can be obtained as shown in Fig. 12, Fig. 13 and Fig. 14.

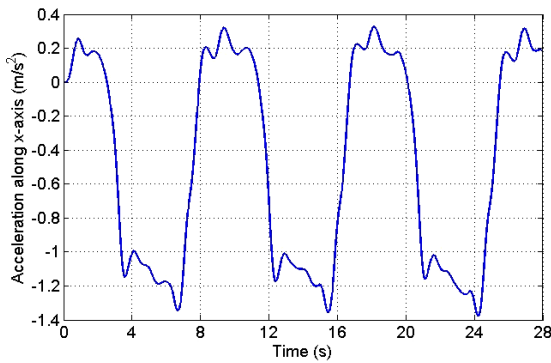


Figure 12 The acceleration of robot body along x-axis (a_x) with respect to time during the test in Fig. 8.

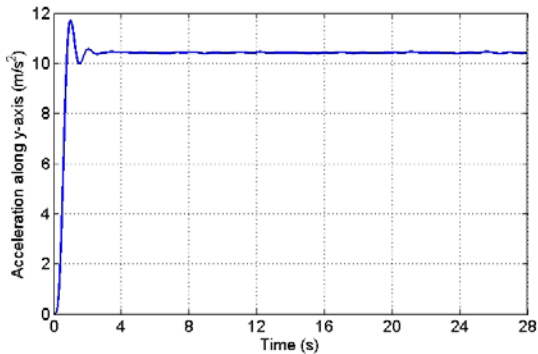


Figure 13 The acceleration of robot body along y-axis (a_y) with respect to time during the test in Fig. 8.

From Fig. 12, Fig. 13 and Fig. 14, it can be computed that the minimum and the maximum value of a_x are about 0.3m/s^2 and 1.4m/s^2 (the negative signs in Fig. 12 and Fig. 14 represent the directions), respectively. a_y seems like having much bigger values than a_x and a_z . In fact, it senses both the acceleration of gravity and acceleration along y-axis of rickshaw motion. Thus the value of a_y should be obtained by subtracting 9.8m/s^2 from the values shown in Fig. 13. The final result of the acceleration along y-axis of rickshaw is shown in Fig. 15. The values are around 0.55m/s^2 . The minimum and the maximum values of a_z are

approximately to 0.05m/s^2 and 0.4m/s^2 . In addition, Fig. 12, Fig. 13, and Fig. 14 show that the variations of a_x , a_y and a_z are small and the rickshaw robot has a smooth movement.

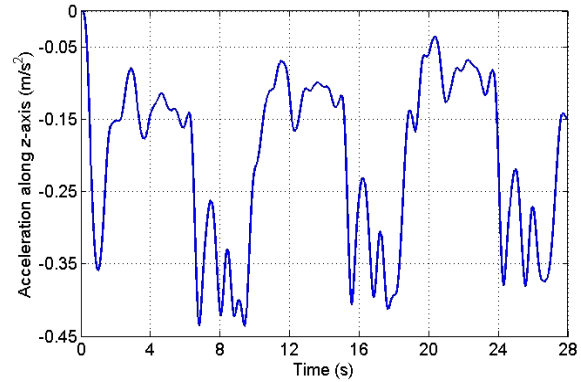


Figure 14 The acceleration of robot body along z-axis (a_z) with respect to time during the test in Fig. 8.

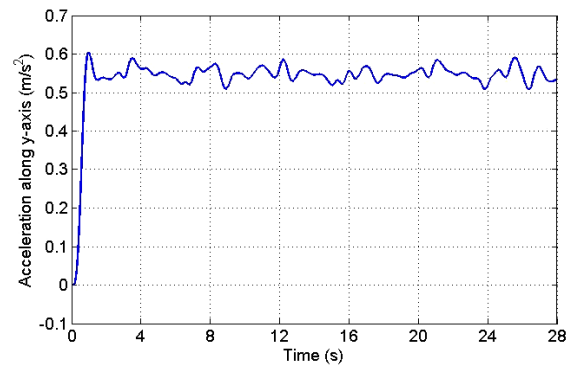


Figure 15 The acceleration of robot body along y-axis of rickshaw with respect to time during the test in Fig. 8.

The torque T of a DC motor can be computed by

$$T = CI_a \quad (13)$$

in which C is the torque constant of the motor. It equals to 0.1Nm/A for the used motor. I_a is the current of the motor that can be computed by

$$I_a = U_t / R \quad (14)$$

in which U_t is the measured voltage of R . R is the resistance that has the value 0.1Ω and forms a series circuit with the motor.

Finally, the computed T is shown in Fig. 16. The maximum torque of the motor is approximately to 0.118Nm , so that the rickshaw robot really does not require high power in operation.

The second experiment is a walking on a 10deg slope plane. In this experiment, a long table was used to make a slope with one side lifted from the ground. Snapshots of this experiment are shown in Fig. 17.

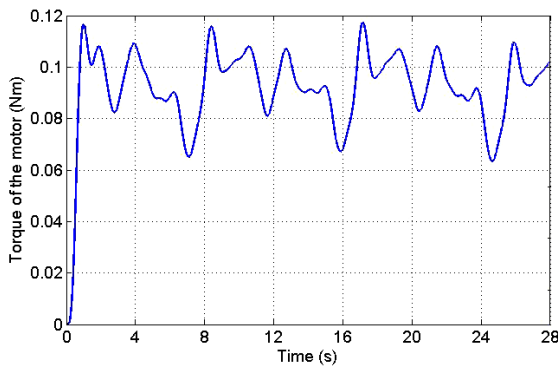


Figure 16 Voltage output for the torque of the motor (T) with respect to time during the test in Fig. 8.

During the walking process, the tabletop is so smooth that the friction force between the foot and table is not large enough, thus make the rickshaw robot has a slight retrograde motion. That's why this walking process took more time than the first one with a same displacement. However, this is just because each foot is installed with a force sensor. In order to guarantee a good measurement of the contact forces, the contact area between foot and slope plane is just the area of the force sensor. It's very small and smooth. While in practical applications, rough materials can be used to manufacture the feet to enable the rickshaw robot climb those slopes with larger inclination. In addition, if the slope planes are also rough, the inclination can be even larger.

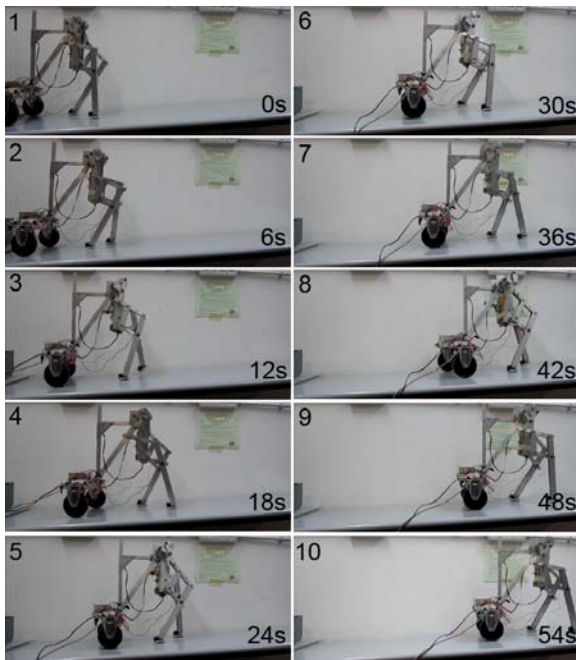


Figure 17 Snapshots of an experimental walking on a 10deg slope plane.

Measured results of the contact forces between feet and slope plane, the accelerations of the body, and the torque of the motor are shown in Fig. 18 to Fig. 23, respectively.

These results are similar to those measured during the first experiment. They verified that the rickshaw robot has good motion properties yet, i.e. no big impact existing during the walking; the LARM rickshaw robot has a smooth motion; and the needed power is very small.

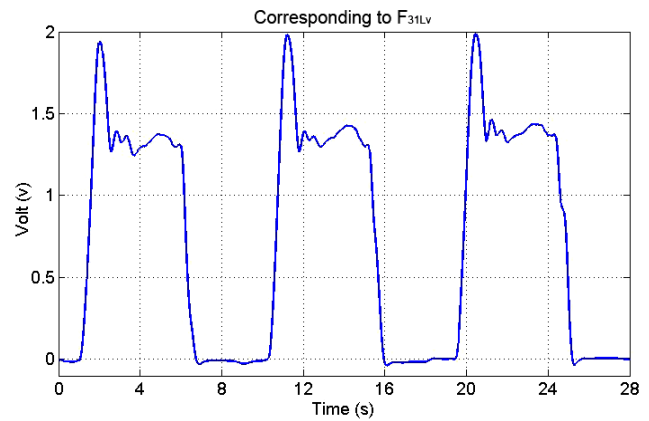


Figure 18 Voltage output for the contact force between the left foot and terrain (F_{31Lv}) with respect to time during the test in Fig. 17.

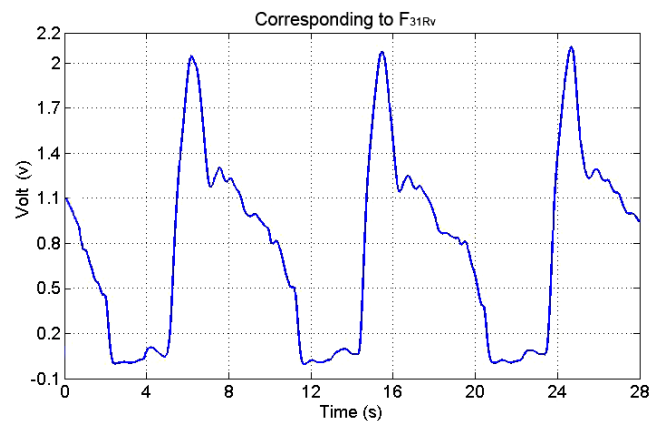


Figure 19 Voltage output for the contact force between the right foot and terrain (F_{31Rv}) with respect to time during the test in Fig. 17.

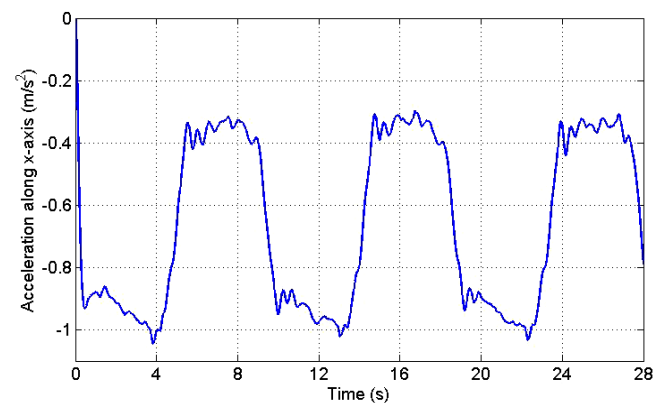


Figure 20 The acceleration of robot body along x -axis (a_x) with respect to time during the test in Fig. 17.

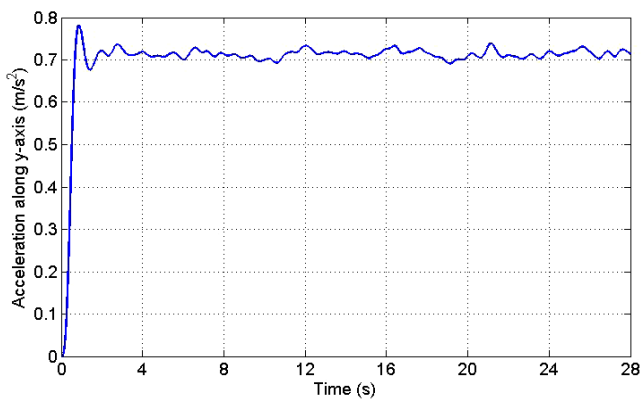


Figure 21 The acceleration of robot body along y-axis of rickshaw with respect to time during the test in Fig. 17.

The third experiment is a walking on a horizontal plane with a 15-kg payload. The payload was installed on the passive two-wheeled chariot. Snapshots of this experiment are shown in Fig. 24. During this experiment, no retrograde motion occurred. Thus the time is nearly the same as that in the first experiment.

Measured results of the contact forces between feet and plane, the accelerations of the body, and the torque of the motor are shown in Fig. 18 to Fig. 30, respectively.

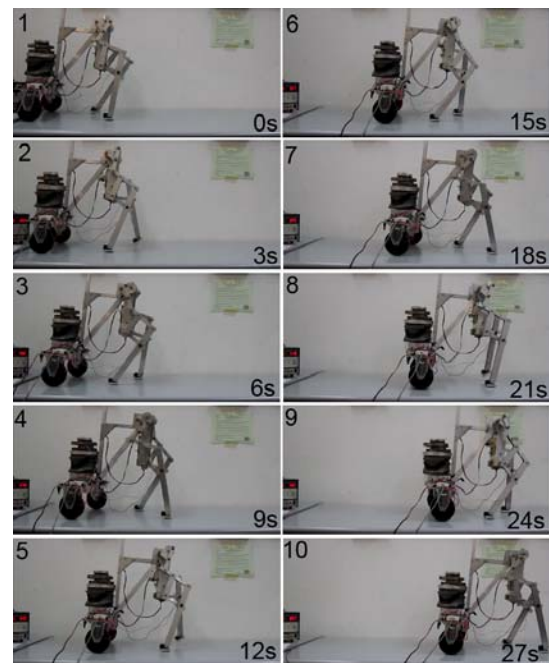


Figure 24 Snapshots of an experimental walking with a 15-kg payload.

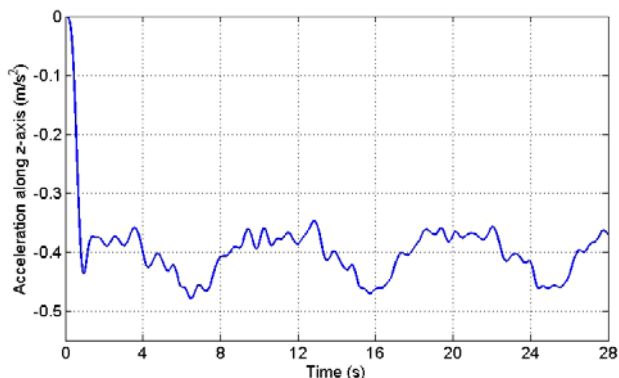


Figure 22 The acceleration of robot body along z-axis (a_z) with respect to time during the test in Fig. 17.

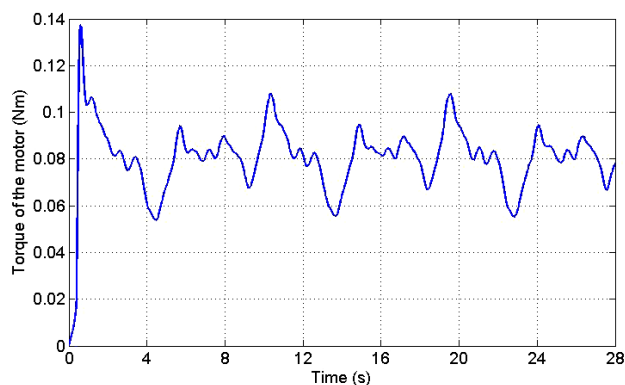


Figure 23 Voltage output for the torque of the motor (T) with respect to time during the test in Fig. 17.

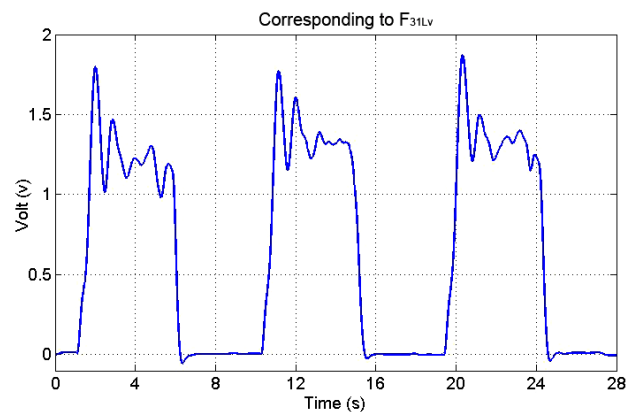


Figure 25 Voltage output for the contact force between the left foot and terrain (F_{31Lv}) with respect to time during the test in Fig. 24.

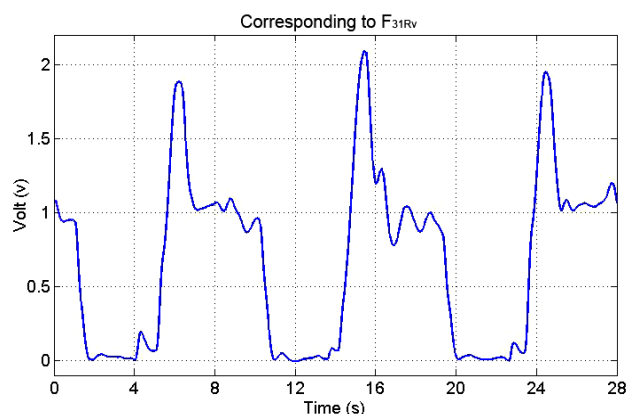


Figure 26 Voltage output for the contact force between the right foot and terrain (F_{31Rv}) with respect to time during the test in Fig. 24.

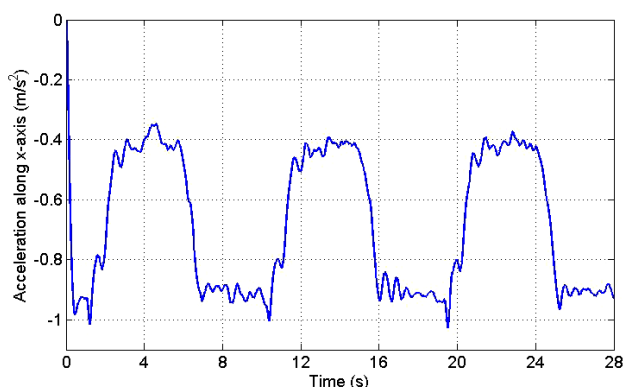


Figure 27 The acceleration of robot body along x -axis (a_x) with respect to time during the test in Fig. 24.

The results that have been measured in this experiment are again similar to those during the first and second experiments. They verified that the LARM rickshaw robot has good motion properties also with high load condition, i.e. no big impact existing during the walking; the rickshaw robot has a smooth motion; and the needed power is very small. In other words, this LARM rickshaw robot has a good payload capacity comparing to its weight.

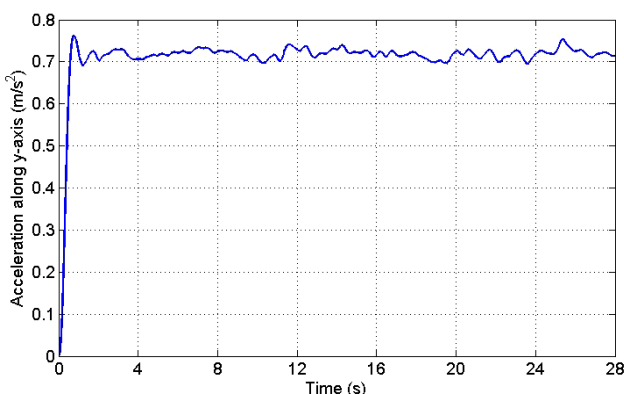


Figure 28 The acceleration of robot body along y -axis of rickshaw with respect to time during the test in Fig. 24.

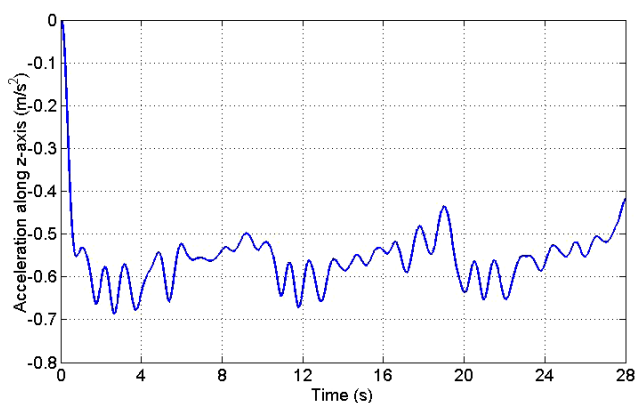


Figure 29 The acceleration of robot body along z -axis (a_z) with respect to time during the test in Fig. 24.

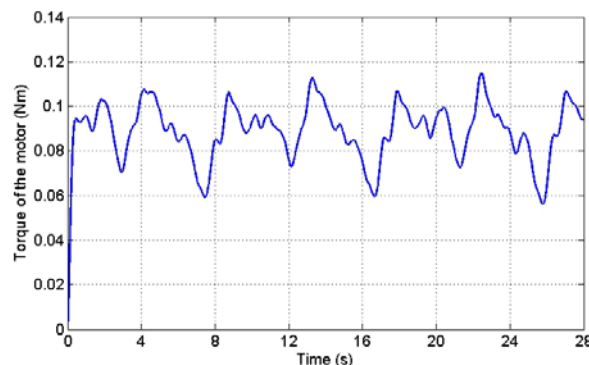


Figure 30 Voltage output for the torque of the motor (T) with respect to time during the test in Fig. 24.

5 CONCLUSIONS

A LARM rickshaw robot has been characterized from aspects of mechanical design, kinematic modelling and experimental tests. Experiments have been carried out to measure the contact forces between feet and terrain, the acceleration of the robot body and torque of the motor during a walking process. Experimental results show that the LARM rickshaw robot has good performance, namely the output forces do not show large foot impact during a walking process; the measured acceleration show that the robot has a smooth motion; and the measured torque verifies that the rickshaw robot does not require high power for its operation.

ACKNOWLEDGEMENT

The first author likes to acknowledge Chinese Scholarship Council (CSC) for supporting his PhD study and research at LARM in the University of Cassino in Italy for the years 2010-2012.

REFERENCES

- [1] Yuan, J., Hirose, S., Zero carrier: a novel eight leg wheels hybrid stair climbing mobile vehicle, *Journal of Robotics and Mechatronics*, 2005, 17:44–51.
- [2] Modianot-Fox, D., Rickshaws reinvented–The ancient transportation takes a modern turn, <http://www.smithsonianmag.com/people-places/rickshaw.html>, March 01, 2007.
- [3] World news, *Chinese rickshaw robot*, <http://wn.com/Chinese Rickshaw Robot>, 2011.
- [4] Ceccarelli M., Carbone G., Ottaviano E., and Lanni. C., Leg Designs for Walking Machines at LARM in Cassino, *ASI workshop on Robotics for moon exploration*, Rome, July, 2009
- [5] Ceccarelli M., Carbone G., A Study of Feasibility for a Leg Design with Parallel Mechanism Architecture, *IEEE/ASME Conference on Advanced Intelligent Mechatronics AIM'09*, Singapore, 2009, paper no. 131.

- [6] Ceccarelli M., M., Figliolini, G., Lanni, C., Ottaviano, E., A Study of Feasibility for Rickshaw Type Mobile Robot, *IEEE International Conference on Industrial Electronics, Control and Instrumentation*, Nagoya, 2000, paper MT9-MRC-2.
- [7] Tavolieri, C., Ottaviano, E., Ceccarelli, M., Design and problems of a new leg-wheel walking robot., *10th CLAWAR International Conference on Climbing and Walking Robots*, Singapore, 2007, pp. 319-328.
- [8] Ottaviano E., Grande S., Ceccarelli M., A Biped Walking Mechanism for a Rickshaw Robot, *Mechanics based design of structures*, 38: 227-242, 2010.
- [9] Rosheim, M. E., *Robot Evaluation*, New York: Wiley, 1994.
- [10] Morecki, A., Waldron, K. J., *Human and Machine Locomotion*, New York: Springer, 1997.
- [11] Konteck C., *Specification Sheet for Standard Lusense Sensors of PS³ Family*, 2001.
- [12] Freescale Semiconductor Technical Data, *±1.5g-6g Three Axis Low-g Micromachined Accelerometer*, Document Number: MMA7260QT, Rev 5, 03, 2008.
- [13] National Instruments Corporation, *User guide and specifications NI USB-6008/6009*, May 2008 Edition, Part Number 371303L-01, 2008.
- [14] Interlink Electronics Inc., *FSR Integration Guide and Evaluation Parts Catalog with Suggested Electrical Interfaces*, Version 1.0, 90-45632 Rev. D, 2007.

A CONTROL SYSTEM FOR ROBOT TRAJECTORY PLANNING: ALGORITHM AND FIRST EXPERIMENTAL RESULTS

Cesare Rossi

Sergio Savino

Department of Mechanics and Energetics, Università di Napoli "Federico II", Italy

ABSTRACT

A technique for robot trajectories planning was proposed and developed. By means of the latter, a better precision of the trajectory itself was achieved. This was obtained by assigning not only the points that the end-effector must go across are assigned but also the tangent lines to the path in each of those given points. The latter condition is achieved by assigning the velocity of each of the joints in the joint space.

In order to evaluate the proposed algorithm, a control system was developed for a robot arm which was also designed at the Di.ME.

In the paper are also reported some test results for comparisons between the trajectories obtained by traditional techniques and those obtained by the proposed technique. The comparisons clearly show that, generally, by the proposed technique paths closed to the planned ones are obtained, also assigning a much lower number of points.

Keywords: Robot Mechanics, Trajectory Planning

1 INTRODUCTION

The main goal of the robot trajectory planning consists into generate those inputs for the control system that will make the end-effector move along a given path or following a given trajectory.

The end-effector path in the work space is assigned, essentially, by means of two methods: simply by giving the start point and the finish point or, more frequently, by giving a number of mid-points that are assigned in order to obtain a defined path. In both cases, the curve that links two consecutive points is stated by the laws of motion of each of the joints that is "established" by the control system.

A single criterion by means of which it is possible to choose the better trajectory does not exist; anyway some aspects must be taken onto account in order to make, each time, the right option. These aspects essentially depend on the following aspects:

1. Characteristics of the working cycle.
2. Limits due to the robot mechanical structure.
3. Mechanical and electrical limits of the actuators.
4. Limits of the transmissions.
5. Limits of the control system. These are essentially due to non-linearities, numerical problems (numerical errors in the data computing and/or possibility of overflow) and also to the maximum frequency of the control system work.
6. Undesired mechanical phenomena, due to the elasticity of the mechanical components, the presence of backlashes and to working irregularities of dome components.

The main aim of this research is to propose and to tune up an innovative method for the path planning in order to obtain path closer to the desired ones but using a much lower number of mid-points..

2 LIMITS OF THE POINT-TO-POINT TRAJECTORY PLANNING

From a general point of view, a trajectory planned by means of assigning points only, has some "intrinsic" limits. In the point to point motion, the manipulator moves from an initial configuration of the joint variables to a final one in a given time. First of all, it must be considered that, in any case, the displacement and the velocity of each of the

Contact author: Cesare Rossi¹

¹ Department of Mechanical Engineering for Energetics,
University of Naples "Federico II"
Via Claudio 21, 80125, Naples, Italy
E-mail: cesare.rossi@unina.it

link must be continuous, this because discontinuities are, obviously, physically impossible. In the industrial robots, frequently polynomial mixed laws of motion are adopted; in this case a trapezoidal shape for the joint velocity is adopted; this means a constant acceleration in the first part of the motion, a cruise speed during the mid-part and constant deceleration during the last part of the motion. A typical joint law of motion $q(t)$ and its derivatives are shown in Figure 1.

If a given path must be obtained with a better precision, it is suitable to assign a number of points on the path; these points will be closer in those parts of the path where obstacles must be avoided or where the path has a small radius of curvature.

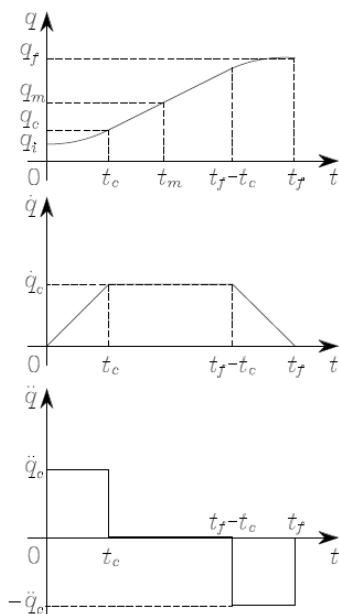


Figure 1 Laws of motion for a point to point motion.

This kind of path planning has several disadvantages:

1. It is impossible to assign the start and end velocities.
2. As the degree of the polynomial rises, its oscillatory nature increases; this can cause sharp trajectories.
3. The numerical precision achieved in computing is reduced as the degree of the polynomial rises.
4. Once the constrain equations is written it is more complicated to solve it.
5. The coefficients of the polynomial depend from all the assigned points; so, if just one point is changed, all must be computed again.

The problems above can be overcome if, instead of using a unique interpolation polynomial with a high degree, a suitable number of interpolation polynomial with a low degree is used; these will be linked, one another, by the assigned points.

The easier technique consists in using, between each couple of given points on the path, the same velocity shape shown in Figure 1. This brings, for the entire path, to a joint

velocity diagram like that reported in Figure 2 and to a joint displacement diagram like the one reported in Figure 3. From the figures above, it is possible to observe that, although the assigned mid-points are fulfilled, at each of them the velocity is zero; this means a non continuous motion of the end effector.

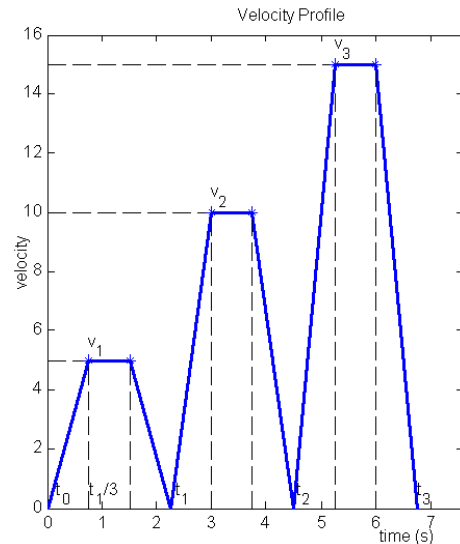


Figure 2 Joint velocity diagram for some mid-points.

A widely used algorithm to obviate this problem consists in overlapping the adjoining velocity shapes (see e.g. [4]), so that the velocity at the mid-points is no more zero, and assuring that each of the points is full filled. This is obtained by starting in advantage each of the new velocity shape that should have been followed once the given point was reached.

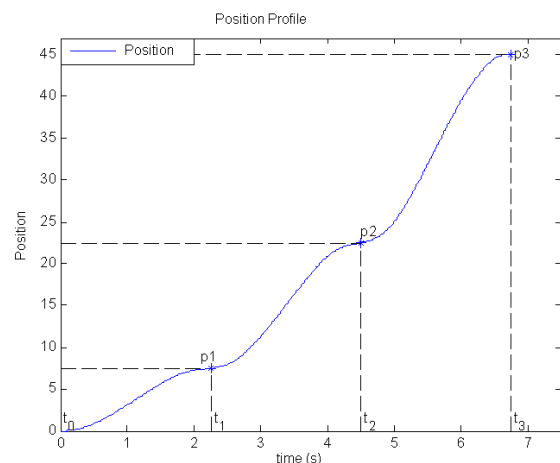


Figure 3 Joint displacement diagram for some mid-points.

In Figure 4 an example of what above said is shown. Thus, by advancing by Δt_i of the (i-1)th velocity shape the (i)th shape, a new velocity shape is obtained; hence the latter is

obtained by joining the two trapeziums as in figure. This permits a smooth and regular velocity shape and avoids that the velocity becomes zero at the mid-points; nevertheless, in general, there is tendency to miss the mid-points, how it is shown in Figure 5.

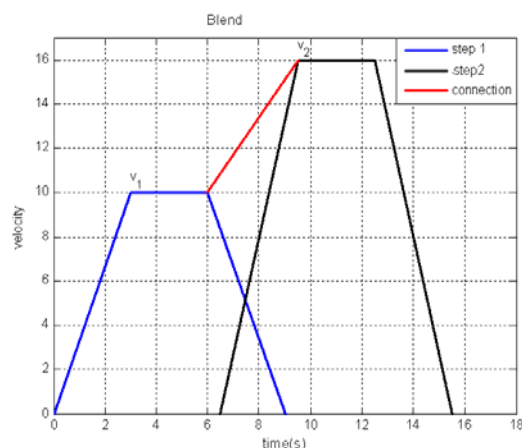


Figure 4 Blend of velocity shapes.

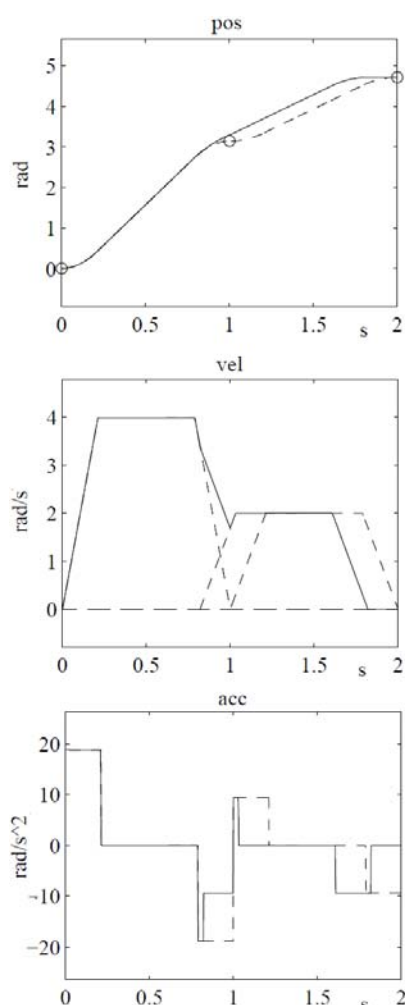


Figure 5 Missing of the mid-points due the blend.

If the fulfilment of each of the mid-points is needed, it would be necessary that the area under the velocity shape for each of the assigned periods of time exactly equals the desired displacement; so, it will be necessary to adapt the velocity shapes by changing the cruise speeds or the accelerations.

3 TRAJECTORY PLANNING BY ASSIGNING POINTS AND TANGENT LINES

From what reminded above, it comes that, if just mid-points are assigned on the path, the shape of the latter will depend from the laws of motion of the joints. This is shown in Figure 6.

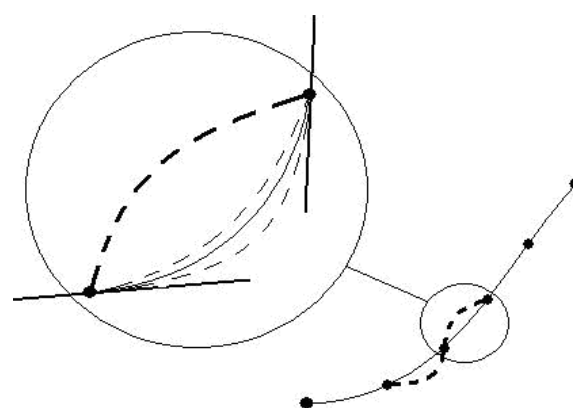


Figure 6 Path and mid-points.

In the figure the assigned path is indicated with a thin line; it is possible that the path really described by the end-effector between two mid-points is the one indicated by a thick dotted line. Now, let us imagine to impose that not only the end-effector fulfils the mid-points but also that, at each of them, the end-effector velocity has the same direction of the tangent line to the assigned path. In this case, the path really obtained will be similar to one of those indicated with a thin dotted line in figure; that is to say it will be possible that the real path will significantly differ from the assigned one.

In order to obtain that the end-effector velocity has the same direction of the tangent line, the steps are conceptually the followings:

1. A number of mid-points are assigned on the planned path.
2. For each of the mid-points above, the corresponding positions of the joints are computed by means of the inverse kinematics.
3. For each of the mid points the velocity vector is assigned by its magnitude and its direction and sense, since the last two are the tangent line to the path; so, it is easy to compute the velocity of each of the joints at each of the mid-points, by means of the Jacobian matrix of the robot.

In this way, for each of the joints, a set of velocities and positions values are obtained; these are given to the control

system. So, each of the servomotors will follow a law of motion, changing at each instant of time, so that the end-effector will fulfil each of the mid-points having at each of them the assigned magnitude, direction and sense of the velocity.

Thus, by the described technique, that will be called “trajectory planning by tangent envelope”, the interpolating polynomial between two mid-points and its derivative must have assigned values at the given mid-points.

3.1 LAWS OF MOTION COMPUTING WITH THE TRAJECTORY PLANNING BY TANGENT ENVELOPE

The inputs necessary to compute the laws of motion of the joints are the followings:

1. The positions $\{q_i\}$ that must be reached by each of the joints in order to describe the assigned path; this is obtained by inverse kinematics by which the positions of each of the joints are computed in order to fulfil the assigned mid-points.
2. The joint velocities $\{\dot{q}_i\}$ at each of the mid-points; these are computed by means of the Jacobian matrix of the robot, starting from the end-effector velocity vector that was assigned in magnitude, direction and sense.
3. The time for each of the displacement; this time essentially depends on the end-effector law of motion that must be obtained in the work space.

In order to obtain the velocity shape between a mid-point and the next one in the joint space, the corresponding time interval was divided in three equal sub-intervals. Said Δt_i the time interval needed to move from a point p_{i-1} at the time t_{i-1} to a point p_i at the time t_i , each sub-interval will be: $\Delta t_i/3$. In particular, during the first or the third sub-interval, will accelerate or decelerate, depending on the velocities that are imposed at the mid-points p_{i-1} and p_i ; that is to say, depending on the difference between the velocities that were planned. The mid sub-interval is necessary to make that the area under the velocity curve equals the space that must be covered. Figure 7 shows the velocity shape described above.

By the velocity shape shown in Figure 7, the law of motion shown in Figure 8 is obtained.

In detail, it was done as follows:

In order to go from a mid-point to the next one in which the velocity magnitude is different, the velocity in the mid sub-interval of the velocity diagram is increased (or decreased); in this way the displacement will be the one that was planned and the time that was stated by the trajectory planning will be fulfilled.

In particular, the velocity in the mid sub-interval of the velocity diagram is computed after the displacement, the initial velocity, the final velocity and the time necessary to cover the displacement have been fixed. From the velocity diagram, the displacement is:

$$\begin{aligned} s(t) &= \frac{t_f - t_i}{3} \cdot \frac{v_i + v^*}{2} + \frac{t_f - t_i}{3} \cdot v^* + \\ &+ \frac{t_f - t_i}{3} \cdot \frac{v_f + v^*}{2} = \\ &= \frac{t_f - t_i}{3} \cdot \frac{v_i + v_f + 4 \cdot v^*}{2} \end{aligned} \quad (1)$$

where:

s = displacement

t_i = initial time

t_f = final time

v^* = cruise velocity in the mid sub-interval

v_i = velocity at initial point in the instant of time t_i

v_f = velocity that must be reached at final point in the instant of time t_f

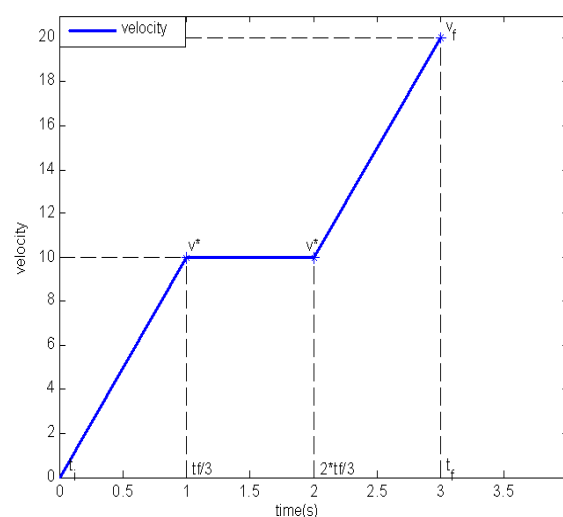


Figure 7 “Three lines” velocity shape.

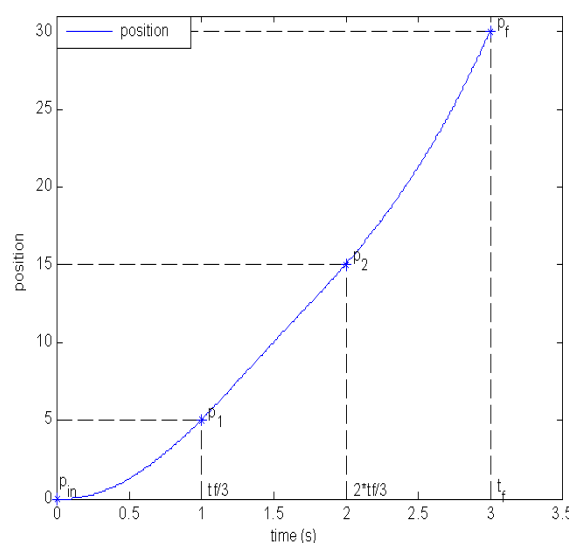


Figure 8 Law of motion for a “three lines” velocity shape.

So, the velocity in the mid sub-interval will be:

$$v^* = \frac{3 \cdot s}{2 \cdot (t_f - t_i)} - \frac{v_f + v_i}{4} \quad (2)$$

It must be observed that the existing algorithm and the one here proposed, if no further specifications are given, do not assure that the maximum acceleration will not exceed the possible limit, so it is always necessary that the control system must verify the respect of the limits of the acceleration.

4 THE CONTROL SYSTEM

In order to test the proposed technique, a number of trajectories have been planned and recorded. The latter were obtained by a revolute robot prototype that was also designed and built at the Di.M.E. and was already described in several papers, see e.g. [1-3]. The robot control system has been modified both in terms of hardware and software; this in order to permit to assign those laws of motion to the joints, that were needed to use the technique "envelope of tangents".

4.1 CONTROL SYSTEM DESCRIPTION

The new control system is developed using two interface PCI cards between the computer and the manipulator. Both cards are manufactured by National Instruments interfaced with the development environment Matlab / Simulink, and this has made possible the development of software management and control.

In a classical structure of a control system, shown in figure 9, one of the two cards (NI 6602) acts on the feedback line by providing the measured data, which in our case are the encoders data. The second card (NI 6733) allows, by acting on the line of action, to send the control signals suitably processed on the basis of the error of position determined by the deviation between the reference trajectory generated and that actually followed by the robot.

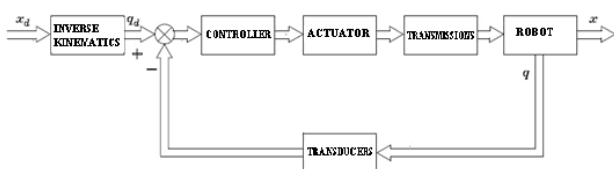


Figure 9 structure of feedback control.

In order to complete the control system, the error signal must be processed and, therefore, the presence of a controller is necessary. In order to be able to replicate the behavior of the pre-existing robot control system (as far as the classical motion planning is concerned) a PID controller with action of feed – forward has been adopted. Finally, the reference trajectory was generated on the basis of the desired positions in the joint space, through some computer programs written in Matlab.

Using the toolbox "Real time windows target" of the development environment Matlab / Simulink, a control model has been developed as shown in Figure 10.

This model consists in 5 main blocks:

- three-axis control blocks, one for each joint;
- a block for the award of the final positions of individual joints;
- a block for the data acquisition in real time in order to have always available the signals of interest for any analysis.

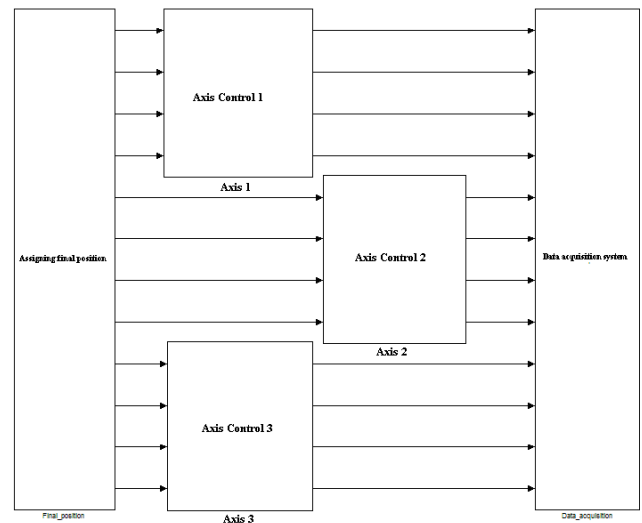


Figure 10 Model of the control system.

Figure 11 shows the structure of the generic block "Axis Control".

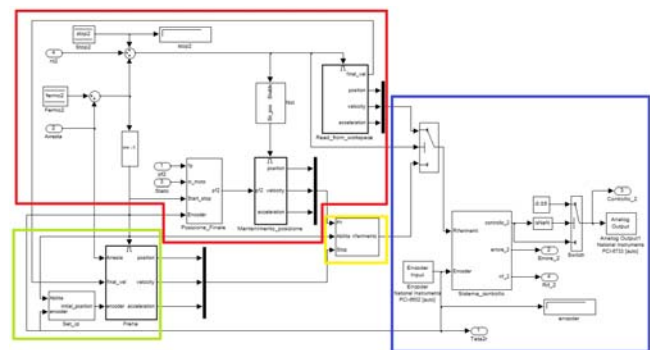


Figure 11 Structure of the generic block "Axis Control"

In the control scheme four areas highlighted in different colors can be distinguished.

The red zone, in addition to the signals of start, end motion and stop, contains three subsystems. Two of them are mutually exclusive (Position Control and Read_from_Workspace) and provide instant by instant the reference positions to the control system in the joint space, and the third one (Final Position) allows to define on the basis of the signals of the encoders, the final position to be provided to the robot.

The green zone contains two blocks (Brake and Set_ip). Such blocks permit to manage the robot if there is the need to stop the motion for emergency situations. These blocks are activated when the user makes use of a stop button, in this case the block “*Brake*” will generate the trajectories to stop the robot in the shortest possible time.

The yellow zone is composed of a single block and allows to select the value to provide the robot to its final position, which is that planned or the one to be reached in case of emergency.

The blue zone contains, in addition to the blocks of the two PCI cards to read encoders and to send signals, a subsystem in which the two control actions are performed: PID and feed-forward.

4.2 USER CONTROL INTERFACE

To make the control system user - friendly, it was necessary to design and to develop an interface that permits to manage the robot in a complete manner. By means of this interface, it is possible to manage the robot handling, data storage and visualization. Figure 12 shows this interface.

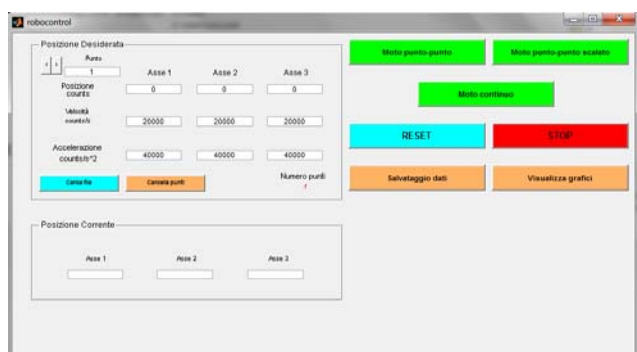


Figure 12 User control interface.

In the upper left corner it is possible to enter the data that are supplied to the robot for its movement.

For each axis it is possible to assign the final position, velocity and acceleration to be performed at each of the points. That is to say, in the joint space.

It is also possible to assign the points of the path together with the speed and the acceleration of the end-effector at each of those assigned points. This was made by means of the option (“*Carica File*”) that permits to load the data through a text file.

Another button (“*Cancella Punti*”) permits to clean this section of the graphics interface.

In the lower left corner the current position of the three joints can be read.

On the right side of the GUI there are some buttons that permit different operational choices and help to manage the input and output robot data.

The green buttons (“*Moto punto – punto*”, “*Moto punto – punto scalato*”, “*Moto continuo*”) permit the choose of the type of motion planning that has to be assigned to the robot movements.

The blue key of Reset permits to send the robot in its reset position.

The red Stop button allows to instantly stop the motion of the robot.

Finally, there are two orange keys that enable the management of the data input and output of the robot. In particular, the button “*Salvataggio dati*” saves (in an external file) the input data that were sent to the robot and the output data that were provided by the robot itself.

The button “*Visualizza grafici*” permits to view the graphics requested by user.

5 AN EXAMPLE OF EXPERIMENTAL RESULTS

In the followings, as example, results referred to a path having the shape of a cylindrical helix are reported. The planned path dimensions are reported in Table I.

Table I - Cylindrical helix parameters

Radius (mm)	N. of twists	Pitch (mm)	Time (s)	N. of points
50	4	75	20	200

In Figure 13 are reported: the ideal cylindrical helix and two experimental paths; one of the experimental path was obtained by means of the proposed technique and the other one was obtained by a point to point planning. Both the experimental paths were obtained by assigning only 200 mid-points.

In Figure 14, a particular of Figure 13 is shown.

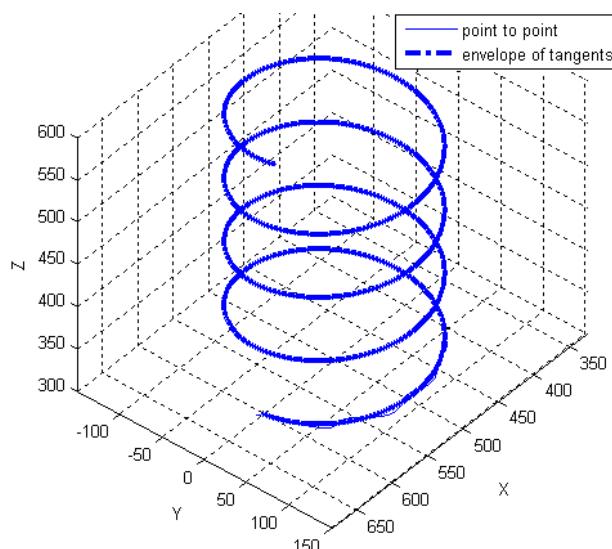


Figure 13 Cylindrical helix paths.

How it can be observed, the precision achieved by the proposed technique is higher.

In Figure 15 are reported the joint velocities obtained with both the techniques and in Figure16 a detail of Figure 15 is shown.

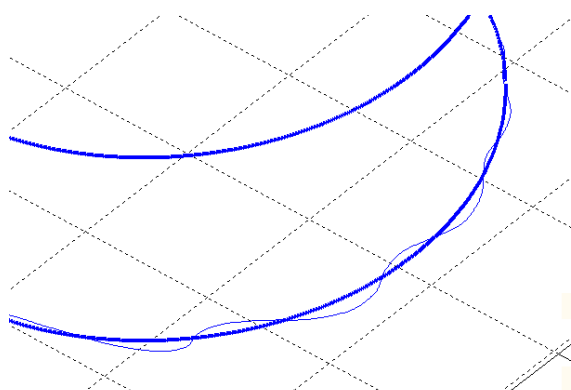


Figure 14 Cylindrical helix paths, particular.

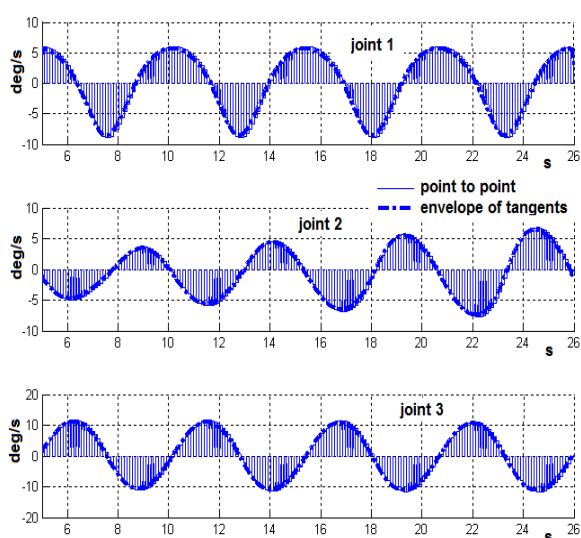


Figure 15 Joint velocities.

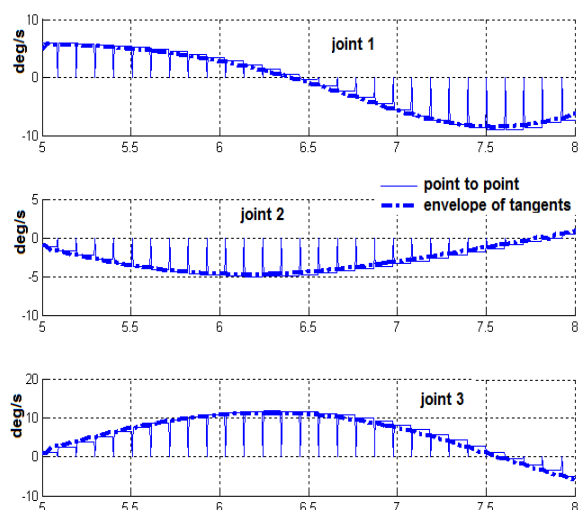


Figure 16 Joint velocities, particular.

From the last two figures, wide joint velocity variation are observed when the point to point technique is used; this could cause oscillatory behaviours of the manipulator.

6 CONCLUSION

A new technique for the robots path and trajectory planning was presented.

The proposed technique has been tested by a suitable control system that was designed, made and developed at our laboratory.

Conceptually, if compared with the point to point techniques, the advances of the proposed technique mainly consist in the following aspects:

1. Lower oscillations of the velocity shapes that means lower stresses of the control system.
2. Possibility of controlling the end-effector velocity during the trajectory.
3. Better fulfilment of the assigned path, especially in those parts of the path where big variations of the pitch of the tangent line to the path are present.
4. Possibility of obtained accurate paths with a much lower number of mid-points.

From an operational point of view, the advantages above were confirmed by a number of experimental tests. From the latter the previously mentioned advantages (1-4) are clearly evident.

The proposed technique does not always need, a dedicated hardware of the control system: it is necessary, in fact, to modify the law of motion computed by equation (1).

REFERENCES

- [1] Brancati R., Rossi C. and Scocca S., An experimental planar manipulator controlled in the joint space - *INES 2000*, Portoroz, Slovenia, September 17-19, pp. 125-128, 2000.
- [2] Pagano S., Rossi C. and Timpone F., A low cost 5 axes revolute industrial robot design - *Proc. of 11th int. Workshop RAAD 2002*, Balatonfüred, Hungary, June 30 – July 2, pp. 117-122, 2002.
- [3] Brancati R., Rossi C., Savino S. and Vollono G., A robot prototype for advanced didactic. *Proc. of 13th int. Workshop RAAD 2004*, Brno, Czech Republic, June 2-5, pp. 293-298, 2004.
- [4] Brancati R., Rossi C. and Savino S., A method for trajectory planning in the joint space. *Proc. of 14th International Workshop on Robotics in Alpe-Adria-Danube Region*, Bucharest, Romania, May 26-28 pp. 81-85, 2005.
- [5] Beiner L., Time optimization of the continuous-path motions of industrial robots, *Advanced Robotics*, Volume 6, Number 3, 1991, pp. 291-305.
- [6] Somló J. and Loginov A., Energetically optimal cruising motion of robots, *IEEE Conference on Intelligent Engineering Systems*, Budapest, 1997.
- [7] Broquere X., Sidobre D. and Herrera-Aguilar I., Soft motion trajectory planner for service manipulator robot. *IEEE/RSJ IROS*, Nice, France, 2008.
- [8] Broquère X., Sidobre D. and Nguyen K., From motion planning to trajectory control with bounded jerk for

service manipulator robots. *International Conference on Robotics and Automation (ICRA)*, Anchorage, AK, 3-7 May, ISSN: 1050-4729, ISBN: 978-1-4244-5038-1, pp. 4505-4510, 2010.

TEMPLATE FOR PREPARING PAPERS FOR PUBLISHING IN INTERNATIONAL JOURNAL OF MECHANICS AND CONTROL

Author1* Author2**

* affiliation Author1

** affiliation Author2

ABSTRACT

This is a brief guide to prepare papers in a better style for publishing in International Journal of Mechanics and Control (JoMaC). It gives details of the preferred style in a template format to ease paper presentation. The abstract must be able to indicate the principal authors' contribution to the argument containing the chosen method and the obtained results. (max 200 words)

Keywords: keywords list (max 5 words)

1 TITLE OF SECTION (E.G. INTRODUCTION)

This sample article is to show you how to prepare papers in a standard style for publishing in International Journal of Mechanics and Control.

It offers you a template for paper layout, and describes points you should notice before you submit your papers.

2 PREPARATION OF PAPERS

2.1 SUBMISSION OF PAPERS

The papers should be submitted in the form of an electronic document, either in Microsoft Word format (Word'97 version or earlier).

In addition to the electronic version a hardcopy of the complete paper including diagrams with annotations must be supplied. The final format of the papers will be A4 page size with a two column layout. The text will be Times New Roman font size 10.

2.2 DETAILS OF PAPER LAYOUT

2.2.1 Style of Writing

The language is English and with UK/European spelling. The papers should be written in the third person. Related work conducted elsewhere may be criticised but not the individuals conducting the work. The paper should be comprehensible both to specialists in the appropriate field and to those with a general understanding of the subject.

Company names or advertising, direct or indirect, is not permitted and product names will only be included at the discretion of the editor. Abbreviations should be spelt out in full the first time they appear and their abbreviated form included in brackets immediately after. Words used in a special context should appear in inverted single quotation mark the first time they appear. Papers are accepted also on the basis that they may be edited for style and language.

2.2.2 Paper length

Paper length is free, but should normally not exceed 10000 words and twenty illustrations.

2.2.3 Diagrams and figures

Figures and Tables will either be entered in one column or two columns and should be 80 mm or 160 mm wide respectively. A minimum line width of 1 point is required at actual size. Captions and annotations should be in 10 point with the first letter only capitalised *at actual size* (see Figure 1 and Table VII).

Contact author: author1¹, author2²

¹Address of author1.

²Address of author2 if different from author1's address.

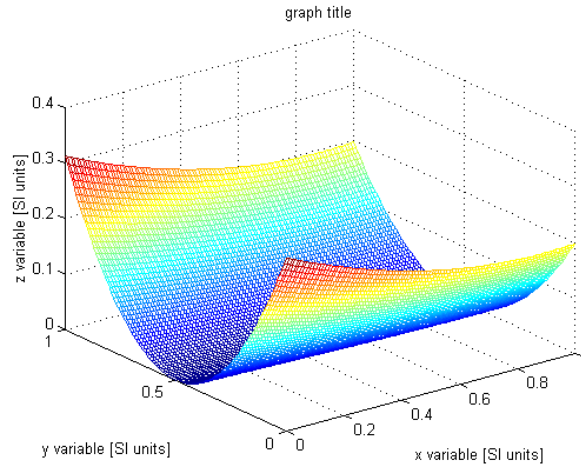


Figure 1 Simple chart.

Table VII - Experimental values

Robot Arm Velocity (rad/s)	Motor Torque (Nm)
0.123	10.123
1.456	20.234
2.789	30.345
3.012	40.456

2.2.4 Photographs and illustrations

Authors could wish to publish in full colour photographs and illustrations. Photographs and illustrations should be included in the electronic document and a copy of their original sent. Illustrations in full colour ...

2.2.5 Equations

Each equation should occur on a new line with uniform spacing from adjacent text as indicated in this template. The equations, where they are referred to in the text, should be numbered sequentially and their identifier enclosed in parenthesis, right justified. The symbols, where referred to in the text, should be italicised.

- point 1
 - point 2
 - point 3
- 1. numbered point 1
- 2. numbered point 2
- 3. numbered point 3

$$W(d) = G(A_0, \sigma, d) = \frac{1}{T} \int_0^{+\infty} A_0 \cdot e^{-\frac{d^2}{2\sigma^2}} dt \quad (1)$$

3 COPYRIGHT

Authors will be asked to sign a copyright transfer form prior to JoMaC publishing of their paper. Reproduction of any part of the publication is not allowed elsewhere without permission from JoMaC whose prior publication must be cited. The understanding is that they have been neither previously published nor submitted concurrently to any other publisher.

4 PEER REVIEW

Papers for publication in JoMaC will first undergo review by anonymous, impartial specialists in the appropriate field. Based on the comments of the referees the Editor will decide on acceptance, revision or rejection. The authors will be provided with copies of the reviewers' remarks to aid in revision and improvement where appropriate.

5 REFERENCES (DESCRIPTION)

The papers in the reference list must be cited in the text. In the text the citation should appear in square brackets [], as in, for example, "the red fox has been shown to jump the black cat [3] but not when...". In the Reference list the font should be Times New Roman with 10 point size. Author's first names should be terminated by a 'full stop'. The reference number should be enclosed in brackets.

The book titles should be in *italics*, followed by a 'full stop'. Proceedings or journal titles should be in *italics*. For instance:

REFERENCES (EXAMPLE)

- [1] Smith J., Jones A.B. and Brown J., *The title of the book*. 1st edition, Publisher, 2001.
- [2] Smith J., Jones A.B. and Brown J., The title of the paper. *Proc. of Conference Name*, where it took place, Vol. 1, paper number, pp. 1-11, 2001.
- [3] Smith J., Jones A.B. and Brown J., The title of the paper. *Journal Name*, Vol. 1, No. 1, pp. 1-11, 2001.
- [4] Smith J., Jones A.B. and Brown J., *Patent title*, U.S. Patent number, 2001.

International Journal of Mechanics and Control – JoMaC
Published by Levrotto&Bella
TRANSFER OF COPYRIGHT AGREEMENT

<p>NOTE: Authors/copyright holders are asked to complete this form signing section A, B or C and mail it to the editor office with the manuscript or as soon afterwards as possible.</p>	<p><i>Editor's office address:</i> Andrea Manuello Bertetto Elvio Bonisoli <i>Dept. of Mechanics</i> <i>Technical University – Politecnico di Torino</i> <i>C.so Duca degli Abruzzi, 24 – 10129 Torino – Italy</i> <i>e_mail: jomac@polito.it</i> <i>fax n.: +39.011.564.6999</i></p>
--	---

The article title:

By: _____

To be Published in *International Journal of Mechanics and Control JoMaC*
Official legal Turin court registration Number 5320 (5 May 2000) - reg. Tribunale di Torino N. 5390 del 5 maggio 2000

- A Copyright to the above article is hereby transferred to the JoMaC, effective upon acceptance for publication. However the following rights are reserved by the author(s)/copyright holder(s):
1. All proprietary rights other than copyright, such as patent rights;
 2. The right to use, free or charge, all or part of this article in future works of their own, such as books and lectures;
 3. The right to reproduce the article for their own purposes provided the copies are not offered for sale.
- To be signed below by all authors or, if signed by only one author on behalf of all co-authors, the statement A2 below must be signed.*

A1. All authors:

SIGNATURE _____ DATE _____ SIGNATURE _____ DATE _____

PRINTED NAME _____ PRINTED NAME _____

SIGNATURE _____ DATE _____ SIGNATURE _____ DATE _____

PRINTED NAME _____ PRINTED NAME _____

A2. One author on behalf of all co-authors:

"I represent and warrant that I am authorised to execute this transfer of copyright on behalf of all the authors of the article referred to above"

PRINTED NAME _____

SIGNATURE _____ TITLE _____ DATE _____

B. The above article was written as part of duties as an employee or otherwise as a work made for hire. As an authorised representative of the employer or other proprietor. I hereby transfer copyright to the above article to *International Journal of Mechanics and Control* effective upon publication. However, the following rights are reserved:

1. All proprietary rights other than copyright, such as patent rights;
2. The right to use, free or charge, all or part of this article in future works of their own, such as books and lectures;
3. The right to reproduce the article for their own purposes provided the copies are not offered for sale.

PRINTED NAME _____

SIGNATURE _____ TITLE _____ DATE _____

C. I certify that the above article has been written in the course of employment by the United States Government so that no copyright exists, or by the United Kingdom Government (Crown Copyright), thus there is no transfer of copyright.

PRINTED NAME _____

SIGNATURE _____ TITLE _____ DATE _____

CONTENTS

3 Motion Principles and Control of a Human Riding Type Robotic Unicycle (Part 1)

H. Suzuki, S. Moromugi and K. Yamafuji

13 Motion Principles and Control of a Human Riding Type Robotic Unicycle (Part 2)

H. Suzuki, S. Moromugi and K. Yamafuji

21 3D Models for Langhe Hazelnuts

S. Tornincasa, E. Bonisoli and M. Brino

29 An Experimental Characterization of a Rickshaw Prototype

T. Li and M. Ceccarelli

**39 A Control System for Robot Trajectory Planning:
Algorithm and First Experimental Results**

C. Rossi and S. Savino

next number scheduled titles:

Epi.q-1.2, A Hybrid Mobile Mini Robot with a Reconfigurable Three Wheeled Locomotion Unit
G. Quaglia, W. Franco, D. Maffiodo, S. Appendino and R. Oderio

Modelling and Temperature Control of Shape Memory Alloys with Fast Electrical Heating
R. Velázquez and E.E. Pissaloux

Vehicles Headlamps Glare Effect Removal
G. Ligios and A. Manuello Bertetto

Nonlinear Elastic Characteristic of Magnetic Suspensions through Hilbert Transform
E. Bonisoli

The Mechanism of Crank Initiation and Propagation in Metallic Engineering Materials
V.T. Hoang